

Université du Québec
Institut National de la Recherche Scientifique
Centre Énergie, Matériaux et Télécommunications

ELECTRON MICROSCOPY TECHNIQUES FOR THE CHARACTERIZATION OF SUB-PARTICLE MORPHOLOGIES OF HOLLOW METALLIC NANOPARTICLES AND THEIR EFFECT ON CARGO RELEASE APPLICATIONS

Par

Jesus Angel Valdez Aguilar

Thèse présenté(e) pour l'obtention
du grade de Philosophiae Doctor (Ph.D.)
en sciences de l'énergie et des matériaux

Jury d'évaluation

Président du jury et
examineur interne

Professeur Kenneth Beyerlein
Institut National de la Recherche
Scientifique

Examineur externe

Professeur Ashok Kakkar
McGill University

Examineur externe

Professeure Anna Ritcey
Université Laval

Directrice de recherche

Professeure Dongling Ma
Institut National de la Recherche
Scientifique

ACKNOWLEDGEMENTS

I would like to express my gratitude to the INRS for their administrative, academic, and financial support in all these years of my studies. To the Mexican Council for Science and Technology-Secretariat of Energy (CONACYT-SENER), Government of Nuevo Leon, Prof. Idalia Gomez, and the University of Nuevo Leon for sponsor and tutor me with the scholarship for my Ph.D. studies. I thank the Natural Sciences and Engineering Research Council of Canada (NSERC), Fonds de recherche du Québec – Nature et technologies (FRQNT) for their financial contribution to the research.

I thank the research group members Rasool, Wanting, Rezvan, and Omar for sharing the time, knowledge, and jokes during these years. I am grateful for the experience of Zakaria Mahfoud, Tugrul Guner, and Lucas Vazquez for helping me to understand and trying to like (a bit) the computational simulations and data analysis with software. I still like more to be in a laboratory.

I also thank Prof. Ma, Prof. Marc, Prof. Kenneth, and Prof. Tavares, and the people working in their laboratories to help me use the instruments and the space provided to perform my experiments.

I thank my friends who always were there to chat, hang out, and the "occasionally?" pre-COVID Saturday nights with the amazing cochinita pibil tacos, hot sauce, and some Quebec tasty cider in La Fontaine Park. God, how much I miss that.

For their long calls and support, I thank my parents and family that helped me during difficult times in my studies, specifically with my mother's good Mexican recipes for improving my cooking.

I also thank the jury members, Prof. Kenneth, Prof. Kakkar, Prof. Marc, and Prof. Ritcey, for taking the time to evaluate and comment on my thesis.

Finally, I would like to thank Prof. Yurtsever for the experience that I got from him with physics and microscopy. I also thank Prof. Ma that I could not finish this work without her help, time, and patience during the last year. It was a pleasure to work with two great supervisors. I learned a lot from you.

RÉSUMÉ

Les détails structurels des nanoparticules au niveau des sous-particules sont essentiels pour comprendre leurs fonctionnalités et les mécanismes impliqués dans leur formation. En particulier, les géométries de ces caractéristiques déterminent la réponse optique globale de la particule. Les nanoparticules métalliques creuses de géométries cubiques, avec des morphologies variables sur leurs parois et leurs vides, offrent une plate-forme pour étudier les effets de ces caractéristiques structurelles sur les propriétés de nanoparticules uniques et de leur ensemble. Dans cette thèse, je rapporte le contrôle des trous et des vides des sous-particules en modifiant la dynamique de la réaction de remplacement galvanique (GRR). Avec l'usage de la microscopie électronique à balayage et à transmission (MEB et MET), des analyses statistiques et des simulations électromagnétiques, j'ai observé que la rupture de symétrie dans les particules individuelles, causée par les morphologies des sous-particules telles que les trous, les vides, les coins ouverts et les pores ont un effet drastique sur les positions des pics de résonance plasmonique dans leurs spectres ultraviolets-visible-proche infrarouge (UV-Vis-NIR). Ces observations sont essentielles pour comprendre la formation des structures pendant le GRR, utilisées pour concevoir les nanoparticules creuses pour diverses applications. Dans mon travail de thèse, j'emploie les MNP creux comme agents de livraison. J'ai abordé l'effet des morphologies de sous-particules sur la livraison du cargo. Par imagerie en champ clair par MET, j'ai calculé la proportion de livraison du cargo sous la surface (ARR) des nanoparticules creuses. J'ai observé que l'incrémentatation des coins ouverts augmente l'ARR dans les petits et grands modèles. J'ai également observé que l'accumulation de polyvinylpyrrolidone (PVP) au-dessus des régions de sous-particules altère la livraison du cargo. Dans les analyses MET, pour les petites morphologies représentées par des pores, ce phénomène provoque un blocage de la morphologie des sous-particules en raison du comportement PVP dans les expériences en phase solide. Cependant, lorsque des particules avec de petites morphologies de sous-particules sont stimulées thermiquement dans la phase liquide, la livraison du cargo est obtenue. De plus, lorsque la taille des morphologies de sous-particules augmente dans les expériences en phase solide, comme les trous et les coins ouverts, l'effet de blocage PVP

est minimisé, augmentant la livraison du cargo. En outre, j'ai observé que l'utilisation de différents substrats altère la livraison du cargo des nanoparticules creuses. Alors qu'un substrat isolant améliore la livraison du cargo, un excellent matériau thermiquement conducteur le diminue. Cet effet est dû au fait que le substrat isolant augmente excessivement la température locale autour des nanoparticules creuses et du substrat de support adjacent en comparaison au reste des régions.

Nos résultats décrivent la conception de nanoparticules via des morphologies de sous-particules pour plusieurs applications. Par ailleurs, notre méthodologie propose une nouvelle méthode de caractérisation par microscopie électronique pour étudier *in-situ* les mécanismes de livraison du cargo des nanostructures. À ma connaissance, la caractérisation *in-situ* de nanoparticules uniques pour les études structurales, optiques et de livraison du cargo n'a pas été abordée auparavant.

Mots clés: nanoparticules, cargo, *in-situ*, creux, MET, sous-particule, livraison, température

ABSTRACT

The structural details of nanoparticles at the sub-particle level are critical for understanding their functionalities and the basic mechanisms involved in their formation. In particular, the geometries of such features determine the particle's overall optical response. Hollow metallic nanoparticles (hollow-MNPs) with cubic geometries, and varying morphologies on their walls and voids, offer a platform to study the effects of such structural features on the properties of single nanoparticles and their ensemble. In this thesis, I report the control over sub-particle pinholes and voids by modifying the galvanic replacement reaction (GRR) dynamics. Using scanning and transmission electron microscopy (SEM and TEM), statistical analyses, and electromagnetic simulations, I observe that symmetry breakage in individual particles, caused by the sub-particle morphologies such as pinholes, voids, open corners, and pores, has a drastic effect on the plasmon-resonance peak positions in their ultraviolet-visible-near infrared (UV-Vis-NIR) spectra. These observations are essential to understand the formation of the step-like structures during the GRR, used to engineer the hollow-MNPs for diverse applications. In my thesis work, I employ hollow-MNPs as cargo release agents. I address the effect of sub-particle morphologies on the cargo release. From bright-field images, I calculate the area release ratio (ARR) of the hollow-MNPs. I observe that the increment of open corners increases the ARR in both small and large templates. I also observe that the accumulation of polyvinylpyrrolidone (PVP) over the sub-particle regions alters the release of the cargo. In TEM analysis of small pores, this phenomenon blocks the pore in the solid phase experiments. However, when particles with small sub-particle morphologies are thermally stimulated in the liquid phase, the cargo release is achieved. In addition, when the sub-particle morphologies' sizes increase in the solid phase experiments, like pinholes and open corners, the PVP blocking effect is minimized, increasing the cargo release. Also, I observe that the use of different substrates alters the cargo release of hollow-MNPs. An insulator substrate enhances the cargo release, while an excellent thermally conductive material decreases it. This effect is because the insulator substrate excessively increases the local temperature around the hollow-MNPs and the adjacent-supporting substrate compared to the rest of the regions.

Our results outline nanoparticle design *via* sub-particle morphologies for several applications. Besides, our methodology proposes a new characterization method *via* electron microscopy for studying *in-situ* the cargo release mechanisms of nanostructures. To the extent of my knowledge, single nanoparticles' *in-situ* characterization for structural, optical, and cargo delivery studies has not been addressed before.

Keywords: nanoparticles, cargo, *in-situ*, hollow, TEM, sub-particle, delivery, temperature

SOMMAIRE RÉCAPITULATIF

Techniques de microscopie électronique pour la caractérisation des morphologies de sous-particules de nanoparticules métalliques creuses et leur effet sur les applications de livraison du cargo

INTRODUCTION

Au cours des dernières décennies, émergentes maladies infectieuses et chroniques sont apparues au sein de la population. Ceux qui ont une incidence génétique ou un désavantage géographique augmentent rapidement ou menacent d'augmenter prochainement. Le concept de trouver des nouvelles voies de traitement pour ces maladies a été proposé récemment. La nano-médecine a été proposée comme nouvelle voie de traitement des maladies. Cette science est basée sur l'application de la nanotechnologie pour guérir la menace médicale d'une population en utilisant des matériaux à l'échelle nanométrique. Elle combine la physique, la chimie et la biologie pour résoudre un défi que les méthodes cliniques conventionnelles ne peuvent pas relever. Avec la progression de cette science et l'avancement de la recherche des nouveaux médicaments et systèmes d'administration, des nombreuses procédures thérapeutiques basés sur la nanotechnologie ont été proposées, offrant un nouvel avantage aux méthodes cliniques traditionnelles.

Plusieurs des études ont montré l'importance d'étudier différents mécanismes de livraison des médicaments pour adapter ces résultats à traitements nouveaux et efficaces dans l'organisme. Chaque voie d'administration a des facteurs qui peuvent affecter la biodisponibilité des médicaments et elles possèdent des avantages et des inconvénients. Le perfectionnement des méthodes d'administration ou la conception de nouvelles méthodes peuvent améliorer l'administration de chaque médicament. Les véhicules de livraison (VLs) peuvent être associés à des stratégies de cargo des médicaments et de ciblage pour améliorer l'efficacité du médicament. Les VLs permet aux scientifiques de trouver différentes façons de traiter la maladie dans l'organisme sans changer le médicament ni l'améliorer.

La recherche sur les nanoparticules métalliques (MNPs) a connu un essor au cours des dernières décennies. En particulier, les nanoparticules creuses ont été utilisées avec succès en nano-médecine en raison de leur avantage à régler leurs résonances plasmoniques jusqu'à la gamme spectrale proche infrarouge sans augmenter leur taille totale, et elles peuvent être nano-conçues pour absorber la lumière dans le range biologique permis. Cet avantage permet aux nanoparticules creuses d'avoir une résonance plasmonique et de conserver de petites tailles qui facilitent l'absorption cellulaire, une propriété que les nanoparticules conventionnelles ne possèdent pas.

Les caractéristiques fonctionnelles des nanoparticules creuses sont en fonction des morphologies structurales des sous-particules qui se développent au cours du processus de creusage. Par conséquent, notre capacité à utiliser efficacement ces particules dans différentes applications est fondamentalement liée à notre compréhension de leurs détails structurels et de la manière dont elles se forment à travers l'évolution des processus chimiques pertinents.

Les nanoparticules creuses sont synthétisées en utilisant des nano-cubes de Ag comme modèles. Ce processus de synthèse utilise la réaction de remplacement galvanique. Les changements structurels se produisent par la réaction galvanique entre les espèces Ag et HAuCl_4 , en remplaçant de le Ag atomique par de le Au *via* la réduction spontanée de Au^{3+} par Ag^0 .

En l'échelle nanométrique, la réaction commence lorsqu'une nanoparticule d'Ag entre en contact avec des ions AuCl_4^- . Ensuite, les atomes Ag sont oxydés spontanément et dissous par les ions AuCl_4^- , donnant des ions Ag^+ dans la solution de la réaction. Simultanément, les atomes Au se déposent à la surface de la nanoparticule en raison de la réduction de l'ion Au^{3+} (situé dans les ions AuCl_4^-). Comme l'Ag et l'Au sont miscibles à l'échelle nanométrique, tout deux avoires la même structure cristalline cubique à faces centrées (FCC) et des constantes de paramètre cristallin similaires, la formation d'un alliage AgAu est attendue avec une composition variable en fonction de la concentration d' AuCl_4^- dans la solution. Cette miscibilité implique une diffusion des atomes métalliques. Elle est régie par de nombreux facteurs, tels que les espèces chimiques impliquées, les conditions de réaction (par exemple, la température) et les propriétés physiques, telles que la taille et la forme des nanoparticules. Les transformations chimiques et structurelles

dans les nanoparticules creuses, se produisant par réaction de remplacement galvanique ont des effets drastiques sur le spectre optique (absorbance), avec une caractéristique préminente étant le déplacement de la longueur d'onde de leurs modes plasmoniques résonants.

La formation de structures creuses permet la possibilité d'insérer des matériaux à l'intérieur de la structure. Ce cargo peut être livré par différents mécanismes. Cependant, des mécanismes de stimulus thermiques sont souvent utilisés pour effectuer le processus de livraison. La génération de chaleur dans les nanoparticules métalliques (comme les nanoparticules creuses) efficace dans la gamme de la résonance plasmonique, qui est un mouvement collectif d'électrons, et elle est provoquée lorsque la nanoparticule métallique est exposée à une excitation optique (par exemple, laser).

Une fois l'énergie est absorbée, il pourrait y avoir une excitation et une relaxation à travers des différents types de mécanismes, et compris les phénomènes électron-électron (e-e) et électron-phonon (e-ph), en fonction de l'irradiation de la source. L'interaction électron-électron commence lorsque les électrons libres (dans la nanoparticule métallique) absorbent l'énergie. Ce processus d'interaction obtient une partie de leur énergie totale. En outre, l'interaction e-ph au sein d'un réseau cristallin de la nanoparticule métallique est contribué. La chaleur est dissipée de nanoparticule métallique et augmente la température du milieu environnant.

De même comme l'interaction photon-matière, les électrons peuvent également soutenir une interaction inélastique avec des électrons libres et par des excitations d'électrons collectives dans l'échantillon, comme le plasmon et polaritons. Aussi, qu'ils perdront de l'énergie qui peut être transférée sous la forme de chaleur. Ces mécanismes peuvent être observés et mesurés dans une microscopie électronique à transmission (MET) où différentes techniques de caractérisation telles que la spectroscopie de perte d'énergie électronique (EELS) que sont basées sur le principe d'électron-matière. L'utilisation de la microscopie électronique à transmission (MET) pour étudier et caractériser les propriétés physico-chimiques des nanomatériaux à l'échelle nanométrique a été cruciale pour

comprendre et corrélés les processus qui expliquent le comportement des nanostructures.

L'interaction entre les énergies élevées du faisceau électronique et l'échantillon produit une gamme de signaux qui fournissent diverses informations en microscopie électronique. Les informations que nous pouvons obtenir à partir de ces interactions sont la composition chimique, la morphologie de l'imagerie et l'étude des structures cristallines de l'échantillon. Au cours de l'interaction électron-matière, la chaleur est également générée, ce qui rend possible l'utilisation du faisceau électronique comme source de chauffage contrôlable pour la génération de processus thermiques à l'échelle nanométrique et des études thermiques en microscopie électronique.

La chaleur générée pour le faisceau électronique en microscopie électronique a été utilisée pour des mesures thermiques dans un nouveau dispositif à base de dioxyde de vanadium, des conductances thermiques des nanoparticules et des matériaux 2D et pour l'effet Debye-Waller pour les mesures thermiques.

Par conséquent, l'importance du faisceau électronique dans les études de microscopie électronique est déterminante non seulement pour les études thermiques, mais aussi pour les changements structurels, les compositions chimiques ou les mesures où la chaleur peut avoir un effet dans l'échantillon.

Dans ce travail, nous utiliserons la chaleur générée par le faisceau électronique dans les expériences de la MET pour activer la livraison du cargo dans les nanoparticules creuses. Ce travail étudiera l'effet des caractéristiques des sous-particules et l'effet du substrat sur la vitesse et la quantité de livraison du cargo. Ces expériences aideront également à élucider la distribution physique de la chaleur lors de la livraison d'un cargo.

Champ d'étude

Dans cette thèse, nous allons synthétiser deux types différents des nanoparticules creuses. Nous étudierons et comparerons les morphologies des sous-particules à l'aide de deux modèles Ag cube différents (appelés petits et grands modèles). Par la réaction de remplacement galvanique, nous observerons les changements structurels dans les nanoparticules creuses. Nous établirons une corrélation de ces caractéristiques des

sous-particules (trous et vides) avec les spectres d'absorption optique. Nous présenterons les résultats de la microscopie électronique à balayage (MEB), de la spectroscopie UV-vis-IR, des outils logiciels analytiques et des simulations électrodynamiques pour discuter de la relation entre la structure et les propriétés optiques des nanoparticules creuses. Cette recherche nous aidera à concevoir le type de caractéristique des sous-particules que nous voulons utiliser pour de futures applications. Nous étudierons la livraison d'un cargo dans les nanoparticules creuses en chauffant indirectement la nanoparticule avec un faisceau électronique dans le MET. Cette technique de caractérisation nous permettra d'analyser les particules individuelles au même qu'elles sont irradiées. À travers de l'imagerie par MET, et la spectroscopie de perte d'énergie des électrons (EELS), nous éluciderons l'effet des morphologies des sous-particules sur les mécanismes de livraison. À notre connaissance, ces études n'ont jamais été réalisées pour des nanoparticules isolées.

REVUE DE LA LITTÉRATURE

Les nanoparticules creuses ont été largement étudiées en vue d'applications dans différents domaines tels que la catalyse, la plasmonique et la nanomédecine. Leur avantage est qu'elles présentent des propriétés dépendantes de la taille, de la forme, de la morphologie et de la composition. À travers à la synthèse contrôlée, il est possible de contrôler les propriétés physiques et chimiques des nanoparticules creuses et de concevoir la nanoparticule spécifique qui peut être utile en fonction de l'application. Cependant, le contrôle de leurs caractéristiques structurales (par exemple, la taille, les vides ou les trous) est un défi.

Synthèse et les études structurales des nanoparticules creuses

L'exigence en matière de chimie utilisant la réaction de remplacement galvanique est basée sur des réactifs qui possèdent un potentiel d'oxydation et de réduction plus élevée. Le réactif possédant d'un potentiel de réduction plus élevé s'appeler "modèle sacrificielle"; en général, ces modèles sont des nanoparticules métalliques solides. L'analyte, qui a un potentiel d'oxydation plus élevé, est une solution anionique métal-halogénée à base de métaux ioniques tels qu'Au, Pd ou Pt.

La réaction de remplacement galvanique se développe en cinq étapes générales :

- i) Initiation de la dissolution de l'Ag pendant le dépôt d'Au³⁺.
- ii) Formation d'un trou et de parois uniformes en alliage d'Au-Ag
- iii) Suppression des coins
- iv) Génération de pores dans le mur par un processus de désengagement
- v) Génération de pores dans les coins

En général, les structures creuses peuvent exister dans différentes morphologies fabriquées par réaction de remplacement galvanique. Les nanoparticules d'argent ont été choisies comme modèle pour un modèle sacrificiel pour la synthèse des nanoparticules creuses. Elles peuvent être produites sous forme de sphères, de plaques et de cubes. Cependant, les nanostructures de sphères, de plaques et de cubes sont les plus utilisées dans les réactions de remplacement galvanique.

Dans les applications d'administration de médicaments, la propriété optique n'est pas le paramètre essentiel à prendre en compte ; la biocompatibilité, la stabilité et la quantité du cargo chargée sont les principaux paramètres que les nanoparticules creuses doivent respecter pour être utilisés dans l'administration de médicaments.

Les nanoparticules creuses cubiques sont des structures poreuses de taille compacte et peuvent être synthétisées avec précision en contrôlant leurs propriétés plasmoniques et la chimie de surface. Les propriétés à l'état solide de ces nanostructures représentent un avantage en comparaison au reste des structures creuses. Par exemple, les modèles des nanocubes d'Ag possèdent des sites actifs spécifiques. Ces sites entraînent des changements structurels au cours de la réaction de remplacement galvanique, que les nanosphères d'Ag ne possèdent pas. Cet avantage des nanocubes d'Ag est crucial parce qu'il permet aux chercheurs de concevoir la nanoparticule en fonction de la propriété optique, de la taille et de la morphologie des sous-particules.

Les nanoparticules creuses en morphologie cubique sont les structures les plus appropriées pour les applications d'administration de médicaments en raison de leurs avantages en matière de morphologie et de formation de structures. Cependant, les détails structurels de ces nanostructures doivent être étudiés pour maximiser le succès des applications biomédicales.

Études structurelles des nanoparticules cubiques creuses

Le contrôle nul des caractéristiques des sous-particules représente un défi si ces nanostructures sont utilisées dans l'administration de médicaments, car les possibilités de modifier leurs structures sont limitées, ce qui peut interdire l'absorption ou l'administration du médicament. Cependant, Skrabalak *et al.* ont étudié les mécanismes impliqués dans la production de nanoparticules cubiques creuses. Des analyses au MEB et MET ont montré que la morphologie initiale des nanocubes d'Ag conduit à différents mécanismes de modification structurelle pour produire des nanoparticules creuses.

En 2016, Genç *et al.* ont rapporté dans la littérature le réglage optique du LSPR de l'ultraviolet à l'infrarouge proche en utilisant la réaction de remplacement galvanique en utilisant des nanocubes d'Ag solides comme modèle sacrificiel et en les transformant en nanoparticules creuses. Pour ce faire, ils ont utilisé une méthode de synthèse modifiée en utilisant du bromure de cetyltriméthylammonium (CTAB) et de l'acide ascorbique dans la réaction de remplacement galvanique. À travers de ce changement, différentes structures d'étapes ont été obtenues.

Les changements structurels tels que dans la nanoparticule entière, comme dans les morphologies des sous-particules, ont pu être obtenus en modifiant les paramètres de la réaction galvanique ou la morphologie des modèles d'argent. Cependant, pour avoir une comparaison directe et la possibilité de surveiller la réaction pour contrôler ces étapes, la réaction galvanique doit être suivie sans modifications. L'effet de la taille du gabarit sur les morphologies des sous-particules n'a pas été étudié. Il est donc essentiel de développer une méthode pour étudier et expliquer les mécanismes impliqués par ce changement.

Nanoparticules creuses comme véhicules de livraison du cargo

En raison de leur stabilité et de leur biocompatibilité, ainsi que de leur manipulation sûre, les matériaux de change de phase (PCMs) ont été utilisés au cours de la dernière décennie pour l'administration de médicaments à l'aide de nanoparticules creuses. Les PCMs changent leurs caractéristiques physiques lorsqu'ils absorbent de la chaleur. La phase du matériau varie en fonction de la température et, selon le rang de température, ces matériaux peuvent fondre ou se solidifier. Selon l'application, les PCMs peuvent être choisis en fonction de leur température de fusion. Dans l'administration de médicaments, cette température doit être proche de la température moyenne du corps afin d'éviter les dommages causés par la chaleur pour libérer le médicament.

En 2011, Moon *et al.* ont présenté un nouveau système d'imagerie diagnostique par contraste pour l'administration contrôlée de médicaments à l'aide d'un PCM. Ils ont rempli le vide des nanoparticules creuses avec du 1-tétradécanol (le PCM) combiné à un colorant pour effectuer ce travail. Le colorant simule la présence d'un médicament. L'objectif du colorant est de détecter l'effet de sa présence dans le système, par exemple, si la charge à l'intérieur d'une nanoparticule creuse a réussi en observant l'absorption optique du colorant après la procédure de chargement.

De même, Tian *et al.* ont rapporté l'effet de la température et de l'irradiation laser sur la livraison du médicament ou du colorant. L'effet de la température est basé sur la livraison maximale par rapport à la température ambiante ; Tian *et al.* ont trouvé une température maximale de 42 °C et Moon *et al.* à 40 °C. Tout d'abord, aucun d'entre eux n'a indiqué pas la méthode à suivre pour trouver la température maximale de livraison et elle est basée sur l'hypothèse que le PCM aura un changement de phase à ~39 °C. Cependant, les caractéristiques structurelles de la particule peuvent affecter la livraison du cargo, indépendamment de la température de changement de phase. Nous pouvons conclure ici qu'une étude de cet effet fait défaut.

Techniques d'imagerie pour les applications de livraison du cargo

Les techniques d'imagerie qui permette d'évaluer l'administration de médicaments à base de nanoparticules sont d'une grande importance. Plusieurs de ces techniques jouent un rôle important dans l'évaluation préclinique des nanosystèmes d'administration de médicaments, permettant d'élucider leur mécanisme d'action et leur effet thérapeutique.

Microscopie à force atomique (AFM)

L'AFM a été utilisée pour étudier les interactions entre médicaments et de la cellule et de la molécule d'une manière singulière, ce qui permet de visualiser les effets des médicaments à l'échelle des cellules vivantes, inaccessibles par les techniques traditionnelles de caractérisation. Cette technique permet également de mesurer la taille et de nombreux autres paramètres physiques des médicaments en une seule analyse. Cependant, cette technique a été utilisée pour obtenir uniquement des informations physiques sur les nanoparticules et elle pose un problème commun pour la caractérisation de l'administration de médicament. Le temps de balayage est crucial pour analyser l'administration *in-situ* ou *in-vivo*, connaissant que l'administration initiale est rapide. Cette technique n'est pas adaptée à la caractérisation des mécanismes de livraison à l'échelle nanométrique pour tout type des nanosystèmes d'administration de médicament.

Microscopie électronique

De nombreux des véhicules inorganiques telles que les nanoparticules de silice mésoporeuse, les nanoparticules métallo-organiques et les nanoparticules de carbone ont été analysés au microscope électronique. En raison de ses avantages en comparaison aux techniques conventionnelles et de la possibilité d'analyser les nanosystèmes avec différentes techniques *in-situ* (par exemple, EELS, EDS, etc.), la microscopie électronique a permis d'observer avec succès l'interaction des véhicules inorganiques avec les systèmes vivants.

La microscopie électronique a principalement été utilisée pour déterminer l'interaction cellulaire entre les nanosystèmes et les cellules *in vitro* et elle est limitée à l'évaluation de la distribution des nanoparticules sur les entités biologiques ou seulement pour leurs études morphologiques. Actuellement, il n'existe aucune étude associée à la livraison de médicaments par des véhicules inorganiques. Le système fermé d'analyse en microscopie électronique, où le stimulus peut être difficile à fournir, a été limité à cette technique pour leur utilisation dans les analyses *in-vivo* et *in-vitro*.

MÉTHODOLOGIE

Synthèse des nanoparticules cubiques d'Ag

Dans un récipient en verre (20 mL) chauffé à 150 ° C, 6 mL d'éthylène glycol et 70 µL de Na₂S·9H₂O 3 mM ont été ajoutés et le récipient est laissé pendant 10 min. Ensuite, 1.5 mL de PVP 8 M et 0.5 mL d'Ag⁺ 280 mM ont été ajoutés.

La solution a été centrifugée à 2000 g pendant 30 minutes. Le surnageant a été lavé avec de l'eau distillée pendant 3 fois. Le culot a été remis en suspension avec 1.5 mL d'eau distillée et il est ultrason pendant 1 min ; puis, il a été placé dans un flacon contenant 2.5 mL d'eau distillée. Les volumes ont été modifiés avec 2.9 mL d'éthylène glycol, 225 µL Na₂S·9H₂O, 3.75 ml de PVP et 1.25 ml d'Ag⁺ pour des modèles plus grands de nanocubes d'argent.

Synthèse des nanoparticules creuses

Pour ce processus, 5 mL de PVP 0.001 % et un agitateur magnétique ont été placés dans un récipient à fond rond. Ensuite, 200 µL de AgNC pour le petit modelé et 100 µL pour le grand modelé ont été ajoutés dans le flacon et la solution a été chauffée pendant 10 min. Ensuite, on a ajouté du HAuCl₄ 0.1 mM (à une vitesse de 0.75 mL par minute), et la solution a été chauffée à reflux pendant 10 min. Les volumes de HAuCl₄ étaient de 4.01, 4.75, 5.75, 7.00 et 8.50 mL pour le petit modèle ; et pour le grand modelé étaient de 3.00,

4.00, 5.50, 7.00 et 8.50 mL pour le grand modèle. Ensuite, il a été centrifugé à 2000 g pendant 30 min. Les nanoparticules ont été dispersées dans 4 mL d'eau distillée.

Caractérisation des nanoparticules creuses

Tous les échantillons des nanoparticules cubiques d'Ag et des nanoparticules creuses ont été caractérisés en utilisant un UV-Vis-NIR avec une longueur d'onde de balayage de 300 à 1100 nm.

Les analyses structurales et statistiques des nanoparticules creuses petits et grands ont été effectuées à l'aide d'un microscope électronique à balayage et les images sont analysées à l'aide d'un code Matlab.

Simulation électrodynamique

Les simulations informatiques ont été réalisées dans une simulation électrodynamique classique, en résolvant les équations de Maxwell dans un formalisme de méthode des éléments finis (FEM) dans le logiciel commercial COMSOL.

Synthèse des nanoparticules creuses modifiées

Une nouvelle méthode de synthèse a été mise pour obtenir des sous-particules de caractéristiques similaires aux petites nanoparticules creuses. Une version modifiée de la méthode a été réalisée en utilisant un grand modèle de nanoparticules cubiques d'Ag. Pour faire ça, 5 mL de PVP 0,1 % et 2 mL des nanoparticules cubiques grands d'Ag ont été ajoutés dans le flacon. Ensuite, du HAuCl_4 10 mM a été ajouté et la solution a été refluxée pendant 10 min. Les volumes de HAuCl_4 étaient de 8.5, 15 et 22 mL. La solution a été centrifugée et lavée. Le culot a été dispersé dans 4 mL d'eau distillée et gardée dans un flacon de verre à 4 °C.

Chargement du cargo dans les nanoparticules creuses

Dans un flacon de verre, 4 mL des nanoparticules creuses préalablement synthétisés ont été centrifugées et dispersées dans 4 mL d'alcool isopropylique. À partir de cette solution, 3 mL des nanoparticules creuses ont été mélangées à 5 mL de 1-tétradécanol à 70 °C. Après l'évaporation de l'isopropanol, le flacon a été placé dans un bain de sable pendant 8 heures.

Après le chargement du cargo, l'échantillon a été transféré dans un récipient préalablement chauffé (90 °C) et elle est centrifugée à 4600 g pendant 5 min. Ce processus a été répété jusqu'à ce que la majeure partie du 1-tétradécanol soit éliminée. Après la centrifugation, les nanoparticules ont été dispersées dans 1 mL d'eau distillée et gardées à 4 °C.

***In-situ* livraison du cargo des nanoparticules creuses**

La solution de nanoparticules a été diluée 1:1 avec de l'eau distillée, puis 20 µL de cette solution ont été placés dans une grille de TEM avec un substrat de monoxyde de silicium d'une épaisseur de 15 à 30 nm. La solution dans la grille s'évapore à température ambiante.

Des images en champ clair des échantillons ont été recueillies pour analyser la livraison du dans les nanoparticules creuses. La livraison a été capturée dans un processus image par image pendant 30 min.

Les nanoparticules creuses pour les petits et grands (modifiés) modelés ont été classées en fonction de leur nombre de coins ouverts. Toutes les images ont été traitées à l'aide d'un code du logiciel MATLAB.

Comparaison du substrat sur la livraison du cargo

Le grand modelé des nanoparticules creuses a été utilisé pour comparer l'effet de deux substrats sur la livraison du cargo. Les particules ont été analysées par imagerie en champ clair pendant 30 minutes et analysées avec le code MATLAB.

Analyses des MET images en champ clair

L'analyse de chaque pile d'image a été effectuée à l'aide du code de Matlab, générant des informations sur la zone de livraison. Les zones ont été tracées en fonction de leur caractéristique de sous-particule depuis la livraison initiale jusqu'à 30 min.

Détection de PVP sur la surface des nanoparticules creuses

En utilisant la microscopie électronique à transmission par balayage (STEM), les nanoparticules creuses ont été analysées pour détecter la présence de PVP. Plus précisément, les nanoparticules ont été imagées et analysées à l'aide du détecteur de champ noir annulaire à angle élevé (HAADF) et de la spectroscopie de perte d'énergie d'électrons (EELS), avec 10 secs de collecte. La collecte des EELS a été effectuée par un balayage linéaire et l'analyse a été effectuée différemment, en fonction des nanoparticules creuses (modelés grands et petits). Pour les petites nanoparticules creuses, le balayage linéaire a été effectué à partir d'un coin, incluaient part de la face, du coin ouvert, du mur et du substrat. Les grandes nanoparticules creuses (non modifiés) ont été analysés sur face et des pores de la structure. Les grandes nanoparticules creuses (modifiés), ont été analysés en considérant le substrat (les deux côtés), la face et les trous sur la structure.

Les analyses pour la caractérisation du STEM-EELS a été effectué avec un code automatisé dans Matlab en utilisant la soustraction du fond avec le modèle d'ajustement de la loi de puissance.

RÉSULTATS ET DISCUSSION

Caractérisation structurelle

Les nanocubes d'Argent ont différents changements de structure au cours de la réaction de remplacement galvanique pour démontrer les effets des changements structurels sur les nanocubes complets ; les nanoparticules creuses ont d'abord été analysées par MEB. L'évolution de leur taille totale et de leurs épaisseurs de paroi en fonction de la concentration en HAuCl_4 est différente pour les deux modèles. Pour le petit modèle, la taille totale des nanoparticules creuses augmente d'environ 7 nm, par rapport à la taille totale du modèle, et elle reste constante avec l'augmentation de la concentration de HAuCl_4 . En revanche, les nanoparticules creuses grosses présentent un phénomène différent. L'incrément de taille des nanoparticules creuses, à partir de la taille du grand modèle, est négligeable pour la plus faible concentration de HAuCl_4 . Cependant, comme la synthèse est effectuée avec plus de HAuCl_4 , la taille totale des cubes creux augmente linéairement. Pour la concentration la plus élevée de HAuCl_4 , les nanoparticules creuses sont en moyenne d'environ 8 nm plus grands que leur modèle. L'épaisseur totale de la paroi des nanoparticules creuses est la même pour chaque modèle (~10 nm) et reste constante avec l'addition de HAuCl_4 .

Pour les deux modèles, lors du processus de remplacement galvanique, les atomes d'Ag sont oxydés pour réduire les ions Au^{3+} (présentés dans AuCl_4^-), déposant des atomes d'Or à la surface de la nanoparticule. Avec plus d'atomes d'Or déposés, la paroi externe augmente son épaisseur tandis que le vide à l'intérieur de la particule se développe simultanément par l'oxydation de l'Ag dans l'intérieur. De plus, l'épaisseur de la paroi interne est réduite par le processus spontané d'inter-diffusion, qui se produit entre les interfaces d'Or (paroi externe) et Ag (paroi interne), ainsi que par l'oxydation continue de l'Ag sous la réaction de remplacement galvanique. Ce processus fixe la limite géométrique à l'expansion du vide tétraédrique à l'intérieur de la nanoparticule.

Les caractéristiques des sous-particules révèlent des différences structurelles entre les modèles petits et grands. Pour le petit modèle, l'augmentation de la concentration de

HAuCl_4 au-delà du point de développement du vide complet produit des trous sur la face du cube. Le diamètre du trou augmente à mesure que la concentration de HAuCl_4 augmente, et les coins du cube se tronquent, ajoutant des trous supplémentaires à la structure. D'autre part, le grand modèle montre un modèle différent après le développement complet du vide intérieur. Dans ce cas, de petits trous apparaissent lors de l'augmentation de la concentration de HAuCl_4 , et au lieu de croître en taille, ils se multiplient.

Ces informations démontrent différentes caractéristiques de surface pour le petit et le grand modèle, ce qui implique différents mécanismes chimiques impliqués dans leur formation. Cette différence peut s'expliquer par la dynamique de diffusion nette des espèces métalliques composant les nanoparticules alliées. D'autre part, cette dynamique de diffusion est régie par l'effet Kirkendall, un phénomène général décrivant la diffusion nette de deux espèces avec des temps de diffusion différents par échange de lacunes et différentes tensions de surface subies par des nanoparticules de différentes tailles.

Pour le grand modèle, le phénomène dominant à l'origine de l'évolution de la morphologie est basé sur l'effet Kirkendall. Le taux de diffusion de l'Ag est supérieur à celui d'Au. Ainsi, l'interface effective entre Ag et Au se déplace vers la surface extérieure lorsqu'un plus grand nombre d'atomes d'Ag migrent vers la paroi extérieure de la nanoparticule vide, formant un alliage. Ce faisant, ces atomes d'Ag proches de la surface externe de la particule peuvent agir comme de petits sites de nucléation. Une fois que la réaction galvanique oxyde l'Ag élémentaire du noyau, les atomes d'Ag diffusés vers la paroi externe s'oxydent. Cette préférence est en corrélation avec la stabilité de l'espèce, où l'Ag élémentaire est moins stable que l'Ag allié. Après l'oxydation de ces atomes alliés d'Ag, il y aura de petites ouvertures de surface que nous appelons pores.

Les nanoparticules creuses pour le petit modèle ont une tension superficielle plus importante, causée par son rapport surface /volume plus élevé, pour modifier la dynamique de diffusion nette de l'alliage. Comme les études de Murch et al. l'ont montré de petites particules d'alliages métalliques présenteront des défauts tels que des dislocations de Shockley partielles, qui peuvent jouer un rôle essentiel dans la

reconstruction de la particule. Surtout, la densité de tels défauts sur la paroi externe augmente avec la réduction de la taille des nanoparticules. Il a été démontré qu'une dislocation partielle de Shockley pouvait transporter du matériel de l'extérieur vers l'intérieur pour de petites nanoshells. Comme la dislocation crée un canal pour la diffusion des atomes, les atomes à la surface externe diffuseront de préférence vers la surface interne en raison de la tendance du système à supprimer la formation de vide. Contrairement à ce qui s'est passé avec les particules plus grandes, l'apparition de défauts cristallins est sensible à la structure géométrique de la nanoparticule. Ils apparaîtront préférentiellement sur certains sites du cube creux au lieu d'être répartis sur sa surface. Ainsi, un plus petit nombre de sites de nucléation pour les trous apparaissent dans les petites nanoparticules, augmentant en diamètre à mesure que le remplacement galvanique progresse.

Caractérisation optique

Les morphologies de sous-particules modifient les propriétés optiques de ces systèmes de nanoparticules. Des analyses UV-Vis-NIR ont été effectuées pour relier les propriétés optiques à la concentration de HAuCl_4 et, par conséquent, à différentes morphologies structurales des particules. Aussi, des simulations électrodynamiques ont été effectuées pour soutenir et comprendre les observations expérimentales.

Dans ce travail, nous pouvons observer un décalage vers le rouge du pic de résonance principale avec une concentration croissante de HAuCl_4 . Aussi, la réponse optique de ces nanocubes partiellement évidés (en raison de faibles concentrations de HAuCl_4) montre un changement clair dans la forme spectrale du pic d'absorption principal, avec l'apparition d'une épaule du côté à haute énergie de la résonance principale.

J'ai également simulé les structures observées expérimentalement avec une épaisseur de paroi correspondant à 50 % de l'épaisseur moyenne de paroi mesurée pour accueillir le couplage de la structure vide. De plus, nous avons inclus l'alliage de la paroi en utilisant les fonctions diélectriques pour plusieurs alliages Au / Ag et les fonctions diélectriques de l'au et de l'Ag pur en tant que deux régions de paroi distinctes. Les changements dans la

composition de l'alliage n'affectent pas de manière significative la position des résonances plasmoniques. La contribution dominante au LSPR provient des caractéristiques géométriques, des vides et des trous.

Livraison du cargo des nanoparticules creuses

Quand une source d'énergie externe interagit avec une particule plasmonique, de forts champs de surface sont induits en raison de l'excitation cohérente des électrons (LSPR). La relaxation rapide de ces électrons excités produit une forte chaleur localisée. Dans notre travail, J'ai utilisé l'interaction d'un faisceau électronique avec des nanoparticules creuses, pour augmenter la chaleur locale, déclenchant une livraison du cargo. Plus précisément, les nanoparticules creuses avec un cargo seront exposées à un faisceau électronique à 200 kV, qui est également utilisé pour la caractérisation par imagerie.

J'ai réalisé une collection d'images MET en champ clair des nanoparticules creuses avec une variation de la taille et les caractéristiques des sous-particules, telles que les coins ouverts, les pores, les trous, et j'ai comparé leur effet sur le taux de livraison du cargo. Toutes les expériences ont été réalisées dans les mêmes conditions sur le même substrat avec la même énergie de faisceau électronique.

L'analyse de la livraison du cargo a été réalisée à l'aide du logiciel Matlab avec un algorithme de traitement d'image personnalisé. Les images ont été analysées en appliquant un seuil pour sélectionner les zones les plus sombres pour la nanoparticule creuse et la livraison relâchée. Ensuite, un masque a été appliqué sur l'image, puis le calcul de la surface a été automatiquement pris à partir de la valeur de dimension en nanomètres. Il est important de mentionner que chaque image a été analysée automatiquement. Chaque pile d'images de MET en champ clair contient environ 800 images. Chaque image est prise à un moment de la livraison initiale jusqu'à 30 min.

L'image originale est transformée en une image en noir et blanc, différenciant le cargo et la nanoparticule du reste de l'image, qui correspond au substrat. Le processus commence par la première image, qui est considérée comme la première valeur initiale. La première image contient une zone « supplémentaire » du cargo en raison de la livraison immédiate.

Je vais discuter les différences de livraison du cargo sur les petites et grandes nanoparticules dans cette thèse. En outre, le calcul de la livraison d'area sera tracé et comparé pour chaque catégorie du nombre de coins ouverts pour différentes tailles. Ces catégories sont quatre, trois et un coin ouvert, représentés désormais respectivement par 4-OpCo, 3-OpCo et 1-OpCo.

Quantification de la livraison du cargo des nanoparticules creuses petits et grands

Livraison du cargo des nanoparticules creuses petits

La morphologie des sous-particules avec quatre coins ouverts offre plus de livraison du cargo que les autres. Le 3-OpCo possède une valeur de livraison (ARR) de 1.2, avec une livraison de fret trois fois plus petite que 4-OpCo. La nanoparticule creuse avec les coins les moins ouverts (1-OpCo) a un ARR moyenne de 1.03, ce qui est relativement plus petit que le reste. Ces expériences montrent comment les caractéristiques des sous-particules affectent les profils de livraison des nanoparticules. Les coins ouverts aident à l'incrémentation de la livraison du cargo qui est chargée dans la nanoparticule creuse. Le plus est chargé, plus la livraison.

J'ai hypothèse que les coins ouverts sont la morphologie des sous-particules qui domine le mécanisme de chargement et de livraison du cargo pour les petites nanoparticules creuses. Comme les coins ouverts ne sont pas directement affectés par le PVP, les coins ouverts influencent le mécanisme de livraison. Si le nombre de coins ouverts augmente, l'ARR sera augmenté.

Livraison du cargo des nanoparticules creuses grands (avec modification)

Les nanoparticules creuses grands présentent un comportement similaire aux nanoparticules petites pour chaque catégorie. Pour toutes les morphologies, il est montré que le largage de la livraison est amélioré en augmentant le temps d'exposition avec le faisceau électronique. Cependant, comme observé pour les nanoparticules creuses petits, les quatre coins ouverts présentent une plus grande quantité de livraison du cargo que les autres. La grande particule avec le plus grand nombre de coins ouverts à un ARR

moyen de 2.0, indiquant que la surface totale (nanoparticule creuse plus le cargo) devient deux fois la surface initiale (nanoparticule creuses comme la surface initiale). Les valeurs de l'ARR décrément considérablement avec un nombre décroissant de coins ouverts. Le comportement de livraison pour les quatre coins ouverts est également différent du reste. La livraison est beaucoup plus rapide dans les 5 premières minutes. Puis entre 5 et 15 min, la livraison est plus lente pour ensuite se stabiliser après ce temps.

La catégorie 3-OpCo a un ARR=1.43 à 30 min, et il est environ la moitié de la version indiquée pour 4-OpCo. Le 1-OpCo atteint un ARR de 1.15, étant beaucoup plus petit que le reste. La saturation commence au début de la livraison initiale pour 1-OpCo. Pour 3-OpCo et 4-OpCo, la saturation prend plus de temps que 1-OpCo.

Effet du substrat dans la livraison du cargo

Dans les expériences MET, non seulement les nanoparticules sont irradiées avec le faisceau électronique, mais le substrat interagit également avec le faisceau et pourrait affecter les propriétés thermiques des nanoparticules. Pour observer l'effet du substrat sur la livraison du cargo, nous avons comparé deux matériaux différents, un isolant, représenté par SiO, et un bon conducteur thermique, le graphène (Gf).

Dans nos expériences, le substrat joue un rôle important dans les mécanismes de livraison du cargo. Sa fonction est d'augmenter la température locale du système (nanoparticules plus le cargo). Une fois que la particule est irradiée avec le faisceau électronique, le substrat provoquera une isolation thermique, produisant une élévation de la température locale dans la nanoparticule, qui est ensuite transférée au cargo et au substrat environnant. Le cargo est ensuite fondu de cette manière ; il peut déplacer dans le substrat en raison de sa température plus élevée (supérieure à 40 ° C). Cependant, si le substrat est un bon conducteur thermique, tel que le graphène, la chaleur sera dissipée plus rapidement. La température locale sera alors confinée dans une zone beaucoup plus petite, empêchant la cargaison de s'écouler à travers le substrat. En comparaison d'un substrat insolent, la chaleur sera plus haute dans le substrat et le cargo peut déplacer en une zone supérieure.

CONCLUSIONS

Analyse structurale des nanoparticules creuses

Cette thèse a porté sur les études structurales des nanoparticules creuses et les effets des caractéristiques des sous-particules sur les propriétés optiques et les études de livraison du cargo. À travers des études expérimentales, nous avons caractérisé les étapes intermédiaires de la réaction de remplacement galvanique qui transforme les nanoparticules cubiques d'Ag en nanoparticules creuses. Nous avons observé que les nanoparticules creuses suivent un développement morphologique différent au cours de la réaction galvanique, déterminé par la taille du modèle initial.

Les modèles petits des nanoparticules cubiques d'Ag commencent par un développement à moitié vide. Au fur et à mesure que la réaction galvanique se poursuit, d'autres morphologies de sous-particules se développent, d'abord le développement complet du vide dans toute la structure, puis l'apparition d'un trou sur la face de la structure et enfin la modification et l'ouverture des coins. De même, les nanoparticules cubiques grandes d'Ag ont montré des structures semblables au vide, mais les dernières morphologies des sous-particules dans la réaction galvanique ont créé de petits pores sur les facettes des cubes creux. Nous attribuons ces différences structurales à des changements dans le mécanisme de diffusion dominant des nanoparticules avec différentes relations surface/volume.

Les morphologies des sous-particules formées pour les différents modèles ont eu un effet majeur sur les résonances plasmoniques et, par conséquent, sur l'absorption optique des nanoparticules. À travers de la caractérisation optique, nous avons pu observer que chaque structure a une absorption dans une longueur d'onde spécifique. Ces absorptions sont les résonances plasmoniques, qui sont caractéristiques de chaque particule en fonction de la morphologie de la sous-particule. Cependant, les structures semblables à des vides présentent des modes différents. Avec à l'analyse de simulation, nous avons pu expliquer que les phénomènes présentés dans les structures vides sont dus à

l'hybridation des modes plasmoniques et à leur interaction avec les surfaces extérieures des nanoparticules creuses.

De plus, l'analyse dans la simulation montre que les absorptions de résonances plasmoniques caractéristiques optiques concordent avec celles obtenues par les résultats des expériences. Cependant, la différence est attribuée à différentes morphologies de sous-particules dans les nanoparticules creuses, ce qui provoque un pic d'absorption avec un demi-maximum de largeur totale (FWHM) spécifique. Les valeurs obtenues se situent dans le rang de le FWHM des analyses expérimentales.

Livraison du cargo dans les nanoparticules creuses

Les nanoparticules creuses obtenus par la réaction galvanique ont été utilisés pour les études de livraison du cargo. Nous avons observé que les différentes morphologies des sous-particules présentées dans les nanoparticules creuses affectent directement le chargement et la livraison du cargo.

Les nanoparticules creuses plus petits ont montré que la seule morphologie de sous-particule menant à la livraison du cargo est celle des structures avec des coins ouverts. Les grandes nanoparticules creuses ne libèrent pas dans aucune structure, y compris celle avec des pores dans la facette de la nanoparticule. L'absence de livraison du cargo est en cours à la présence de PVP sur les morphologies des sous-particules. Nous avons observé que le PVP s'accumule sur les bords des sous-particules, provoquant le blocage de la structure et empêchant le chargement du cargo. Cependant, l'accumulation de PVP est minimisée sur les sous-particules plus grandes telles que les coins ouverts, le contrôle du chargement du cargo et les mécanismes de livraison. De cette manière, nous avons synthétisé des nanoparticules creuses avec des coins ouverts (pour comparer avec les modèles petits), et nous avons observé qu'ils étaient capables de libérer le cargo, comme dans les nanoparticules creuses petits.

La quantification de l'area de livraison du cargo dans les nanoparticules creuses petits et grands a montré qu'en augmentant le nombre de coins ouverts, la livraison du cargo augmente. Cependant, la structure creuse avec 4 coins ouverts a montré un écart type

important par rapport au reste des nanoparticules, y compris les petites nanoparticules creuses. Ce phénomène s'explique par l'interaction du PVP avec le reste des morphologies des sous-particules. Les petits trous seront plus affectés par l'accumulation de PVP que les plus grands. La formation et la variation du diamètre des trous présentés dans les coins ouverts, explique l'effet du PVP sur cette caractéristique des sous-particules et leur contribution aux mécanismes de chargement et de livraison.

L'interaction du faisceau électronique avec les nanoparticules creuses et leur utilisation comme véhicules de transportation du cargo a mis en évidence l'importance des études sur l'électron-matière pour évaluer différents mécanismes. Plus précisément, dans notre méthodologie, nous avons pu élucider que la température s'élève au-dessus de 40 °C parce que c'est le point de fusion de notre matériau à changement de phase (le cargo).

En outre, nous évaluons l'effet sur la livraison du cargo des nanoparticules creuses en comparant deux substrats différents. Le substrat isolant, représenté par SiO₂, a montré une livraison du cargo plus que celui qui possède une conductivité thermique plus élevée, le graphène. Cela suggère que les substrats isolants auront un effet majeur sur l'augmentation locale de la température que les substrats conducteurs et que ce processus affecte la livraison du cargo. Toutefois, nos conclusions portent sur l'importance des différentes études qui peuvent être réalisées en microscopie électronique. L'interaction du faisceau électronique avec l'échantillon entraînera une augmentation de la température du système. Ainsi, l'observation des différents mécanismes par cette technique de caractérisation doit tenir compte de ce facteur.

TABLE OF CONTENT

ACKNOWLEDGEMENTS	III
RÉSUMÉ	V
ABSTRACT	VII
SOMMAIRE RÉCAPITULATIF	IX
INTRODUCTION.....	IX
CHAMP D'ETUDE	XII
SYNTHESE ET LES ETUDES STRUCTURALES DES NANOPARTICULES CREUSES	XIII
ÉTUDES STRUCTURELLES DES NANOPARTICULES CUBIQUES CREUSES	XV
NANOPARTICULES CREUSES COMME VEHICULES DE LIVRAISON DU CARGO	XVI
TECHNIQUES D'IMAGERIE POUR LES APPLICATIONS DE LIVRAISON DU CARGO.....	XVII
<i>Microscopie à force atomique (AFM)</i>	<i>xvii</i>
<i>Microscopie électronique</i>	<i>xvii</i>
SYNTHESE DES NANOPARTICULES CUBIQUES D'AG	XVIII
SYNTHESE DES NANOPARTICULES CREUSES	XVIII
<i>Caractérisation des nanoparticules creuses</i>	<i>xix</i>
SIMULATION ÉLECTRODYNAMIQUE	XIX
SYNTHESE DES NANOPARTICULES CREUSES MODIFIÉES.....	XIX
CHARGEMENT DU CARGO DANS LES NANOPARTICULES CREUSES.....	XX
<i>IN-SITU</i> LIVRAISON DU CARGO DES NANOPARTICULES CREUSES	XX
<i>Comparaison du substrat sur la livraison du cargo</i>	<i>xxi</i>
ANALYSES DES MET IMAGES EN CHAMP CLAIR.....	XXI
DETECTION DE PVP SUR LA SURFACE DES NANOPARTICULES CREUSES	XXI
TABLE OF CONTENT	XXXI
LIST OF FIGURES	XXXV
LIST OF TABLES	XLIII
LIST OF EQUATIONS	XLIV
LIST OF PUBLICATIONS, CONFERENCES, AND AWARDS	XLV
ABBREVIATIONS	XLVII
1 INTRODUCTION	1
1.1 INORGANIC DVs.....	6
1.2 HOLLOW-MNPs AS THERMAL-CARGO DELIVERY VEHICLE?.....	6
1.2.1 <i>General overview of cargo delivery on hollow-MNPs</i>	<i>8</i>
1.2.2 <i>Galvanic replacement reaction (GRR)</i>	<i>10</i>
1.3 ELECTRON MICROSCOPY	11

1.3.1	<i>Transmission electron microscopy (TEM)</i>	12
1.3.2	<i>Imaging modes in TEM</i>	13
1.3.3	<i>Scanning transmission electron microscopy</i>	14
1.3.4	<i>Electron energy loss spectroscopy (EELS)</i>	16
1.4	ELECTRON-MATTER INTERACTION THROUGH ELECTRON MICROSCOPY	18
1.4.1	<i>The heating mechanism for electron-matter interaction</i>	21
1.4.2	<i>Thermodynamics of heating through electron-matter interaction using a TEM</i>	22
1.4.3	<i>Importance of e-beam heating</i>	25
1.5	SCOPE OF THE STUDY.....	26
1.5.1	<i>Hypothesis</i>	27
2	LITERATURE REVIEW	29
2.1	SYNTHESIS AND STRUCTURAL STUDIES OF HOLLOW-MNPs	29
2.2	STRUCTURAL STUDIES OF CUBIC HOLLOW-MNPs.....	35
2.3	HOLLOW-MNPs AS CARGO DELIVERY ACTUATORS.....	38
2.4	IMAGING TECHNIQUES FOR CARGO DELIVERY APPLICATIONS.....	41
2.4.1	<i>Atomic force microscopy</i>	41
2.4.2	<i>Electron microscopy</i>	42
2.5	THERMAL STUDIES OF E-BEAM INTERACTIONS	43
3	MATERIALS AND METHODS	45
3.1	SYNTHESIS OF SILVER NANOCUBES (AGNCs).....	45
3.2	SYNTHESIS OF HOLLOW-MNPs	46
3.2.1	<i>Characterization of hollow-MNPs</i>	46
3.3	ELECTRODYNAMIC SIMULATION.....	47
3.4	SYNTHESIS OF A MODIFIED LARGE HOLLOW-MNP.....	49
3.5	CARGO LOADING INTO HOLLOW-MNP	49
3.6	<i>IN-SITU</i> CARGO DELIVERY OF HOLLOW-MNPs	50
3.6.1	<i>Substrate comparison for the cargo delivery</i>	51
3.7	<i>EX-SITU</i> CARGO DELIVERY OF HOLLOW-MNPs.....	51
3.8	DATA ANALYSIS OF BRIGHT-FIELD TEM IMAGES.....	51
3.8.1	<i>Electron dose calculations</i>	52
3.9	SURFACE DETECTION OF PVP ON HOLLOW-MNPs.....	52
4	RESULTS AND DISCUSSION	53
4.1	STRUCTURAL CHARACTERIZATION	53
4.2	OPTICAL CHARACTERIZATION	60
4.2.1	<i>Structural and alloy effect on the optical properties of hollow-MNPs</i>	61

4.2.2	<i>Effect of structural properties of hollow-MNPs on the hybridization of the plasmonic modes</i>	66
4.3	CARGO RELEASE OF HOLLOW-MNPs.....	71
4.3.1	<i>Structural characterization of hollow-MNPs by bright-field TEM imaging</i>	73
4.3.2	<i>Cargo detection on small and large hollow-MNPs</i>	78
4.3.3	<i>Structural characterization of large hollow-MNPs (modified particle)</i>	84
4.4	CARGO DELIVERY QUANTIFICATION FOR SMALL AND LARGE HOLLOW-MNPs.....	86
4.4.1	<i>Small hollow-MNPs cargo delivery</i>	86
4.4.2	<i>Large hollow-MNPs cargo delivery (modified particle)</i>	90
4.4.3	<i>The area release rate for hollow-MNPs</i>	97
4.4.4	<i>Effect of substrate on cargo release</i>	98
5	CONCLUSIONS	103
5.1	STRUCTURAL ANALYSIS OF HOLLOW-MNPs.....	103
5.2	CARGO DELIVERY OF HOLLOW-MNPs.....	104
5.3	PERSPECTIVES	105
5.3.1	<i>Structural studies of hollow-MNPs</i>	105
5.3.2	<i>Dynamics studies of single hollow-MNPs</i>	106
5.3.3	<i>Cryo-TEM studies of single hollow-MNPs</i>	106
5.3.4	<i>Nanothermometer development</i>	107
5.3.5	<i>Cargo delivery studies</i>	107
6	REFERENCES	109
7	APPENDIX	131
7.1	APPENDIX I.....	131
7.2	APPENDIX II.....	134

LIST OF FIGURES

FIGURE 1.1 DRUG DELIVERY MECHANISMS OF THE ESSENTIAL DV NOWADAYS. DIFFUSION: THE DRUG IS RELEASED IN TIME BY THE REMOVAL OF THE HYDROGEL PROTECTING THE POLYMER RESERVOIR. SOLVENT-INTERACTION: THE SOLVENT INFLUX BY OSMOSIS INTO THE CORE OF THE RESERVOIR (E.G., WATER), PROPITIATING THE DRUG'S RELEASE. BIOCHEMICAL REACTIONS: PH, ORGANIC-GROUPS, AND ENZYMATIC REACTIONS INITIATE THE DRUG RELEASE BY BREAKING THE DRUG-HOST LINKED STRUCTURE. STIMULI-CONTROLLED MECHANISMS: MODIFICATION OF THE STRUCTURE THROUGH DIFFERENT PARAMETERS INITIATING THE DELIVERY, SUCH AS HEAT, SONICATION, LIGHT, AND MAGNETIC FIELDS.	4
FIGURE 1.2 EFFECTIVE ATTENUATION COEFFICIENT SPECTRUM COMPARING THE DIFFERENT TISSUES OF THE ORGANISM AND THE RANGE OF THE FIRST AND SECOND BIOLOGICAL WINDOWS. THE ABSORPTION RANGE OF SOME METALLIC AND SPECIFIC NANOPARTICLES ARE SHOWN AND COMPARED AGAINST THEIR LOCATION IN THE SPECTRA, SHOWING THAT HOLLOW-MNPS (BASED ON AN AU/AG ALLOY) AND AUNRS ARE SUITABLE NANOMEDICINE APPLICATIONS. ADAPTED FROM "SECOND WINDOW FOR IN VIVO IMAGING" BY A. SMITH, M. MANCINI, AND S. NIE, 2009, NAT NANOTECHNOL, 4(11), COPYRIGHT (2009) BY SPRINGER NATURE. [40]	8
FIGURE 1.3 GENERAL OVERVIEW OF THE LOAD AND DELIVERY OF THE DRUG FROM A HOLLOW-MNP. AFTER THE NANOPARTICLE IS IRRADIATED WITH A PULSED LASER, HEAT IS PRODUCED AND TRANSFERRED TO THE SURROUNDED MEDIA. THE HEAT STIMULATES THE DRUG INSIDE THE HOLLOW-MNP, AND IT CAUSES THE EXPULSION FROM THE NANOSTRUCTURE.	9
FIGURE 1.4 SCHEMATIC REPRESENTATION OF A TEM MICROSCOPE SHOWING THE PARTS THAT CONFORM TO THIS EQUIPMENT. ADAPTED FROM VISION AND VISUAL SERVOING FOR NANOMANIPULATION AND NANOCHARACTERIZATION IN SCANNING ELECTRON MICROSCOPE. MARTURI N. 2013. [69]	13
FIGURE 1.5 SCHEMATIC REPRESENTATION OF THE STEM CHARACTERIZATION. IN THIS IMAGE, THE DIFFERENT DETECTORS ARE SHOWN, AND HOW THE E-BEAM INTERACTS WITH THE SAMPLE IS ALSO PRESENTED. EXTRA DETECTORS SUCH AS ELECTRON ENERGY LOSS (FOR EELS SPECTROSCOPY) CAN ALSO BE USED.	16
FIGURE 1.6 SCHEMATIC REPRESENTATION OF A GIF CAMERA USED TO ANALYZE THE ENERGY LOSS BY AN ELECTRON WHEN INTERACTS WITH A SPECIMEN. FIRST, ELECTRONS PASS THROUGH AN APERTURE TO BE RE-DIRECTED IN THE PRISM TO THE ENERGY FILTERS (GREEN RECTANGLES) THEN THE DEFLECTOR POSITIONS THE ELECTRONS THROUGH THE CCD CAMERA. IMAGE USED FROM "FAST SIMULTANEOUS ACCESS TO MULTIPLE	

ANALYTICAL TEM DATA STREAMS WITH GIF TRIDIEM AND STEMPACK," MIKE KUNDMANN, GATAN INC. 2011.	17
FIGURE 1.7 SCHEMATIC REPRESENTATION OF THE INELASTIC INTERACTION. A) A FAST ELECTRON HAS A NEAR-FIELD INTERACTION WITH THE FREE ELECTRONS OF A METALLIC NANOPARTICLE (MNP). B) THE ELECTRON LOSES ENERGY, AND THE LSPR IS EXCITED. C) THE LSPR DECAYS: I) RADIATIVELY, BY EMITTING A PHOTON ($h\nu$), II) OR NON-RADIATIVELY, WHEN THE ELECTRON ENERGY IS ABSORBED INTERNALLY, AND IT CAN BE DISSIPATED IN DIFFERENT MECHANISMS SUCH AS HEAT.	19
FIGURE 1.8 GENERAL OVERVIEW OF A UEM. PUMP-PULSES IRRADIATE THE CATHODE, AND THE PHOTOELECTRIC PROCESS IS INITIATED, PRODUCING ELECTRON PULSES. PROBE-PULSES INTERACT WITH THE SPECIMEN, WHICH IS ALSO INTERACTING WITH THE ELECTRON PULSES AT DIFFERENT TIMES.	20
FIGURE 1.9 SCHEMATIC REPRESENTATION OF THE INTERACTION BETWEEN SWIFT ELECTRONS (TRANSMITTED ELECTRONS FOR TEM ANALYSIS) AND ATOMS. WHEN A SWIFT ELECTRON INTERACTS WITH AN ELECTRON FROM AN ATOM, IT PRODUCES INELASTIC SCATTERING AND X-RAYS; WHEN IT INTERACTS WITH THE ATOMIC NUCLEUS, IT PRODUCES BACKSCATTERED ELECTRONS AND ELASTIC SCATTERING.	21
FIGURE 1.10 THE INCREASE OF TEMPERATURE (ΔT) THROUGH DIFFERENT ELECTRON BEAM CURRENTS AND THERMAL CONDUCTIVITY VALUES (K) OF DIFFERENT SPECIMENS. THE DOTTED LINES SHOW THE DIFFERENT AND MOST COMMON ELECTRON SOURCES THAT ARE FOUND IN TEM. IMAGE USED FROM YOUNG, L "HEAT GENERATION/TEMPERATURE INCREASE BY ELECTRON IRRADIATION." HTTPS://WWW.GLOBALSINO.COM (2021). [104]....	25
FIGURE 2.1 SCHEMATIC DETAILING OF THE MAJOR STEPS THAT GALVANIC REPLACEMENT REACTION FOLLOWS. PINHOLE FORMATION AND AG DISSOLUTION (I), THE FORMATION OF AG-AU WALLS AND VOID SIZE INCREMENT (II), THE FORMATION OF THE TRUNCATED WALLS AND FULL VOID SIZE DEVELOPMENT (III), THE DISSOLUTION OF ALLOYED AG ATOMS, AND FORMATION OF PORES (IV) AND THE FORMATION OF THE PORES IN THE TRUNCATED CORNERS AND DIAMETER INCREMENT FOR SMALL PORES (V). ADAPTED FROM "GALVANIC REPLACEMENT REACTION: A SIMPLE AND POWERFUL ROUTE TO HOLLOW AND POROUS METAL NANOSTRUCTURES" BY X. LU, J. CHEN, AND S. SKRABALAK, 2007, JOURNAL OF NANOENGINEERING AND NANOSYSTEMS, 221(1), COPYRIGHT (2009) BY SAGE PUBLICATIONS. [122].....	30
FIGURE 2.2 SCHEMATIC REPRESENTATION OF THE DIFFERENT SUB-PARTICLE MORPHOLOGIES OF CUBIC HOLLOW-MNPS BY CHANGING THE AG TEMPLATE FROM A) SHARP CORNERS AND B) ROUNDED CORNERS.	36
FIGURE 2.3 SUB-PARTICLE MORPHOLOGIES OBSERVED BY GENÇ ET AL. [125]. I) SILVER TEMPLATE, II) BEGINNING OF THE GALVANIC REPLACEMENT REACTION, III) PINHOLE	

NANOCUBE FORMATION (IN THE FRONT AND BACK FACETS), IV) SINGLE-WALLED AND FULL VOID DEVELOPMENT AND V) NANOFRAME FORMATION. CHANGES WERE OBSERVED BY INCREASING THE CONCENTRATION OF HAUCL ₄	37
FIGURE 2.4 SCHEMATIC REPRESENTATION OF THE STEPS INVOLVING <i>LOADING</i> THE CARGO INTO THE HOLLOW-MNPS <i>VIA</i> THE PCM METHOD. FIRST, THE PCM MATERIAL IS MELTED AND MIXED WITH THE DRUG/DYE (CARGO). THEN HOLLOW-MNPS ARE ADDED, AND IT ALLOWS THE INCORPORATION OF THE CARGO. THE CARGO+HOLLOW-MNPS ARE EXTRACTED WITH WATER DUE TO THE POLARITY DIFFERENCE.....	39
FIGURE 2.5 BRIGHT-FIELD TEM IMAGES FOR THE HOLLOW-MNPS SYNTHESIZED BY MOON ET AL. [149] BEFORE (A) AND AFTER (B) THE CARGO LOADING PROCESS. THE SCALE BAR IS 20 NM. ADAPTED FROM "A NEW THERANOSTIC SYSTEM BASED ON GOLD NANOCAGES AND PHASE-CHANGE MATERIALS WITH UNIQUE FEATURES FOR PHOTOACOUSTIC IMAGING AND CONTROLLED RELEASE" BY G. MOON ET AL., 2011, JOURNAL OF THE AMERICAN CHEMICAL SOCIETY, 133, COPYRIGHT (2011) BY ACS PUBLICATIONS.	40
FIGURE 4.1 STRUCTURAL CHARACTERISTICS OF (A) AGNCS TEMPLATE AND (B) ITS CORRESPONDING HOLLOW-MNPS, VISUALIZED <i>VIA</i> SEM IMAGING. C) ANALYSES OF A SINGLE HOLLOW NANOCUBE. D) INTENSITY PROFILES THAT CORRESPOND TO THE REGIONS SHOWN IN C). THE SCALE BAR IN A) IS 500 NM, AND IN C) IS 50 NM. THE DOTTED RED SQUARE IN B) DENOTES THE PARTICLE IN C).....	54
FIGURE 4.2 EVOLUTION OF TOTAL PARTICLE SIZES AND WALL THICKNESSES OF HOLLOW-MNPS AS A FUNCTION OF HAUCL ₄ CONCENTRATION FOR SMALL AND LARGE AGNC TEMPLATES. A) TOTAL PARTICLE SIZE AND WALL THICKNESS REMAIN THE SAME WITH HAUCL ₄ . INNER AND OUTER WALLS ALSO REMAIN THE SAME. B) TOTAL PARTICLE SIZE INCREASES LINEARLY WITH HAUCL ₄ CONCENTRATION, BUT THE TOTAL WALL THICKNESS REMAINS THE SAME.....	56
FIGURE 4.3 STRUCTURAL EVOLUTION OF THE SUB-PARTICLE FEATURES, VOIDS, AND PINHOLES, WITH INCREASING HAUCL ₄ CONCENTRATION (INCREASES FROM LEFT TO THE RIGHT) FOR THE SMALL (TOP) AND LARGER TEMPLATES (BOTTOM).....	57
FIGURE 4.4 HIGH RESOLUTION-TEM (HR-TEM) IMAGES FOR THE REPRESENTATIVE HOLLOW-MNPS FOR THE SMALL (A, B, C) AND LARGE (D, F, G) TEMPLATES DEPENDING ON THE HAUCL ₄ CONCENTRATION INCREASE FROM LEFT TO RIGHT.....	59
FIGURE 4.5 A) REPRESENTATIVE HIGH-RESOLUTION TEM IMAGE OF A HOLLOW-MNP SYNTHESIZED USING THE SMALL TEMPLATE AND 0.062 MM OF HAUCL ₄ . B) PARTICLE'S FOURIER TRANSFORM IN (A) SHOWING A LATTICE MEASURED AT 5 NM ⁻¹ FROM THE CENTER. C) ZOOMED-IN IMAGE OF THE REGION SHOWN IN (A). D) LINE PROFILE ACROSS THE ATOMIC COLUMNS REVEALS AN INTERPLANAR SPACING OF 0.2 NM.....	60

FIGURE 4.6 ABSORBANCE SPECTRA OF AGNCS (BLACK) AND HOLLOW-MNPS FOR THE A) SMALL AND B) LARGE TEMPLATES AT DIFFERENT CONCENTRATIONS OF HAUCL₄. THE MAIN LSPR PEAK HAS A RED SHIFTING IN BOTH TEMPLATES BY INCREASING THE CONCENTRATION OF HAUCL₄ DURING THE GRR. 61

FIGURE 4.7 LSPR PEAK WAVELENGTH FROM THE EXPERIMENTAL ABSORBANCE SPECTRA AS A FUNCTION OF HAUCL₄. THEORETICAL RESULTS FOR VARIOUS STRUCTURES SHOWN AT THE TOP, WHICH CORRESPONDS TO EXPERIMENTAL STRUCTURES, WITH A TOTAL WALL THICKNESS OF 7.5 NM (BLUE) AND 3.75 NM (RED) FOR THE SMALL TEMPLATE IN A); 10 NM (BLUE) AND 5 NM (RED) FOR THE LARGE TEMPLATE IN B). 63

FIGURE 4.8 SCHEMATIC REPRESENTATION OF A PLASMON HYBRIDIZATION MECHANISM (A) WITH THICK (B) AND THIN (C) SHELLS. THE GENERAL EXPLANATION IS DESCRIBING THE PLASMONS THAT A METAL NANOSHELLS SHOWS, DUE TO THE COUPLING BETWEEN THE ANTI-SYMMETRICALLY MODE (Ω_+) AND SYMMETRICALLY MODE (Ω_-). THE HYBRIDIZATION IS ENHANCED WHEN IF A THICK METALLIC SHELL (B) GETS THINNER (C). ADAPTED FROM “PLAYING WITH PLASMONS: TUNING THE OPTICAL RESONANT PROPERTIES OF METALLIC NANOSHELLS”. HALAS N. CAMBRIDGE UNIVERSITY PRESS. 2011. [187]..... 64

FIGURE 4.9 A) OPTICAL RESPONSE OF NANOCUBE ENSEMBLES: ABSORBANCE SPECTRA OF AGNCS TEMPLATES AND HOLLOW-MNPS. B) OPTICAL SPECTRA COMPARISON BETWEEN EXPERIMENTAL AND THEORETICAL RESULTS. THE THEORETICAL SIMULATION WAS PERFORMED FOR A PARTICLE WITH A TOTAL SIZE OF 75 NM AND AN INNER/OUTER WALL COMPOSITION OF AG (PURE)/ AU₉₀AG₁₀ WITH A VOID ALONG THE Z-DIRECTION. 65

FIGURE 4.10 WEAK COUPLING. OPTICAL CROSS SECTIONS (σ) AND DOMINANT DIPOLAR (p) AND QUADRIPOlar (Q) MOMENTS OF THE CHARGE DISTRIBUTION IN THE PARTICLE WITH A 55X55X20 NM VOID (PANEL A) AND A 55X55X55 NM VOID (PANEL B). 68

FIGURE 4.11 STRONG COUPLING. OPTICAL CROSS SECTIONS (σ) AND DOMINANT DIPOLAR (p) AND QUADRIPOlar (Q) MOMENTS OF THE CHARGE DISTRIBUTION IN THE PARTICLE WITH A 65X65X20 NM VOID (PANEL A) AND A 65X65X65 NM VOID (PANEL B). 69

FIGURE 4.12 STRONG COUPLING. INTERACTION CROSS-SECTIONS σ AND SURFACE CHARGES FOR MNPS WITH WALL THICKNESS EQUAL TO ONE HALF THE VALUES PRESENTED IN TABLE 1 AND TABLE 2, SHOWING THE STRONG-COUPLING REGIME BETWEEN THE CHARGES AT THE OUTER AND INNER MNPS’ SURFACES. WE SHOWCASE RESULTS FOR SPECIFIC LIGHT INCIDENCES, ILLUSTRATING THE SPATIAL SYMMETRY OF THE MAIN PLASMONIC MODES. THE DATA HAS BEEN CHOSEN FROM REPRESENTATIVE GEOMETRIES WITH FULLY DEVELOPED VOIDS AND HOLLOW SURFACE FEATURES. A) SMALL TEMPLATE, SINGLE PINHOLE. B) SMALL TEMPLATE, SINGLE PINHOLE, EIGHT TRUNCATED HOLES. C) LARGE TEMPLATE, THREE PINHOLES PER FACE. 70

FIGURE 4.13 SCHEMATIC REPRESENTATION OF THE E-BEAM INDUCED CARGO RELEASE PROCESS FROM A HOLLOW-MNP. FIRST, THE HOLLOW-MNP FILLED WITH CARGO IS PLACED INTO A TEM GRID (A). THE PARTICLE IS IRRADIATED UNDER THE E-BEAM (B), INCREASING THE LOCAL TEMPERATURE, CAUSING CARGO MELT (C). 71

FIGURE 4.14 IMAGING PROCESSING THROUGH MATLAB SOFTWARE. BRIGHT-FIELD IMAGES FOR A SMALL HOLLOW-MNP AT INITIAL (A) AND 30 MIN (B) AFTER RELEASE. THE IMAGES ARE TREATED WITH A THRESHOLD THAT WILL SELECT DARKER AREAS THAT WILL BE MASKED (RIGHT IMAGES). THE AREA IS CALCULATED THROUGH THE CONVERSION OF PIXELS TO NANOMETERS. THE SCALE BAR IS 50 NM. 72

FIGURE 4.15 BRIGHT-FIELD IMAGES FOR DIFFERENT SUB-PARTICLES MORPHOLOGIES FOR SMALL HOLLOW-MNPS AFTER THE CARGO LOADING PROCESS. THE COMPARISON IS MADE FOR THE OBSERVABLE SUB-PARTICLE MORPHOLOGIES IN THE STRUCTURE, FOR (A) HALF VOID, (B) THREE OPEN CORNERS (3-OPCO), AND (C) FOUR OPEN CORNERS (4-OPCO). MODELS SHOWN ON THE LEFT REPRESENT THE SUB-PARTICLE MORPHOLOGY FOR THE CORRESPONDING ANALYZED CATEGORY. THE SCALE BAR IS 50 NM. 74

FIGURE 4.16 BRIGHT-FIELD IMAGES FOR DIFFERENT SUB-PARTICLES MORPHOLOGIES FOR SMALL HOLLOW-MNPS WITHOUT A CARGO LOADING PROCESS. THE COMPARISON IS MADE FOR THE OBSERVABLE SUB-PARTICLE MORPHOLOGIES IN THE STRUCTURE, FOR (A) HALF VOID, (B) THREE OPEN CORNERS (3-OPCO), AND (C) FOUR OPEN CORNERS (4-OPCO). MODELS SHOWN ON THE LEFT REPRESENT THE SUB-PARTICLE MORPHOLOGY FOR THE CORRESPONDING ANALYZED CATEGORY. THE SCALE BAR IS 50 NM. 75

FIGURE 4.17 BRIGHT-FIELD IMAGES FOR DIFFERENT SUB-PARTICLES MORPHOLOGIES FOR LARGE HOLLOW-MNPS AFTER THE CARGO LOADING PROCESS. THE COMPARISON IS MADE FOR THE OBSERVABLE SUB-PARTICLE MORPHOLOGIES IN THE STRUCTURE FOR (A) HALF VOID, (B) FULL VOID, AND (C) PORES. THE SCALE BAR IS 50 NM. 76

FIGURE 4.18 BRIGHT-FIELD IMAGES FOR DIFFERENT SUB-PARTICLES MORPHOLOGIES FOR LARGE HOLLOW-MNPS WITHOUT THE CARGO LOADING PROCESS. THE COMPARISON IS MADE FOR THE OBSERVABLE SUB-PARTICLE MORPHOLOGIES IN THE STRUCTURE FOR (A) HALF VOID, (B) FULL VOID, AND (C) PORES. THE SCALE BAR IS 50 NM. 78

FIGURE 4.19 BRIGHT-FIELD IMAGES FOR A SMALL HOLLOW-MNP WITH 1-OPCO. THE HOLLOW NANOPARTICLE IS EXPOSED TO THE E-BEAM (A), THE TEMPERATURE INCREASES, AND THE CARGO IS THEN RELEASED THROUGH THE OPEN CORNER AT 1 MIN (B). THE CARGO COVERS THE PARTICLE AT 3 MIN (C) TO EXPAND AT 6 MIN (D). THE INSERTS SHOW A CONTRAST-COLORED IMAGE THAT DIFFERENTIATES THE CARGO RELEASE (RED COLOR) FROM THE HOLLOW-MNP (BLUE COLOR). 79

FIGURE 4.20 HAADF IMAGES AND STEM-EELS ANALYSIS FOR SMALL (A) AND LARGE (B) HOLLOW-MNPS. THE RED ARROW INDICATES THE ORDER OF THE LINE SCAN OF THE ANALYSIS. THE

HISTOGRAMS (MIDDLE) AND CONTOUR MAPS (RIGHT IMAGES) ARE REPRESENTED BY THE INITIAL AND FINAL DISTANCES ANALYZED IN THE LINE SCAN. THE CONTOUR MAPS EXHIBIT THE CHARACTERISTIC ENERGY LOSS VALUES FOR CARBON. THE YELLOW DOTTED-CIRCLES INDICATE THE SUB-PARTICLE MORPHOLOGY ANALYZED DURING THE DATA ACQUISITION..... 80

FIGURE 4.21 BRIGHT-FIELD IMAGES FOR DIFFERENT SUB-PARTICLES MORPHOLOGIES FOR CARGO RELEASE OF LARGE HOLLOW-MNPS IN AN EX-SITU EXPERIMENT FOR THE INITIAL RELEASE AFTER 4 H OF HEATING AND 30 MIN AFTER THE CONTACT WITH THE E-BEAM. THE RIGHT IMAGES REPRESENT THE MAGNIFICATION OF THE CORRESPONDING BRIGHT-FIELD IMAGES. THE COMPARISON IS MADE FOR THE OBSERVABLE SUB-PARTICLE MORPHOLOGIES IN THE STRUCTURE FOR (A) HALF VOID, (B) FULL VOID, AND (C) PORES. THE SCALE BAR IS 50 NM. 82

FIGURE 4.22 SCHEMATIC REPRESENTATION OF THE CARGO RELEASE PROCESS FOR SMALL (A) AND LARGE (B) HOLLOW-MNPS IN THE SOLID PHASE AND LARGE (C) HOLLOW-MNPS IN THE LIQUID PHASE. FOR SMALL HOLLOW-MNP, THE PVP DOES NOT COVER THE OPEN CORNERS ALLOWING THE CARGO LOADING AND RELEASE IN BOTH PHASES. LARGE HOLLOW-MNP HAVE A BLOCKAGE OF PORES CAUSED BY THE COLLAPSE OF PVP, AND IT CANNOT RELEASE ANY CARGO. WHEN LARGE HOLLOW-MNPS ARE IN A HOT LIQUID PHASE, THE PVP DOES NOT COVER THE PORES AND ALLOWS THE CARGO RELEASE. THE CARGO LOADING PROCESS IS PRESENTED IN ALL THE STRUCTURES BECAUSE IT TAKES PLACE IN THE LIQUID PHASE, WHERE PVP IS NOT BLOCKING ANY SUB-PARTICLE MORPHOLOGY. 83

FIGURE 4.23 BRIGHT-FIELD IMAGES FOR DIFFERENT SUB-PARTICLES MORPHOLOGIES FOR MODIFIED LARGE HOLLOW-MNPS WITH A CARGO LOADING PROCESS. THE COMPARISON IS MADE FOR THE OBSERVABLE SUB-PARTICLE MORPHOLOGIES IN THE STRUCTURE FOR (A) 1-OPCO, (B) 3-OPCO, (C), AND 4-OPCO. THE SCALE BAR IS 50 NM. 85

FIGURE 4.24 BRIGHT-FIELD IMAGES FOR DIFFERENT SUB-PARTICLES MORPHOLOGIES FOR THE MODIFIED LARGE HOLLOW-MNPS WITHOUT A CARGO LOADING PROCESS. THE COMPARISON IS MADE FOR THE OBSERVABLE SUB-PARTICLE MORPHOLOGIES IN THE STRUCTURE FOR (A) 1-OPCO, (B) 3-OPCO, (C), AND 4-OPCO. THE SCALE BAR IS 50 NM. 86

FIGURE 4.25 BRIGHT-FIELD IMAGES FOR CHARACTERISTIC SMALL HOLLOW-MNPS ANALYZED BASED ON THEIR NUMBER OF OPEN CORNERS. THE YELLOW CIRCLES IDENTIFY THE OPEN CORNERS FOR EVERY CATEGORY. THE SCALE BAR IS 50 NM. 87

FIGURE 4.26 AREA RELEASE RATIO (ARR) ANALYSES FOR THE THREE DIFFERENT CATEGORIES OF SMALL HOLLOW-MNPS. THE STATISTICAL VALUES WERE OBTAINED FROM FOUR TO EIGHT ANALYZED PARTICLES PER CATEGORY. THE CIRCLES REPRESENT THE DATA OBTAINED FROM THE CODE, AND THE DASH LINES CORRESPOND TO THE FITTING THROUGH EXPONENTIAL DECAY FOR EVERY CATEGORY. THE STANDARD DEVIATION IS

REPRESENTED AS A SHADED AREA IN BLACK FOR 4-OPCO, BLUE FOR 3-OPCO, AND RED FOR 1-OPCO.....	88
FIGURE 4.27 BRIGHT-FIELD IMAGES FOR SMALL HOLLOW-MNPS WITH 4-OPCO WITH MULTIPLE SMALL PINHOLES (A) AND LARGE WELL-DEFINED (C) PINHOLE ON THEIR STRUCTURE. AFTER 30 MIN, THE PARTICLE WITH MULTIPLE PINHOLES (B) RELEASED MORE CARGO THAN ITS COUNTERPART (D). THE YELLOW CIRCLES IDENTIFY THE PINHOLES FOR EVERY PARTICLE. SCALE BAR IN (C) IS 50 NM.	90
FIGURE 4.28 BRIGHT-FIELD IMAGES FOR A REPRESENTATIVE LARGE (MODIFIED) HOLLOW-MNPS ANALYZED BASED ON THEIR NUMBER OF OPEN CORNERS. THE YELLOW CIRCLES IDENTIFY THE OPEN CORNERS FOR EVERY CATEGORY. THE SCALE BAR IS 50 NM.....	91
FIGURE 4.29 AREA RELEASE RATIO (ARR) ANALYSES FOR THE THREE DIFFERENT CATEGORIES OF LARGE HOLLOW-MNPS. THE STATISTICAL VALUES WERE OBTAINED FROM FIVE TO TEN ANALYZED PARTICLES PER CATEGORY. THE CIRCLES REPRESENT THE DATA OBTAINED FROM THE CODE, AND THE DASH LINES CORRESPOND TO THE FITTING THROUGH EXPONENTIAL DECAY FOR EVERY CATEGORY. THE STANDARD DEVIATION IS REPRESENTED AS A SHADED AREA IN BLACK FOR 4-OPCO, BLUE FOR 3-OPCO, AND RED FOR 1-OPCO.....	92
FIGURE 4.30 BRIGHT-FIELD IMAGES FOR THE CARGO RELEASE FROM A LARGE HOLLOW-MNP WITH 4-OPCO. THE PARTICLE RELEASES THE CARGO IMMEDIATELY (A). THE RELEASE INCREASES AT 1 MIN (B) AND 5 MIN (C). THE AREA COVERED BY THE CARGO RELEASE STABILIZES AT 15 MIN (D), SIMILAR TO THE RELEASE AT 30 MIN (E).....	93
FIGURE 4.31 BRIGHT-FIELD IMAGES FOR LARGE HOLLOW-MNPS WITH 4-OPCO WITH A LARGE (A) AND SMALL (C) PINHOLE ON THEIR STRUCTURE. AFTER 30 MIN, THE LARGE PINHOLE (B) RELEASED MORE CARGO THAN ITS COUNTERPART (D). SCALE BAR IN (C) IS 50 NM.	94
FIGURE 4.32 HAADF IMAGES AND STEM-EELS ANALYSIS FOR LARGE (A) AND SMALL (B) PINHOLE FOR THE LARGE HOLLOW-MNPS. THE RED ARROW INDICATES THE ORDER OF THE LINE SCAN OF THE ANALYSIS. THE HISTOGRAMS AND CONTOUR MAPS (RIGHT IMAGES) ARE REPRESENTED BY THE INITIAL AND FINAL DISTANCES ANALYZED IN THE LINE SCAN. THE CONTOUR MAPS EXHIBIT THE CHARACTERISTIC ENERGY LOSS VALUES FOR CARBON. THE YELLOW DOTTED CIRCLES INDICATE THE SUB-PARTICLE MORPHOLOGY ANALYZED DURING THE DATA ACQUISITION.....	95
FIGURE 4.33 SCHEMATIC REPRESENTATION OF THE CARGO RELEASE AND LOADING MECHANISMS IN LARGE (MODIFIED) HOLLOW-MNP. SMALL PINHOLES WILL HAVE A HIGHER EFFECT OF PVP ON THE MECHANISMS DUE TO HYDROGEN BONDS AND STERIC HINDRANCE. THIS PHENOMENON IS MINIMIZED IN LARGER PINHOLES CAUSING A MAJOR EFFECT ON CARGO LOADING AND RELEASING, SUCH AS THE OPEN CORNERS.....	97

FIGURE 4.34 COMPARISON OF THE NORMALIZED AREA RELEASE RATES FOR SMALL (LINE) AND LARGE (DOTTED LINE) HOLLOW-MNPS FOR 30 MIN..... 98

FIGURE 4.35 AREA RELEASE RATIO COMPARISON FOR 3-OPCO USING SIO (RED) AND GRAPHENE (BLACK)..... 99

FIGURE 4.36 BRIGHT-FIELD IMAGES OF THE CARGO RELEASE FOR A 3-OPCO HOLLOW-MNPS ON SIO (A) AND GRAPHENE (C) AT 30 MIN; THE RIGHT IMAGES ARE THE CONTRAST-COLORED BRIGHT-FIELD IMAGES FOR SIO (B) AND GRAPHENE (D). SCALE BAR IN (C) IS 50 NM. NOTICE THAT THE GRAPHENE SUBSTRATE CAN BE FOLDED DUE TO ITS THICKNESS, AND HOLLOW-MNP WILL BE TILTED. THE SUB-PARTICLE FEATURES WILL NOT APPEAR AS FLAT SUBSTRATES..... 100

LIST OF TABLES

TABLE 1 COMPARISON AND DEVELOPMENT OF THE REPRESENTATIVE AG TEMPLATES AND THEIR HOLLOW-MNPS COUNTERPARTS. NANOPLATE [135] NANOSPHERE [134] NANOCUBE AND NANOROD [124].	34
TABLE 2 PARAMETERS USED IN THE THEORETICAL CALCULATIONS FOR A SMALL TEMPLATE WITH AN INNER WALL = 4 NM, OUTER WALL = 3.5 NM, AND A TOTAL SIZE OF 54 NM.	48
TABLE 3 PARAMETERS USED IN THE THEORETICAL CALCULATIONS FOR THE LARGE TEMPLATE WITH AN INNER AND OUTER WALL = 5 NM AND A TOTAL SIZE OF 74 NM.	49

LIST OF EQUATIONS

EQUATION 1:	10
EQUATION 2	22
EQUATION 3	23
EQUATION 4	23
EQUATION 5	24
EQUATION 6	52
EQUATION 7	55
EQUATION 8	55
EQUATION 9	73

LIST OF PUBLICATIONS, CONFERENCES, AND AWARDS

Publications

Jesus Valdez, Lucas Vazquez, Zakria Mahfoud, Tugrul Guner, and Aycan Yurtsever. Optical resonances of hollow nanocubes controlled with sub-particle structural morphologies. *Nanoscale*. 2019.

AC Tavares, F Deganello, JG Rivera, J Valdez, GO Gamboa, and A Yurtsever. Oxygen Evolution and Reduction on $\text{La}_{0.5}\text{Sr}_{0.5}\text{Co}_{0.8}\text{Fe}_{0.2}\text{O}_{3-\Delta}$ Perovskites with Tunable Structural Features. *ECS Meeting Abstracts*. 2019.

U Bruno, J Valdez, A Yurtsever, and AC Tavares. Electrochemistry at Tungsten Conical Sharp Tip Electrodes. *ECS Meeting Abstracts*. 2020.

Conferences

Jesus Valdez, Aycan Yurtsever. Synthesis and study of the optical properties for hollow metallic nanoparticles. Symposium Annuel de Chimie Inorganique du Québec. Trois-Rivières, Canada. 2018.

Jesus Valdez, Lucas Vazquez, Aycan Yurtsever. Synthesis of metallic nanoboxes and their optical and structural properties. XXVII International Materials Research Congress. Cancún, Mexico. 2018.

Jesus Valdez, Lucas Vazquez, Zakria Mahfoud, Tugrul Guner, Aycan Yurtsever. Optical resonances of hollow nanocubes controlled with sub-particle structural morphologies. Chemistry conference and exhibition. Quebec, Canada. 2019.

Awards

Best oral presentation. Symposium Annuel de Chimie Inorganique du Québec. Trois-Rivières, Canada. 2018.

Scholarship. Mexico's Council of Science and Technology/Secretariat of Energy (CONACYT/SENER): From 2016 to 2020.

ABBREVIATIONS

Hollow-MNPs	Hollow metallic nanoparticles
UV-Vis-NIRS	Ultraviolet-visible-near infrared
TEM	Transmission electron microscopy
ARR	Area release ratio
DVs	Delivery vehicles
MNPs	Metallic nanoparticles
AuNRs	Gold nanorods
LSPR	Localized surface plasmon resonance
<i>e-e</i>	Electron-electron
<i>e-ph</i>	Electron-phonon
EELS	Energy electron loss spectroscopy
UEM	Ultrafast electron microscopy
e-beam	Electron beam
2D	Two dimension
DW	Debye-Waller effect
3D	Three dimensional
CTAB	Cetyl trimethyl ammonium bromide
BEM	Boundary element method
PCMs	Phase change materials
HIFU	High-intensity focused ultrasound
AFM	Atomic Force Microscopy
SEM	Scanning electron microscopy
HAADF	High-angle annular dark-field imaging

STEM	Scanning transmission electron microscopy
FEM	Finite element method
AgNCs	Silver nanocubes
HR-TEM	High resolution-TEM
FCC	Face centered cubic
UED	Ultrafast electron diffraction
FWHM	Full-width half maxima

1 INTRODUCTION

In the last decades, emerging infectious and chronic diseases have appeared within the population. Those who have a genetic incidence or geographic disadvantage, will suffer of diseases are rapidly increasing diseases or threatens to increase shortly. The concept of finding new routes of treatment for these diseases has been proposed recently. [1, 2]

Nanomedicine is applying nanotechnology to achieve the cure or treat of a medical threat to the population. This science is based on the use of materials on the nanometer scale. It combines physics, chemistry, and biology to solve a challenge that conventional clinical methods cannot achieve. With this science's progression and research on new drugs and drug delivery systems, numerous therapeutic procedures based on nanotechnology have been proposed [3, 4], offering a new advantage to traditional clinical methods. These new therapeutic methods increase drug specificity and diagnostic accuracy. For example, new drug administration routes have been formulated to have a specific action in the payload in specific regions of the organism reducing their toxicity to other normal parts and increasing their bioavailability.

The research on finding or designing new drugs is a promising area that characterizes discovering a new product based on the biological target. Several studies have found the importance of studying different drug release mechanisms to adapt these findings to new and effective treatments in the organism. However, the research on new drugs usually lacks in two essential aspects: bioavailability and bio-selectivity.

Bioavailability is when the absorption of the drug takes place. Each route of administration has factors that can affect drug bioavailability. It is the fraction of the administered dose that reaches the systemic circulation, and here, bio-selectivity plays an important role. Bio selectivity means that the drug can be carried into the organism to a specific place, allowing that the specific drug dose can be decreased due to the improvement of the therapeutic problem's target area/site. The use of "carriers" enables the introduction of a therapeutic substance into the organism. It also improves the drug payload's efficacy and safety by controlling the rate, time, and place of release in the body, something the drugs

lack by themselves. That is why the research on drug delivery systems (DDS) has been necessary for the last few years.

Current research on DDS can be described in four categories:

- Routes of delivery
Drugs can be delivered in different ways, such as oral, inhalation, or absorption administration. Each method possesses distinct advantages and disadvantages, and not all of them are compatible with every drug. Improving the delivery methods or designing new ones can enhance the success in the delivery of every drug.
- Targeting strategies
The target may be whole organs, tissue-based regions, disease forms (such as tumor cells), or structures inside cells (RNA chain). The development of specific-target molecules or structures increases the possibilities of healing a specific area without damaging other parts of the organism.
- Cargo
In addition to drugs, researchers are also exploring the use of genes, proteins, organic molecules, and stem cells as treatments to treat alone or in combination with drugs various diseases.
- Delivery vehicles (DVs)
Researchers have begun to reformulate the paths in drugs that can be delivered in the system to be safer and more compatible in specific conditions. The more targeted a drug is, the lower its chance to affect different parts of the organism. DVs can be combined with cargo and targeting strategies to improve the drug's effectiveness. DVs gain interest lately due to their advantage of using various drugs and their use as secondary treatment agents.

As explained before, DVs allow scientists to find different ways to treat diseases in the organism without changing the drug or improving them. That is why DV became one of the most crucial research nowadays in DDS.

DVs have chemical, physical, and morphological characteristics. Depending on the action, they may have different affinities to different drugs due to their polarities through chemical or physical interactions. All these factors influence the interaction and the kinetic mechanisms of the nanocarriers in different biological systems. [5–7]. Mechanisms of drug delivery are difficult to elucidate because the conventional techniques of characterization focus on a whole assemble of DV, ignoring the differences in morphology, size, and structural details DV may have.

Other parameters, such as the nature of the carriers (e.g., organic, inorganic, and bio-composites) and the form in which drugs can be hosted, such as core-shell or matrix systems, are essential for elucidating their drug delivery profiles [8, 9]. The critical mechanism profiles of drug delivery can be divided into four categories, which are diffusion, solvent-interaction, chemical reaction, and stimuli-controlled release [10].

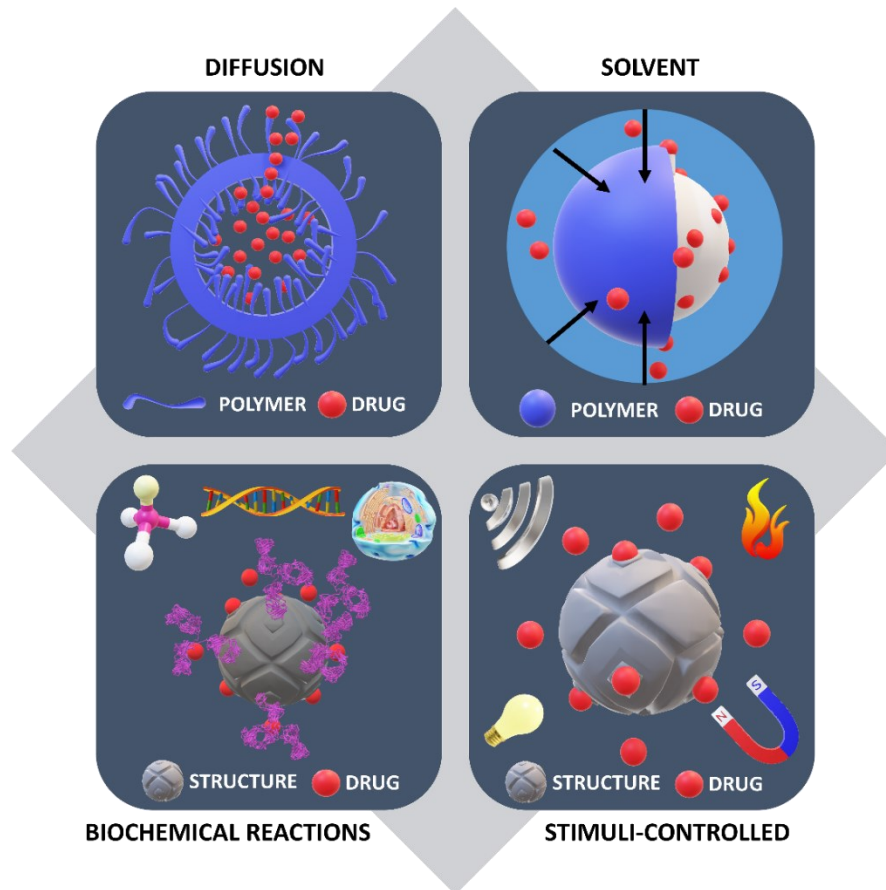


Figure 1.1 Drug delivery mechanisms of the essential DV nowadays. Diffusion: The drug is released in time by the removal of the hydrogel protecting the polymer reservoir. **Solvent-interaction:** the solvent influx by osmosis into the core of the reservoir (e.g., water), propitiating the drug's release. **Biochemical reactions:** pH, organic-groups, and enzymatic reactions initiate the drug release by breaking the drug-host linked structure. **Stimuli-controlled mechanisms:** modification of the structure through different parameters initiating the delivery, such as heat, sonication, light, and magnetic fields.

Although there are different drug release mechanisms, strategies are mainly based on improving the nanostructures' specificity to target regions in the organism [11, 12]. That is why all these four categories of mechanisms are under research to achieve this task. Nowadays, the strategies that are currently under study for an optimal drug release are based on the coating or chemical functionalization of the host structures with several materials [13]–[15]. This functionalization allows drugs to be delivered in a particular

environment. However, the creation of a ligand based-drug delivery is difficult, and several designs must be performed previously (such as solvent and diffusion mechanisms), which lead to a lack of interaction with the type of disease and poor biocompatibility with the organism or tissue design [1]. Besides, due to different DVs' physicochemical characteristics, it has been difficult to standardize the mechanism of release in the organisms [1, 16].

Stimuli-based DVs have shown the ability to control the release of drugs when they are exposed to external factors such as ultrasound [17–19], heat [20, 21], magnetism [22, 23], light [22, 24, 25]. These simulations allow controlling the release of the drug outside the DV. The biochemical reactions and stimuli-based mechanisms represent nanomedicine's most promising research nowadays. They combine different mechanisms' properties for single systems, enhancing the performance of the drug delivery. However, the information about this system's action mechanisms is little known due to the physical limitations of conventional characterization techniques (e.g., ensemble, segmented, or single nanoparticle analyses).

Based on their physicochemical properties, stimulated-DV can be divided into two groups:

- Organic
Organic DVs are carbon-based nanomaterials that are generally characterized by a high drug loading capacity. They allow flexible control of both morphology and chemical composition. However, colloidal stability plays an essential role in organic DVs applications; it means that these carriers can only be used in systems to allow their surveillance until they reach the specific target.
- Inorganic
Inorganic DVs represent the most versatile way of drug delivery. They can be synthesized more broadly: from silica and magnetic nanoparticles to metallic nanostructures. These DVs are resistant to different organisms' changes and can load different types of drugs. Besides, the ease of synthesis and their adaptability

to different media, making them the most suitable structures to be used in drug delivery approaches.

Moreover, the different properties of inorganic and organic DVs and their combinations provide significant advantages offering the specific functionalities of organic materials at the surface of inorganic NPs. For example, inorganic nanoparticles can be coated with polymers to be functionalized with biomolecules, enhancing the inorganic nanostructures' selectivity and efficiency [26–28].

1.1 Inorganic DVs

Inorganic nanoparticles have unique properties that make them attractive for drug delivery purposes. Inorganic DVs are non-toxic, biocompatible, and very stable structures compared to organic DVs.

Many inorganic structures have been proposed to be DV's [29–32]. However, hollow-MNPs possess essential properties to be used for delivery purposes and the possibility to carry the drug inside their structures; this allows protecting the drug to the media in which it is going to be released. The time over-controlled drug release that hollow-MNPs can provide is the most important property suitable for biological purposes.

1.2 Hollow-MNPs as thermal-cargo delivery vehicle?

Research on metallic nanoparticles (MNPs) supporting plasmonic resonances has seen a surge in the last decades. Their strong coupling with light has been exploited in various applications, such as creating nanostructured sensors [33] or enhancing light-harvesting devices' efficiency. [34] In particular, hollow-MNPs have been successfully used in catalysis and nanomedicine. As catalysts, hollow-MNPs have been shown to induce a higher catalytic activity than traditional nanoparticles [35, 36] due to their larger available surface, through which they interact with adsorbed reagents.[37] An additional advantage comes from the flexibility to tune their plasmon resonances up to the near IR spectral range without increasing their total size or aspect ratio, a requirement for conventional non-hollow MNPs.[38]

This ability is particularly relevant for nanomedicine applications. Hollow-MNPs can be nanoengineered to absorb light in the biological window [39, 40]. The biological window is the region on the electromagnetic spectrum in which the tissues scatter and absorb less light. In this region, the distance travelled by photons increases within the tissue, and the probability of photon absorption by another system (e.g., DV, drugs, nanoparticles) also increases.

As shown in Figure 1.2, hollow-MNPs and gold nanorods (AuNRs) are the most suitable nanostructures for nanomedicine due to their LSPR in the biological window. However, the advantage of hollow-MNPs over conventional MNPs is that they can be engineered to retain a plasmon resonance even at small sizes that can facilitate cell uptake, a property that MNPs (e.g., AuNRs) do not possess.[41] Consequently, hollow-MNPs are an excellent tool for nanomedicine applications (e.g., imaging, photothermal therapy, and drug delivery). [42–46]

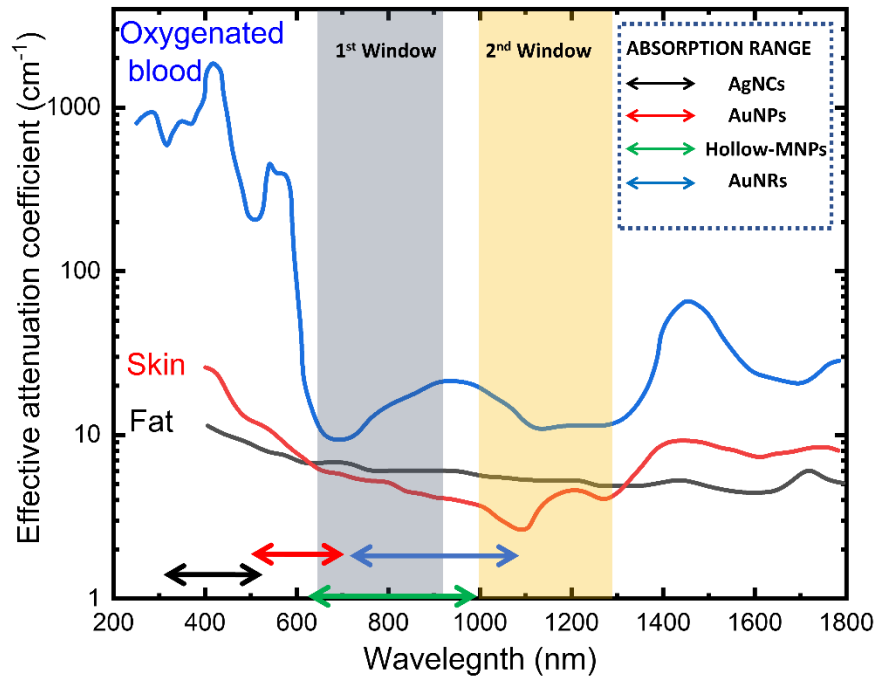


Figure 1.2 Effective attenuation coefficient spectrum comparing the different tissues of the organism and the range of the first and second biological windows. The absorption range of some metallic and specific nanoparticles are shown and compared against their location in the spectra, showing that hollow-MNPs (based on an Au/Ag alloy) and AuNRs are suitable nanomedicine applications. Adapted from "Second window for in vivo imaging" by A. Smith, M. Mancini, and S. Nie, 2009, Nat Nanotechnol, 4(11), Copyright (2009) by Springer Nature. [40]

Functional characteristics of hollow-MNPs, including those mentioned above, depending on the sub-particle structural morphologies that develop through the hollowing process. Therefore, our ability to effectively use such particles in different applications is fundamentally linked to our understanding of their structural details and how they form through the evolution of the relevant chemical processes.

1.2.1 General overview of cargo delivery on hollow-MNPs

In drug delivery, the importance of knowing the structure of the nanoparticle is essential. It allows proposing different routes of loading/delivering the cargo. However, high control over the structure of the composite material is necessary to harness this potential. An

example of the structures' control is the pores' size or pinholes forming in the nanoparticle structure. These pinholes should be large enough to allow the cargo to be loaded and delivered successfully from the nanostructure.

Also, delivery mechanisms for hollow-MNPs have not been explained up to the present, and elucidating these mechanisms is essential to achieve the optimal structure for successful drug delivery. The objective should be to propose and understand the mechanisms for controlling the release's location and timing.

There are different mechanisms by which the delivery is activated. In our case, we will use temperature as the initiator of a delivery. It will be achieved by irradiating the nanoparticle with an e-beam that will heat the particle. This heat is going to be transferred to the cargo, which starts the delivery mechanisms. That is why the study and research of the correlation between optical and thermal properties with the sub-particle morphologies are essential.

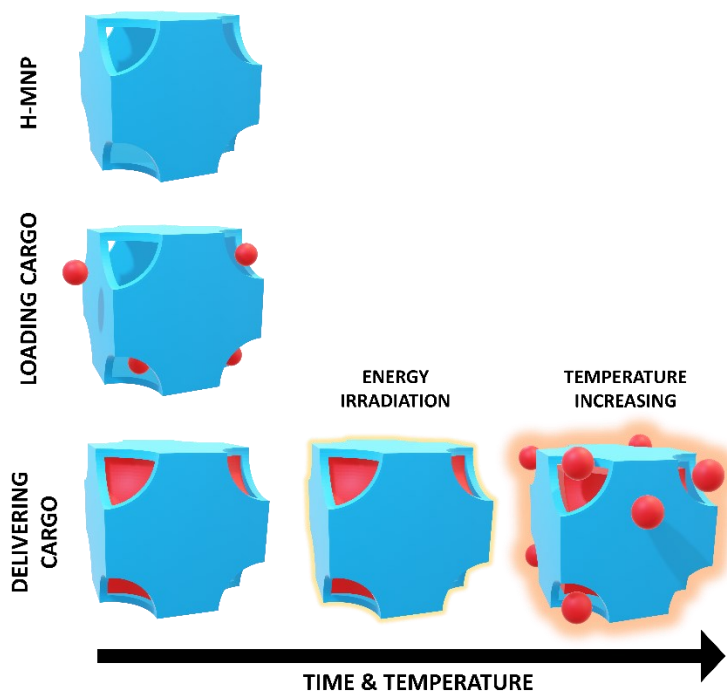
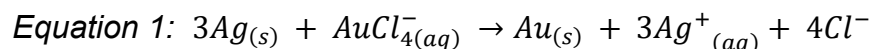


Figure 1.3 General overview of the load and delivery of the drug from a hollow-MNP. After the nanoparticle is irradiated with a pulsed laser, heat is produced and transferred to the surrounded media. The heat stimulates the drug inside the hollow-MNP, and it causes the expulsion from the nanostructure.

1.2.2 Galvanic replacement reaction (GRR)

The structural changes occur through the GRR between Ag and HAuCl₄ species.[47] This process, which has been extensively studied and reported,[48–52] presents a way to synthesize Au/Ag hollow nanoparticles. First, solid Ag cubical nanoparticles (Figure 1A) are synthesized as a template to obtain hollow-MNPs by replacing atomic silver with gold *via* the spontaneous reduction of Au³⁺ with Ag⁰. Differences in the reduction potentials of Au³⁺/Au⁰ and Ag⁺/Ag⁰ enable a spontaneous GRR, which can be described as



At the nanoscale, the reaction begins when an Ag nanoparticle gets in contact with AuCl₄⁻ ions. Then, Ag atoms are oxidized spontaneously and dissolved by AuCl₄⁻ ions, yielding Ag⁺ ions into the reaction's solution. Simultaneously, Au atoms are deposited on the nanoparticle's surface caused by the Au³⁺ ion's reduction (located in AuCl₄⁻ ions). As the Au and Ag are miscible at the nanoscale, both having the same face-centered cubic (FCC) crystal structure and similar lattices constants, an AgAu alloy's formation is expected with varying composition as a function of the concentration of AuCl₄⁻ in the solution. This miscibility implies a diffusion of the metal atoms, governed by many factors, such as the chemical species involved, reaction conditions (e.g., temperature), and physical properties, such as the nanoparticles' size and shape.

It has been observed that GRR co-exists at the nanoscale with a process of diffusion known as the Kirkendall effect, which can lead to more complex hollow structures [49]. Furthermore, as the molar ratio of AuCl₄⁻: Ag increases, dealloying and surface reconstruction processes are initiated [47]. The Kirkendall effect defines the motion of the boundaries between two metals due to an unbalanced diffusion of atoms arising from the species having different diffusion rates. Initially described for bulk systems [53], it was also found to act in the nanoscale. [54] The Kirkendall effect provides a continuous outward material flux with simultaneous vacancies inside the nanoparticles in core-shell systems.[55, 56] Besides, this effect has emerged as an important self-templated strategy for synthesizing hollow nanoparticles. It has been used to synthesize hollow nanostructures with different morphologies (e.g., nanospheres, nanotubes, and

nanocubes), [50, 54, 55, [57, 58] and different compositions (e.g., bimetallic alloys and non-metallic oxides).[59–61]

Moreover, it has been shown that the Kirkendall effect is a size-dependent process, and it can be altered if the nanoparticle has a reduced dimension, which imposes a boundary condition. One example is the defect formation in smaller nanoparticles. At smaller sizes, the defect formation chance at the nanoparticle's surface is higher. It allows an inward diffusion of the atoms presented on the outer surface, being transported by the defect diffusion mechanism.[62, 63] These diffusion mechanisms lead to unlocking different morphological modifications during the galvanic replacement reaction.

As noted above, chemical, and structural transformations occurring through galvanic replacement reaction have drastic effects on the optical spectrum (UV-vis-NIR absorbance) of the hollow-MNPs, with a salient feature being the shift in wavelength of their resonant plasmonic modes. Several studies have already suggested that this shift is due to changes in (a) the chemical composition of the hollow-MNPs due to alloying, (b) their wall thickness, and (c) morphology due to void formation.[38, 64] But these studies remain limited because they have focused on a single type of nanoparticles with a fixed size and only fully developed inner voids. Furthermore, the diversity of pinhole morphologies occurring at the MNPs' surfaces were not addressed. Hence, understanding how sub-particle morphologies affect these nanoparticle ensembles' optical response and how these morphologies depend on other factors is lacking.

1.3 Electron microscopy characterization

Electron microscopy is a characterization technique used to obtain high-resolution images of biological and inorganic specimens. It is used in biomedical research to investigate the structure of cells [65], [66], tissues [67], [68], and macromolecular complexes. This technique's high spatial resolution results from electrons' use (which have very short wavelengths) as the illuminating radiation source. In this technique, different characterizations can be used depending on the sample or the needed information.

This characterization technique represents a suitable way of analyzing very small structural details on nanoparticles, such as the sub-particle morphologies that hollow-

MNPs develop during their synthesis. Additionally, the extra characterization techniques that can be achieved parallel to electron microscopy can help observe different *in-situ* phenomena that hollow-MNPs may present.

1.3.1 Transmission electron microscopy (TEM)

TEM microscopy is an electron technique that uses a small beam of electrons to visualize specimens and generate a magnified image. TEMs can image objects around the nanometric scale. The TEM employs a high voltage electron beam to irradiate a sample and create an image. An electron gun or cathode at the top of the TEM column emits electrons that are accelerated through the microscope's column. The difference with light microscopes is that rather than having a glass lens focusing the light, the TEM uses electromagnetic lenses that focus the electrons to create a small (in diameter) electron beam. This beam interacts with the specimen, and electrons can either scatter or are transmitted. These electrons can be detected through different detectors that are placed in different places in the TEM microscope. Figure 1.4 shows the schematic representation of a TEM microscope and its respective parts.

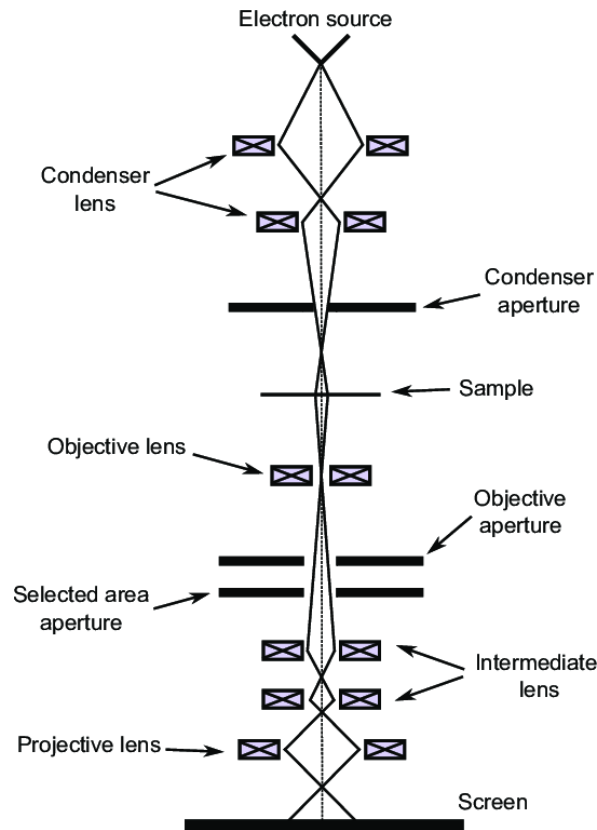


Figure 1.4 Schematic representation of a TEM microscope showing the parts that conform to this equipment. Adapted from Vision and visual servoing for nanomanipulation and nanocharacterization in scanning electron microscope. Marturi N. 2013. [69]

1.3.2 Imaging modes in TEM

1.1.1.1 Bright-field imaging

Bright-field imaging is the most common technique used with a TEM. The imaging process begins when the electron beam interacts with the specimen, some areas of the sample absorb or scatter electrons and appear darker, while other areas that transmit electrons appear brighter. [70] In the bright field image, the transmitted electron beam is selected with the aperture, and the scattered electrons are blocked. Since the transmitted beam is selected, areas with crystalline or high mass materials will appear dark. When an aperture is selected in the bright-field mode, it allows only the direct beam to pass. In this case, the image results from a weakening of the direct beam by interacting with the sample. Therefore, the image's formation depends on its mass-thickness and

diffraction contrast: thick areas, areas in which heavy atoms and crystalline areas appear with dark contrast. [71]

In bright-field TEM, the image's enhanced contrast can be manually tuned via objective apertures or energy filters (depending on the detector/camera). This technique is also suitable for most types of structures, and it is widely used. However, bright field images have their disadvantages. Problems may occur with contrast (which can be fixed by using a smaller objective aperture), and they are not suitable for crystalline structures that are too small.

1.1.1.2 **Dark-field imaging**

Dark-field TEM is the inverse of bright-field TEM. In this TEM mode, the scattered electrons are selected, and the transmitted electrons are excluded. In dark-field imaging, the areas where there are no electron scattering will be darker, and where there are scattered electrons (usually specimen and other materials) will appear brighter [72]. This technique can enhance the contrast compared to a bright field image, which is sometimes not clear enough when crystalline features are too small. This technique can be used to study the crystal lattice, crystal defects, stacking faults, dislocations, and grain sizes.

1.3.3 **Scanning transmission electron microscopy**

Scanning transmission electron microscopy (STEM) is a microscopic technique that combines the principles of transmission and scanning electron microscopies. The STEM technique requires thin samples where there could be a transmission of electrons, and it also analyzes the electrons that are scattered by the interaction with the electron beam and the sample. [73]

The STEM technique scans the specimen with a very small, focused beam of electrons. The pixel size can modify the scan's size if the image to be analyzed, modifying the acquisition time: the higher resolution, longer acquisition time. The interactions between the e-beam and the specimen generate a signal that is correlated with beam position. This correlation is used to create an image in which the signal level is represented by the brightness at the beam's corresponding location in the image. During the electron beam

interaction, various types of scattering are produced. The electrons at high scattering angles are used to form high-resolution, chemically sensitive, Z-contrast images.

One of its principal advantages compared to TEM is that STEM can use other signals that cannot be spatially correlated in TEM. These signals are secondary electrons, scattered electrons, X-rays, and electron energy losses. These signals can be obtained at the same time as the imaging, allowing direct correlation of images and spectroscopic data. However, due to the beam's focused energy, the specimen's interaction can burn organic materials or create carbon contamination. [74], [75]

To analyze these signals, the microscope must have detectors that can collect and correlate this information.

Bright-field detector

It is located at the same place as the aperture in bright-field TEM mode and detects the intensity in the direct beam from the specimen.

Annular dark-field detector

The annular dark-field detector is a hollowed disk where the bright-field detector is placed. The dark-field detector uses scattered electrons for image formation, like the dark-field mode in TEM.

High angle annular dark-field (HAADF) detector

The HAADF detector, like a dark-field detector, is a detector in the form of disk with a hole on its center, but the disk diameter and the hole are much larger than in the dark-field detector. Thus, it detects electrons that are scattered to higher angles. In this detector, the Z contrast is achieved.

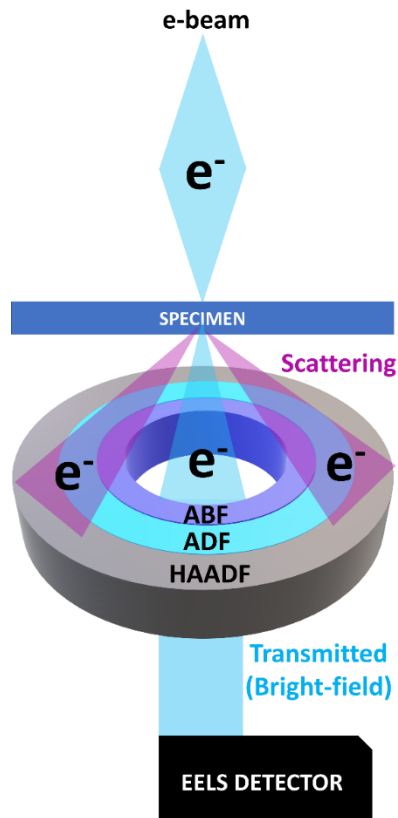


Figure 1.5 Schematic representation of the STEM characterization. In this image, the different detectors are shown, and how the e-beam interacts with the sample is also presented. Extra detectors such as electron energy loss (For EELS spectroscopy) can also be used.

1.3.4 Electron energy loss spectroscopy (EELS)

Electron energy-loss spectroscopy (EELS) is an analytical technique based on the inelastic scattering of fast electrons with a specimen. When this interaction occurs, the electron loses energy, which is then detected through the EELS spectroscopy. This technique can detect the elemental composition and physicochemical properties of different materials, including biological samples. [76], [77]

EELS analyzes the transmitted electrons to determine the amount of energy they have lost when the e-beam interacts with the sample. Due to this phenomenon, information about interaction with atoms that includes elemental information, chemical bonding,

valence, and conduction bands, among others, can be detected by EELS spectroscopy. [78]

Electron energy losses can be measured using a gatan image filter (GIF) to detect materials' compositional and electronic properties. The GIF camera is a setup of energy imaging filters that can be used to acquire either filtered images or electron spectrum on a CCD camera. A magnetic prism chromatically disperses the electrons. The imaged line spectra are converted into a two-dimensional line plot of electron intensity as a function of electron energy loss. Figure 1.6 shows the schematic representation of the GIF camera.

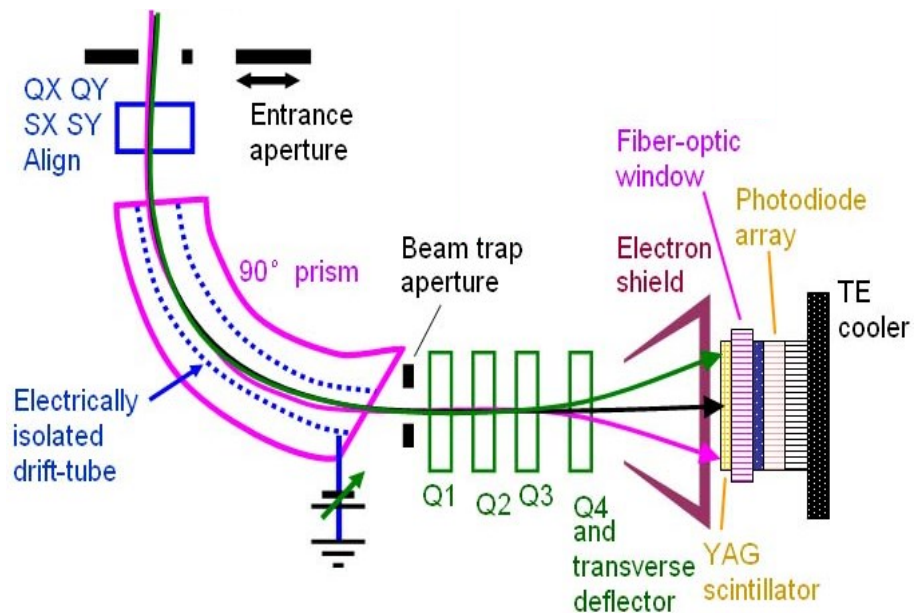


Figure 1.6 Schematic representation of a GIF camera used to analyze the energy loss by an electron when interacts with a specimen. First, electrons pass through an aperture to be re-directed in the prism to the energy filters (green rectangles) then the deflector positions the electrons through the CCD camera. Image used from “Fast simultaneous access to multiple analytical TEM data streams with GIF Tridiem and STEMPack,” Mike Kundmann, Gatan Inc. 2011.

1.4 Electron-matter interaction through electron microscopy

Since the development of electron microscopy through the invention of the transmission electron microscope by Ernst Ruska, this field has been developed by scientists until reaching an ultrahigh sub-Ångstrom spatial resolution. Nevertheless, providing ultrahigh spatial resolution in electron microscopy is not the only goal of this technique; indeed, it is similarly important to characterize material properties at the nanoscale. In nanoscience, where many of the physicochemical processes happen at the nanoscale, electron microscopy offers, through the electron probes, the brightness, emittance, and spatiotemporal resolutions that are needed to study the processes within the time-energy and momentum-space.

Like photon-matter interactions, incident electrons can also experience inelastic interaction with single electrons from the specimen and by collective electron excitations within the sample, like plasmon and photon polaritons result of which they will lose energy. These mechanisms can be observed and measured in a TEM where different characterization techniques, such as energy electron loss spectroscopy (EELS), are based on electron-matter interactions.

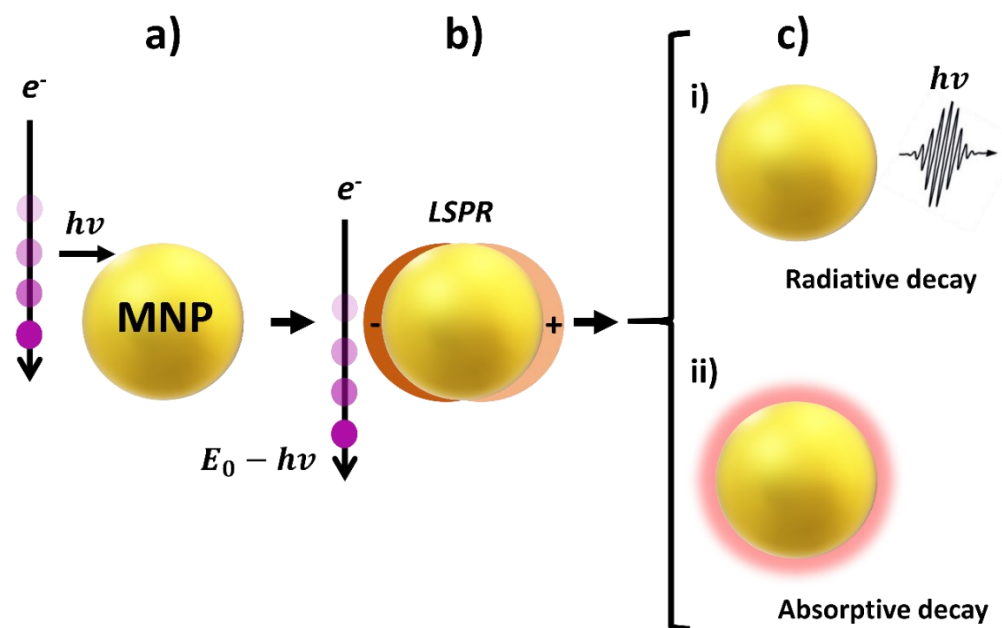


Figure 1.7 Schematic representation of the inelastic interaction. a) A fast electron has a near-field interaction with the free electrons of a metallic nanoparticle (MNP). b) the electron loses energy, and the LSPR is excited. c) The LSPR decays: i) radiatively, by emitting a photon ($h\nu$), ii) or non-radiatively, when the electron energy is absorbed internally, and it can be dissipated in different mechanisms such as heat.

The use of TEM in investigating and characterizing the nanomaterials' physicochemical properties at the nanoscale has been crucial to understand and correlate the processes that explain the behavior of the nanostructures.

In recent years, the development of new TEM techniques aided the study of nanomaterials' unique properties that could not be studied before. These modern microscopes include new additaments such as gaseous chambers [79], heating/cooling holders [66–68], liquid cell holders [83], laser irradiation [70, 71], and new camera detectors that allow scientists to study *in-situ* and *in-vivo* the processes that may occur at different conditions. For instance, many of the electron-matter or photon-matter interactions within nanoparticles occur in the femtosecond regime. The use of a conventional technique such as TEM with an ultrafast laser provides a unique way of characterizing nanoscale mechanisms. The design of such combined techniques led to the birth of the so-called ultrafast electron microscopy (UEM), which is conducted using

a stroboscopic pump-probe approach. In the case of the UEM, pump-probe experiments mean that one laser pulse is used to excite the specimen, and another is used to hit the photocathode to produce the electrons *via* the photoelectric effect. Figure 1.8 shows the essential parts and processes that occurred in the UEM.

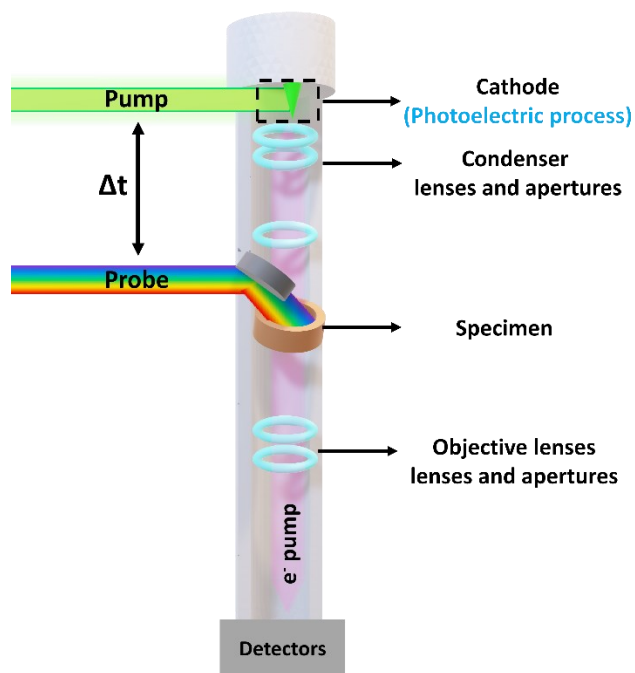


Figure 1.8 General overview of a UEM. Pump-pulses irradiate the cathode, and the photoelectric process is initiated, producing electron pulses. Probe-pulses interact with the specimen, which is also interacting with the electron pulses at different times.

The consolidation of TEM as a characterization technique, apart from its imaging use, drawn attention to the effects that the electron beam (e-beam) has on the processes studied by *in-situ* experimental analysis. It is well known that e-beam damages the sample at high exposure times during TEM imaging [72, 73] or induces a change in the morphology of nanoparticles [74, 75]. However, *in-situ* analysis with the new measurement developments (e.g., heating/liquid holders or gas chambers) possesses different challenges in TEM-based measurements.

For example, it has been found that e-beam increases dislocation activation during *in-situ* experiments in gold and aluminum films [90]. For nano-systems-based characterizations,

the e-beam ionizes gas molecules, increasing their reactivity and modifying the surface of the specimens [77, 78]. In liquid-phase TEM experiments, the e-beam leads to the water's radiolysis, forming reducing and oxidizing species that may potentially modify and destroy specimens [79, 80]. In this fashion, it is particularly important to understand the effect of the e-beam on the samples' behavior.

1.4.1 The heating mechanism for electron-matter interaction

The electron-matter interaction in TEM can be categorized based on energy transfer processes. These processes are the radiolysis, generated due to the inelastic scattering of electron-electron interactions, causing heating, ionization, and X-rays in the specimen. The second process is the elastic scattering produced from the electron-atom interaction, creating point defects due to the atomic displacement. In a general way, the energy transfer by inelastic scattering is reduced at higher e-beam energies, while elastic scattering is increased [95].

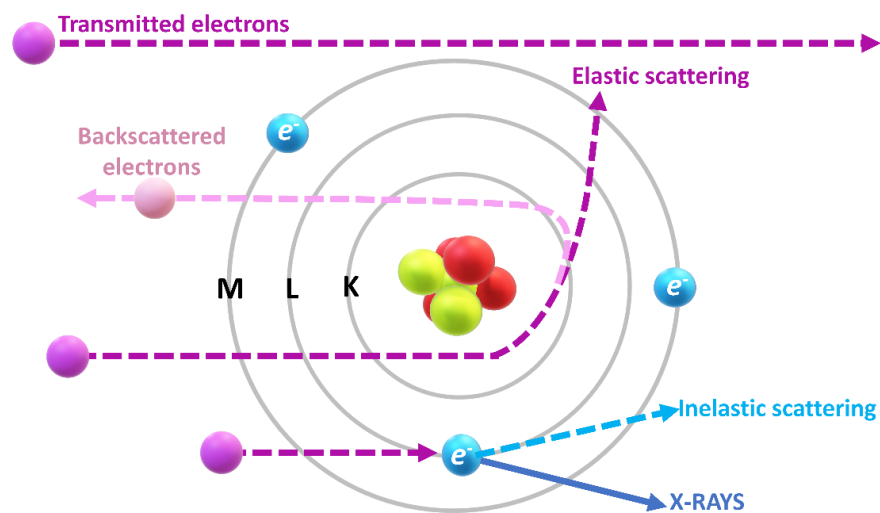


Figure 1.9 Schematic representation of the interaction between swift electrons (transmitted electrons for TEM analysis) and atoms. When a swift electron interacts with an electron from an atom, it produces inelastic scattering and X-Rays; when it interacts with the atomic nucleus, it produces backscattered electrons and elastic scattering.

The interaction between the high e-beam energies and a specimen produces a range of signals that provide various information in electron microscopy. Figure 1.9 shows the

schematic representation of the electron-matter processes and their corresponding signals depending on the electron-matter interaction. The information we can obtain from these interactions is the chemical composition, morphology, and crystalline structures of the specimen. During the electron-matter interaction, heat is also generated, making possible the use of the e-beam as a controllable heating source for the generation of thermal processes at the nanoscale and thermal studies in electron microscopy [82–84].

Electron beam possesses some advantages for its use as a thermal metrology tool for nano-systems. First, the spatial resolution that an e-beam provides is higher than other nanoscale thermal measurements such as thermoreflectance, Raman spectroscopy, and other methods with limitations in the fabrication length scale [85, 86]. The second advantage is the high heat flux that a high-energy e-beam has by focusing it in a small area, which is fundamental in the studies of hotspots, which is essential in the engineering and design of nanoelectronics. The e-beam is dynamically controllable in shape and position, which makes this source important in thermal studies. [101]

1.4.2 Thermodynamics of heating through electron-matter interaction using a TEM

When an electron beam irradiates a specimen, most of the interactions between electrons with atoms result in energy losses. This energy loss includes the heat generated in the irradiated material, increasing the local temperature of analysis compared to the surroundings' temperature. [102], [103]

For TEM analysis, the heat deposited in the specimen per second can be calculated by Equation 2.

$$\text{Equation 2} \quad \Delta Q = \Delta E \cdot (I_{beam}/e) \cdot (t/\lambda)$$

Where ΔE represents the average energy loss per inelastic collision per electron, t is the thickness of the specimen, λ represents the electron mean free path for all inelastic scattering, I_{beam} is electron beam current, and e represents the charge of electron.

In Equation 2, the units of ΔQ will be considered as eV to have similar dimension because the units of ΔE are eV.

At the steady-state of TEM analysis, the heat generation can be balanced by heat loss due to radial thermal conduction and radiation in the vacuum. Thus, we can have:

$$\text{Equation 3} \quad I_{beam} \cdot \Delta E \cdot \frac{t}{\lambda} = \frac{4\pi kt(T-T_0)}{\left(0.58+2\ln\left(\frac{2R_0}{d}\right)\right)}$$

Where I_{beam} the electron beam current, k is the specimen's thermal conductivity, T_0 represents the initial temperature and T the local temperature (final temperature), R_0 is the traveling distance of heat, and d represents the beam diameter. [104]

In Equation 3, some parameters have to be considered depending on the equipment used. One of these parameters is the electron beam diameter (d). This parameter is a major factor in all aspects of electron microscopes, where it can be used as a small, focused beam depending on the characterization or analysis to be performed in a TEM.

This value can be calculated or measured experimentally. The calculation is simple, but the value may vary from different equipment types due to the lack of considerations of setup values for each microscope. The measurement of the diameter is difficult and can be imprecise.

At this moment, there is not a universally accepted definition of the beam diameter. Theoretically, the beam diameter can only be manipulated using a smaller condenser aperture or increasing the condenser lens's excitation. Companies provide values of beam diameters for each condenser or aperture setting. [105]

Unfortunately, these values are calculated and may significantly differ from the actual beam diameter due to the assumption that the electron beam distribution is a Gaussian form. Nevertheless, many parameters such as misalignments and astigmatism in TEM avoid forming a real Gaussian distribution.

If no apertures are considered, the beam diameter could be defined by diffraction of the electron (dominated by wavelength λ) and spherical and chromatic aberration of the electron lenses (mainly the objective lenses). Generally, for a Gaussian beam, the beam diameter is defined by Equation 4: [106]

$$\text{Equation 4} \quad d = \left(\frac{I}{\beta}\right)^{1/2} \cdot \frac{1}{\alpha} + 0.5 \cdot Cs \cdot \alpha^3 + 1.22 \frac{\lambda}{\alpha}$$

Where β represents the brightness of the electron beam, λ is the electron wavelength, α represents the convergence semi-angle of the electron beam, C_s stands for the spherical aberration coefficient, and I represent the beam current.

In Equation 4, another parameter can be calculated experimentally, and it is correlated to the diameter beam. This parameter is the brightness of the electron beam (β). The correlation is observed when the electron beam is focused on the specimen, the brightness increases, and when it is spread, it decreases. Therefore, it is essential to measure this parameter. Equation 5 shows the calculation of the brightness of the electron beam.

$$\text{Equation 5} \quad \beta = \frac{4i_e}{(\pi d_0 \alpha_0)}$$

Where d_0 represents the beam's initial diameter, i_e is the cathode emission current, and α_0 stands for the source's divergence semi-angle.

This section shows that considering the specimen's physicochemical properties and calculating parameters during the TEM acquisition is essential to understand and estimate the heat produced by the electron beam's interaction and the specimens. This information is valuable to avoid samples' damage or understand some physicochemical changes during the TEM analysis. [107], [108]

However, the estimation of some parameters could be difficult depending on the sample. This problem is due to the use of complex nanosystems or the difficulty of observing crucial parameters during *in-situ* characterizations. Figure 1.10 shows an approximation of the temperature change (ΔT) considering thermal conductivity values and the primary beam current from different electron beam sources. From this information, it is possible to observe the difference in ΔT through different materials such as conductors, semiconductors, and insulators. This estimation helps to estimate the ΔT in a faster way.

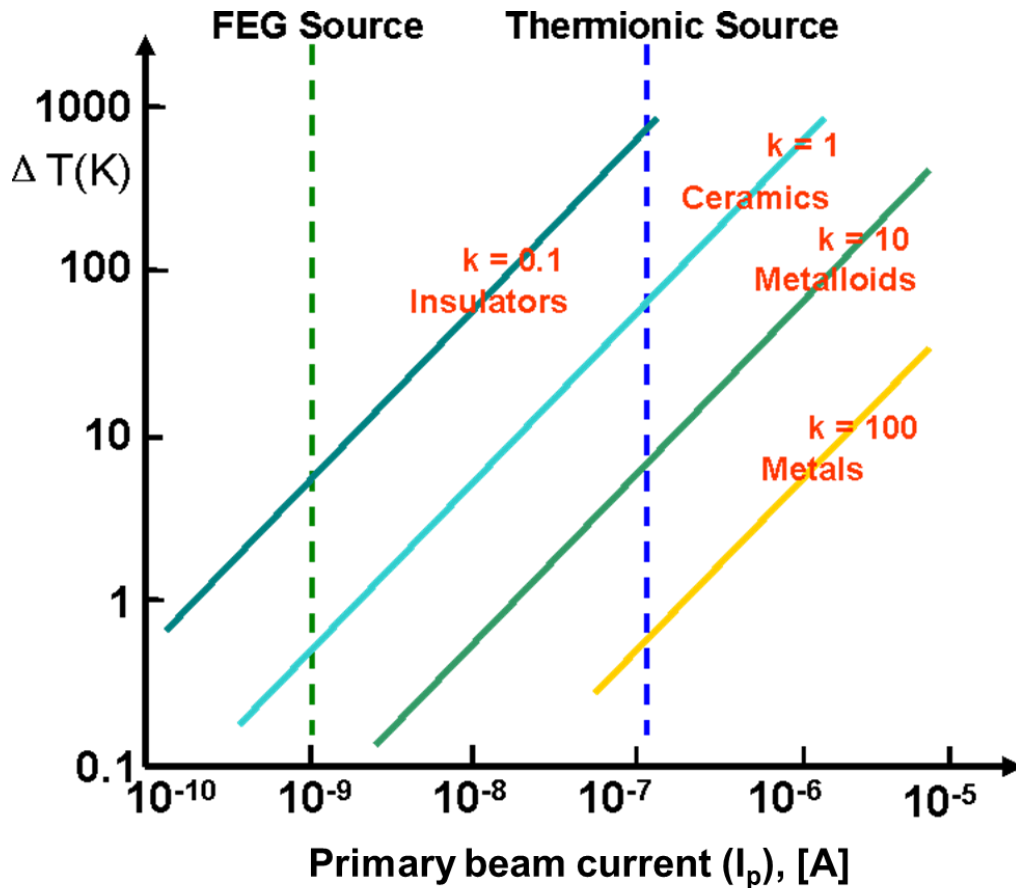


Figure 1.10 The increase of temperature (ΔT) through different electron beam currents and thermal conductivity values (k) of different specimens. The dotted lines show the different and most common electron sources that are found in TEM. Image used from Yougui, L “Heat generation/temperature increase by electron irradiation.” <https://www.globalsino.com> (2021). [104]

1.4.3 Importance of e-beam heating

The importance of the e-beam on the data acquisition in electron microscopy relies on the changes that may occur in the specimen. Specifically, the heat generated due to the high e-beam energy in TEM [109] is critical for studying nanoparticles' structural stability or chemical composition [89, 90].

The e-beam heating in electron microscopy has been used for thermal observations, which has been used in new devices based on vanadium dioxide [82, 91], thermal conductances of nanoparticles [113], and two-dimension (2D) materials [114]. However,

in these studies, the heating generated from the e-beam was only for increasing the temperature and observe interaction with the specimen (e.g., phase transition), and studies regarding the quantification of temperature were not done.

Another application where e-beam heating is important is the Debye-Waller effect (DW) for thermal measurements. Here, irradiative energy (most used is laser) increases the nanoparticle's heat by phonon vibrations. In DW studies, the energy contribution (based on temperature) from the e-beam is neglected, and the studies assume that the specimen is at room temperature when it is irradiated by an e-beam and is only considered the heat contribution from the laser irradiation [115].

Hence, the importance of e-beam on the electron microscopy studies is determinant for thermal studies and structural changes, chemical compositions, or measurements where heat may affect. This work will use the heating generated by the e-beam in TEM experiments to activate cargo release from single hollow-MNPs. This work will study the effect of sub-particle features and substrate effect on the rate and amount of delivery. These experiments will also help map and elucidate the spatial distribution of heat through cargo delivery.

1.5 Scope of the study

In this work, I will synthesize two sets of hollow-MNPs. I will study and compare the sub-particle morphologies using two different Ag cube templates (referred to as small and large templates henceforth). *Via* the galvanic replacement reaction, I will observe the structural changes in these hollow-MNPs. I will correlate these sub-particle features (pinholes and voids) with the particle solutions' optical absorption spectra. I will present results from scanning electron microscopy (SEM), UV-vis-IR spectroscopy, analytical software tools, and electrodynamic simulations to discuss the relationship between the structure and optical properties hollow-MNPs. This research will help us engineer the type of sub-particle feature we want to use for future applications.

I will also load a dye (simulating a drug) into the hollow-MNPs for both templates using a phase change material (PCM). I will study the cargo delivery of hollow-MNPs by indirectly heating the nanoparticle with an e-beam (TEM). This characterization technique will allow

me to analyze single particles while they are being irradiated. *Via* transmission electron microscopy imaging TEM, and EELS, I will elucidate and correlate the sub-particle morphologies' effect on cargo release. To the extent of our knowledge, these studies have not been performed before for single nanoparticles.

1.5.1 Hypothesis

The change in the Ag template's size will unlock different sub-particle morphologies formation mechanisms in the hollow-MNPs. These hollow-MNPs will have different optical properties, which are correlated to their sub-particle morphologies. The difference between these features for the small and large templates will provide different release mechanisms for cargo delivery studies.

2 LITERATURE REVIEW

Hollow-MNPs have been extensively studied towards applications in different fields such as catalysis, plasmonic, and nanomedicine. [95–97] Their advantageous feature is that their LSPR can be tuned depending on the size, shape, morphology, and composition [119]. *Via* controlled synthesis, it is possible to control the physical and chemical properties of hollow-MNPs and engineer the specific nanoparticle that can be useful depending on the application. However, controlling their structural features (e.g., size, void, or pinholes) is challenging.

This chapter will focus on the synthesis and structural studies of hollow-MNPs based on the GRR of Ag and Au and compare different morphologies that can be obtained with this reaction. The use of cubic hollow-MNPs in cargo delivery applications and the characterizations used to analyze those results will be discussed further in this chapter.

2.1 Synthesis and structural studies of hollow-MNPs

GRR has been the most widely used method for synthesizing hollow-MNPs. Due to this chemical reaction's versatility, the synthesis of a variety of bimetallic nanostructures is possible. The nanoparticles possess additional versatility in their structures by changing a few parameters (e.g., the composition of reactants, temperature, and time) [38, 99].

The chemical requirement using GRR is based on reactants that possess a different potential of oxidation and reduction. The reactant with a higher reduction potential is called a "sacrificial template"; commonly, these templates are solid metal nanoparticles (MNPs). The analyte, which has a higher oxidation potential, is an anionic metallic-halogenated solution based on ionic metals such as Au, Pd, or Pt [121].

As mentioned in 1.2.2, Galvanic replacement reaction of the Ag-Au system follows five general steps:

- i) Initiation of Ag dissolution during the Au³⁺ deposition
- ii) Formation of a pinhole and uniform wall thicknesses of Au–Ag alloy
- iii) Corners truncation
- iv) Generation of pores in the wall through a dealloying process

v) Generation of pores in the truncated corners

However, these steps can be modified if the parameters of the GRR change. The parameters could be the silver template's morphology, the chemicals used in the reaction, or reaction time. Figure 2.1 shows a general representation of the galvanic replacement reaction to produce hollow-MNPs.

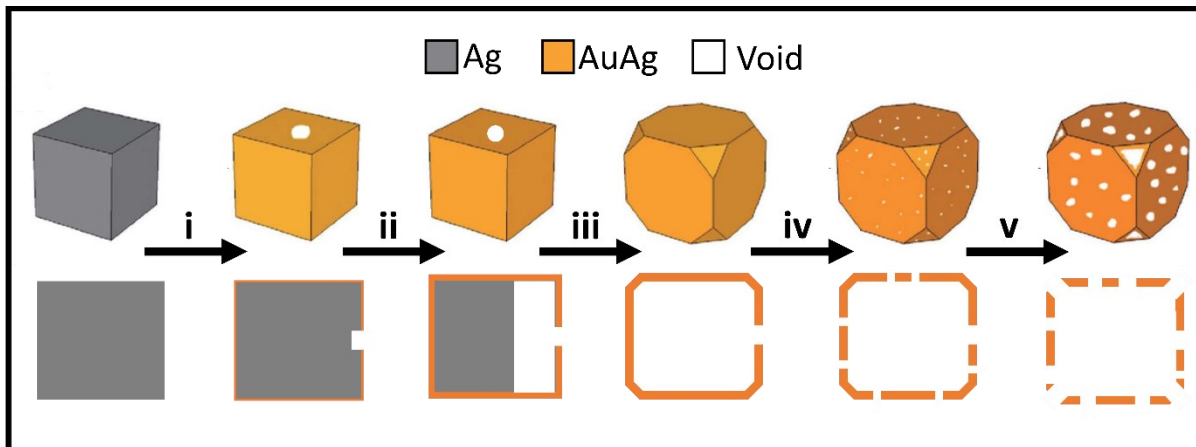


Figure 2.1 Schematic detailing of the major steps that galvanic replacement reaction follows. Pinhole formation and Ag dissolution (i), the formation of Ag-Au walls and void size increment (ii), the formation of the truncated walls and full void size development (iii), the dissolution of alloyed Ag atoms, and formation of pores (iv) and the formation of the pores in the truncated corners and diameter increment for small pores (v). Adapted from “Galvanic replacement reaction: A simple and powerful route to hollow and porous metal nanostructures” by X. Lu, J. Chen, and S. Skrabalak, 2007, *Journal of Nanoengineering and Nanosystems*, 221(1), Copyright (2009) by Sage publications. [122]

In early 2000, Xia et al. were the first to use the GRR to obtain noble metal-based hollow-MNPs [51, 102, 103]. The hollow-MNPs, synthesized by the GRR, are characterized by having bimetallic and thin walls. However, there is difficulty elucidating these nanostructures' composition and structural details, particularly at the single-particle level [125].

Characterizing and elucidating mechanisms of the chemical and physical behavior of hollow-MNPs contributes to improving our understanding of the synthesis of these

nanomaterials by GRR and thus allowing us to achieve and produce different materials with desired features.

Generally, hollow structures can exist in different morphologies fabricated through GRR. Silver nanoparticles have been chosen as the model for a sacrificial template for synthesizing hollow-MNPs. The easiness of producing silver nanoparticles and their versatility in changing their morphology [105–108] are among the principal properties that make them suitable to synthesize different hollow nanostructured materials. They can be produced in the form of spheres [130], rods [131], plates [132], and cubes [133], among many. However, the nanostructures of spheres, plates, and cubes have been the most widely used in GRRs [103, 113, 114]. Table 1 shows the representative morphologies in which Ag nanoparticles have been used for the sacrificial template.

In order to improve the optical and structural properties, as well as the properties of hollow-MNPs, template-based morphology control has been achieved to obtain hollow nanostructures of various shapes. The sacrificial template method plays a vital role because it sets the optical properties of hollow nanoparticles. For instance, Ag nanocubes and Ag nanoplates both have different LSPR. By controlling experimental parameters, the LSPR for nanocubes can be tuned in 400-500 nm [114], while nanoplates can be between 500-1200 nm [136]. If these structures are used as sacrificial templates in galvanic replacement reaction, the LSPR of the hollowed structure can be tuned depending on the application. The corresponding LSPR for the hollowed nanoplate can be tuned in a broader range than hollow nanocubes in this fashion.

However, in drug delivery applications, the optical property is not the essential parameter to be considered; biocompatibility, stability, and cargo loading capacity [116, 117] are among the principal parameters hollow-MNPs have to meet to be used in drug delivery.

Since the first report of the synthesis of hollow-MNPs [124], researchers have prepared hollow nanostructures by using Ag nanospheres [118, 119]. With the use of Ag nanospheres in the GRR, spherical hollow-MNPs can be obtained easily.

Ag nanospheres possess a similar LSPR to Ag nanocubes. This similarity means that the optical properties of spherical-shaped hollow-MNP are closely related to cube-shaped hollow-MNP (e.g., LSPR wavelength, size, and morphology dependence). However,

hollowed spheres have a disadvantage in the structural behavior; there is no control on the sub-particle morphologies. This disadvantage represents an important parameter to consider. Also, the final, individual hollow nanoparticle's structural changes will not represent the ensemble. It represents a challenge in terms of the elucidation for drug delivery mechanisms, increasing, for example, the standard deviation of the drug delivered, among others.

Other types of structures obtained *via* GRRs using Ag and Au are the nanoframes. This structure includes three-dimensional 3D skeletal nanostructures (e.g., nanocubes) and planar, 2D nanostructures. Hollow 2D nanostructures are specific nanostructures that are only obtained from specific AgNPs. The most commonly used template for 2D nanoframes is the nanoplates [114, 120].

Due to their open-like structure, nanoframes are easy to use in loading drugs. However, the open structure represents a limitation; drugs cannot be contained in such structures. Thus, drugs used in this kind of nanostructures need to have a chemical interaction with the metallic structure. Thiolate cargoes are the most common compounds used in drug delivery for nanoframes.

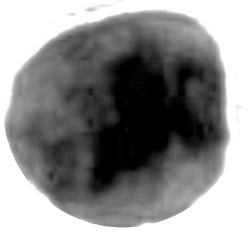
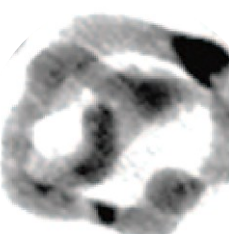
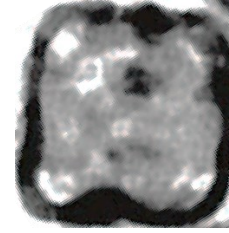
Compared with 3D nanoframes and spherical and cubic hollow-MNPs, 2D-based nanoframes cannot contain much drug-volume in their structure; this represents a problem in drug delivery applications. 2D-based nanoframes are limited to drugs that can interact chemically with their structures to be contained in these nanoparticles' spatial volume. On the other hand, the low content of metallic Ag in 3D nanoframes provides low cytotoxicity derived from the residual Ag after the GRR, and the production of oxygen-species is minimized. Thus, nanoframes are more suitable for biomedical applications, such as sensing and imaging [142]. Table 1 summarizes the disadvantages of hollow-MNPs in spheres and frames that they could have either in structural details as in drug delivery application.

As discussed above, hollow-MNPs possess disadvantages and advantages in their structural behavior. Cubic hollow-MNPs are porous structures with compact sizes obtained through the GRR based on Ag and Au materials, and they can be precisely engineered by controlling their plasmonic properties and surface chemistry. These

nanostructures' solid-state properties represent an advantage compared to the rest of the hollow structures, such as the spheres and frames. For instance, the templates of Ag nanocubes possess specific active planes. These sites lead to structural changes during the galvanic replacement reaction, which Ag nanospheres do not possess. This advantage that Ag nanocubes have is crucial because it allows researchers to engineer the nanoparticle to have the desired optical property, size, and sub-particle morphologies.

In conclusion, hollow-MNPs in cubic morphology are the most suitable structures for drug delivery applications due to their advantages in morphology and structure formation. However, structural details for these nanostructures have to be studied to maximize the success in biomedical applications.

Table 1 Comparison and development of the representative Ag templates and their hollow-MNPs counterparts. nanoplate [135] nanosphere [134] nanocube and nanorod [124].

Ag template	Hollow-MNP	Properties and applications in drug delivery
		Nanospheres. The advantages of using these templates are the facile synthesis of the template and their hollow-MNP. However, the non-controlled sub-particle features represent a challenge in engineering these nanoparticles for drug delivery.
		Nanoplates. Their LSPR can be tuned in NIR, being optimal for biomedical applications. However, the low volume for loading cargo makes them non-suitable for drug delivery purposes.
		Nanoframes. These nanoparticles can be produced efficiently, and they possess an LSPR located in NIR. However, their stability and their limited use with bonded-based cargo represent a low efficiency compared to their counterparts.
		Nanorods. They possess optical absorptions in NIR. However, their non-controllable sub-particle features and their low volume for cargo are their main disadvantages.
		Nanocubes. These nanoparticles have a controllable synthesis with LSPR located in the biological window. Their versatility of loading different cargos, high stability, and their controlled sub-particles morphologies are their main advantages.

2.2 Structural studies of cubic hollow-MNPs

Structural studies in hollow-MNPs in the form of spheres are lacking. The sacrificial templates in the form of spheres do not possess different mechanisms or applications that may change sub-particle morphologies. For instance, Ag spheres can only be modified by varying their physical size; consequently, mechanisms for sub-particle changes such as pinholes and voids will be the same. From now on, this thesis will refer to the hollow-MNPs as nanoparticles with cubic morphology.

The non-control of the sub-particle features represents a challenge if these nanostructures are used in drug delivery. The options to modify their structure are limited, limiting the optimal performance for drug absorption or delivery. However, Skrabalak et al. [48, 49, 122, 123] have studied the mechanisms involved in the production of cubic hollow-MNPs. *Via* SEM and TEM analyses, Skrabalak et al. found that Ag nanocubes' initial morphology leads to different mechanisms for structural modification to produce hollow-MNPs.

They demonstrated the control over the sub-particle morphologies producing hollow-MNPs with pores explicitly localized at the corners. They achieved it using rounded Ag nanocubes as a template (Figure 2.2B) in the GRR. This template's synthesis is similar to sharp Ag nanocubes using the polyol method, and they can be obtained by modifying reaction time [120]. These changes are different from using an Ag template with sharp corners. In this latter case, the pinhole formation is essential to start the oxidation of Ag atoms from the template. If the oxidizing agent's addition continues, the corners are modified, and the pinhole diameter increases. We can infer that Ag templates have a major role in generating sub-particle morphologies in GRR from these observations.

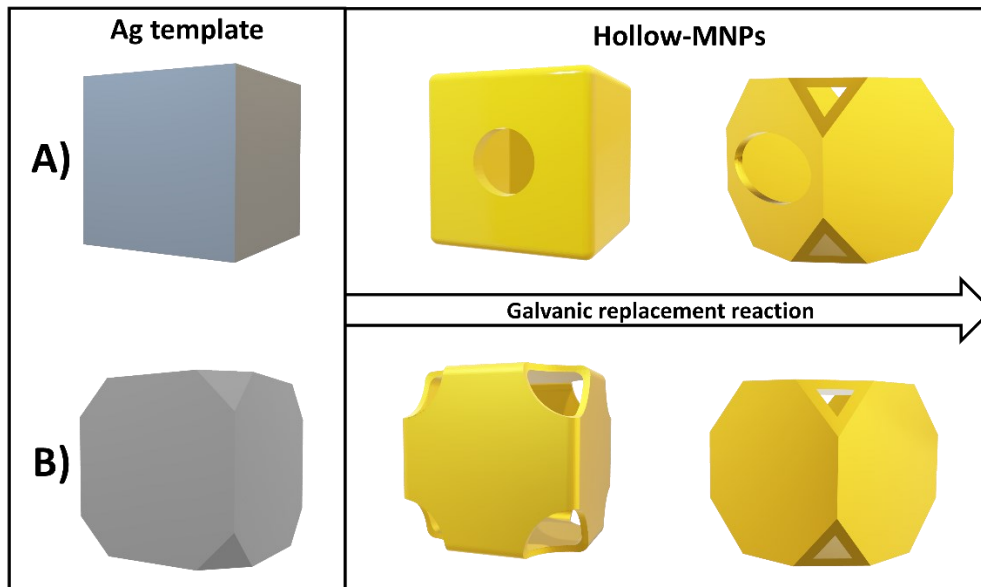


Figure 2.2 Schematic representation of the different sub-particle morphologies of cubic hollow-MNPs by changing the Ag template from A) sharp corners and B) rounded corners.

Different sub-particle morphologies can also be achieved by modifying the synthesis method. In 2016, Genç et al. [125] reported in the literature the optical tuning of the LSPR from ultraviolet to near-infrared by using the galvanic replacement reaction employing solid Ag nanocubes as a sacrificial template, which were transformed into hollow-MNPs until finally, cubic nanoframes. They modified the synthesis method by applying cetyl trimethyl ammonium bromide (CTAB) and ascorbic acid as surfactants instead of PVP during the GRR. Due to this change, different step structures were obtained, and also the obtention of a stable cubic nanoframe was possible. Figure 2.3 compares the structural changes during the original procedure's galvanic replacement reaction versus the modified version.

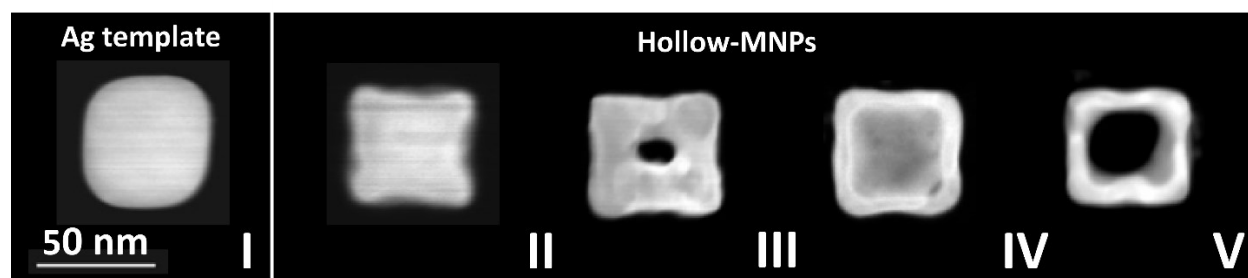


Figure 2.3 Sub-particle morphologies observed by Genç et al. [125]. I) Silver template, II) Beginning of the galvanic replacement reaction, III) Pinhole nanocube formation (in the front and back facets), IV) single-walled and full void development and V) Nanoframe formation. Changes were observed by increasing the concentration of HAuCl_4 .

Via single-particle EELS analysis, the authors characterized each structure's plasmonic resonances found for every batch synthesized *via* GRR. It is unclear if the single-particle analyses are characteristic for each batch. They do not mention any statistical analysis that may support those structures' obtention in the majority in all the batches. For instance, the structure observed in Figure 2.3III corresponds to a pinhole that goes through the front and back facets, and it is physically impossible for this structure to evolve into the structure shown in Figure 2.3IV that possesses complete walls with small pores.

Even though they did not perform any statistical analysis, they compared the optical spectra with simulations using the boundary element method (BEM). They could correlate that the EELS spectra from experiments are similar to their counterpart by performing these simulations. However, these analyses are still for single-nanoparticles and not for the ensemble (batch). The only possible explanation for the step structures' obtention in Figure 2.3 could be that the synthetic procedure modifications made by Genç et al. affected the structural mechanisms of formation for these nanostructures.

From this work, we can learn useful information. First, changing the GRR can induce changes in the structural morphology of hollow-MNPs. Second, the simulation of these nanostructures' optical properties can help us elucidate or, at least, correlate the mechanisms involved during the GRR.

All the observations from Skrabalak *et al.* and Genç *et al.* were made based on the use of different shapes of Ag templates or varying parameters in the GRR. Nevertheless, studies observing the changes that may occur by using different Ag templates' sizes were not addressed before, and this is because the synthesis of Ag templates smaller than 30 nm is difficult [144]. Nonetheless, for drug delivery applications, the volume in which the drug can be loaded is essential, as well as having a plasmonic absorption in biological windows.

We think that the structural behavior of hollow-MNPs for drug delivery applications can be made by using larger sizes of Ag templates, not smaller, as Skrabalak *et al.* focused on before.

In summary, structural changes such as in the whole nanoparticle, as in sub-particle morphologies, could be achieved by modifying the GRR or silver templates' morphology parameters. However, to have a direct comparison and the possibility to monitor the reaction to control these steps, the GRR must be followed without changes. The effect of template size on the sub-particle morphologies was not studied. Hence, developing a method to study and explain the mechanisms involved by performing this change is essential.

2.3 Hollow-MNPs as cargo delivery actuators

Shin *et al.* [145] found that hollow-MNPs synthesized by GRR based on AuAg materials possess pores around ≈ 3.4 nm measured *via* nitrogen adsorption. These pores are large enough for drugs such as oligonucleotides or doxorubicin (commonly used in drug delivery), which can be loaded and delivered successfully [145].

However, the cargo has to be contained before the delivery. Liquid solutions cannot be kept inside hollow-MNPs. That is why different methods were developed in which the use of smart polymers [125–127] and phase change materials (PCMs) [128, 129] solved this issue. Due to their stability and biocompatibility, and secure handling, PCMs materials have been used in the last decade to perform drug delivery using hollow-MNPs.

PCMs change their physical characteristics when absorbing heat. The material phase varies with temperature, and depending on the temperature range, PCM materials can

melt or solidify. Depending on the application, PCMs can be chosen based on their melting point temperature. In drug delivery, this temperature must be close to the body's average temperature to avoid damages during the heat to release the drug. Figure 2.4 shows a schematic representation of the procedure for loading PCMs into the gold nanocages.

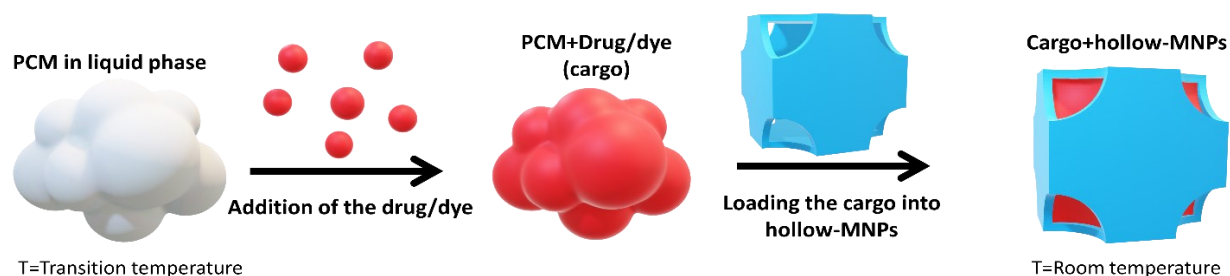


Figure 2.4 Schematic representation of the steps involving *loading* the cargo into the hollow-MNPs *via* the PCM method. First, the PCM material is melted and mixed with the drug/dye (cargo). Then hollow-MNPs are added, and it allows the incorporation of the cargo. The cargo+hollow-MNPs are extracted with water due to the polarity difference.

In 2011, Moon et al. [149] reported a new theranostic system for imaging *via* contrast of photoacoustic and controlled drug delivery using PCM. They filled the void of hollow-MNPs with 1-tetradecanol (PCM) combined with a dye to perform this work. The dye simulates a drug's presence and is used to detect the cargo's presence (PCM and dye) in the system. For instance, to probe if the load inside an hollow-MNP was successful, observe the dye's UV-vis-NIR absorption after the loading procedure.

In their work, they used high-intensity focused ultrasound (HIFU) to stimulate the drug release. By varying the power of HIFU, they could observe different release patterns, at higher power, the release increases. Importantly, inductive heating takes longer times of release compared to HIFU. These findings are explained by the fact that ultrasonication stimulates local heating on the nanoparticle, being transferred directly to the PCM/drug system.

However, the hollow-MNPs used in the study mentioned above were synthesized only with a full void structure with small pores on their surface; the release mechanism is still unclear. The bright-field images for hollow nanoparticles are shown in Figure 2.5. It is

essential to characterize different hollow-MNPs to elucidate these mechanisms. Besides, the use of HIFU *in vivo* for drug release is difficult. It is necessary to use a non-invasive technique only in local places.

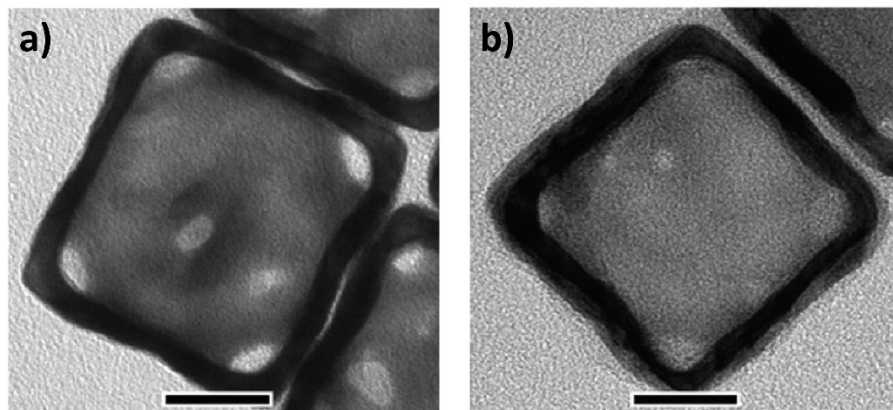


Figure 2.5 Bright-field TEM images for the hollow-MNPs synthesized by Moon *et al.* [149] before (a) and after (b) the cargo loading process. The scale bar is 20 nm. Adapted from “A New Theranostic System Based on Gold Nanocages and Phase-Change Materials with Unique Features for Photoacoustic Imaging and Controlled Release” by G. Moon *et al.*, 2011, *Journal of the American Chemical Society*, 133, Copyright (2011) by ACS publications.

Similarly, Tian *et al.* [150] reported the effect of temperature and laser irradiation on drug/dye release. The effect of temperature is based on the maximum release compared to room temperature; Tian *et al.* found a maximum temperature of the cargo release of 42°C and Moon *et al.* at 40°C. First, none of them reported the method to follow to find the maximum temperature of release. The cargo release temperature is based on the supposition that the PCM will have a phase change at ~39°C. However, structural features on the particle can affect the release independently of the phase change temperature. Here, we can conclude that a study of this effect is lacking.

Tian *et al.* reported the laser's effect on drug release *in vitro* experiments, showing that the signal in Raman scattering decreases by increasing the exposure time to the laser. This phenomenon is explained by the photothermal interaction between hollow-MNPs and the laser. However, they could not calculate the system's temperature, which cannot allow a direct correlation between the drug release and temperature.

Many methods have been reported for drug release purposes using energy irradiation [130–133]. However, none of them explains the mechanisms of release and their correlation with the optical and structural properties of hollow-MNPs.

The lack of information about the mechanisms involved in drug release is due to the characterization techniques. Many experiments are based only on the effect of diverse parameters on the ensemble of nanoparticles. The analysis of single particles is the only way to provide the exact information of these mechanisms depending on their structure. This information can be extrapolated to the structures with the same morphology and sub-particle features. That is why it is necessary to use a technique that can involve, at the same time, the detection method with the parameter that triggers the drug release.

2.4 Imaging techniques for cargo delivery applications

Therefore, imaging techniques that offer an assessment of single nanoparticle drug delivery are of great importance. Many of these techniques play a key role in the preclinical evaluation of drug delivery nano-systems, allowing them to elucidate their mechanism of action and therapeutic effect. Even though there are many techniques for drug delivery characterization (e.g., molecular, optical, nuclear, and Raman imaging) [134–138], this section will discuss and review the current techniques used to characterize the mechanisms of drug delivery for inorganic nanocarriers at the nanoscale.

2.4.1 Atomic force microscopy

Atomic Force Microscopy (also called scanning force microscopy; AFM) uses the deflection of a fine tip, the cantilever. This microscopy technique enables investigating samples that are not necessarily conductive. When the tip is interacting with a surface, the cantilever is bending due to forces between the tip and the specimen, causing a proportional deflection to the force applied to the sample, which provides a visualization of the surface topography. [160]

AFM has been used to investigate drug-target interactions at the single-cell and single-molecule levels. This technique allows researchers to visualize the drug effects on live cells, which are inaccessible by traditional characterization techniques. This technique

also allows measuring the size and many other physical parameters for drug DVs in a single analysis. [161] However, this technique has been used to obtain only physical information of the drug nanocarriers [141–143], and it has a common problem for drug delivery characterization, which is the long scanning time required for analyzing the delivery *in-situ* or *in-vivo*, knowing that the initial delivery is rapid. This technique is not suitable for characterizing the release mechanisms at the nanoscale for any drug delivery actuators due that the time of delivery is faster than the acquisition time from this characterization technique.

2.4.2 Electron microscopy

The broad range of electron microscopy techniques (imaging techniques, analytical spectroscopies, tomography, gas or liquid in situ experiments...) currently provides the means to reveal at the finest spatial scale, down to sub-Angstrom, the 2D and 3D information required to monitor the structure and functionalization of the nanometric systems as well as to rationalize their behavior. Inorganic nanoparticles, especially those with a porous or hollow nature, have emerged as powerful materials for drug delivery applications. One relevant characteristic of these materials is their high loading capacity, with high volumes inside the structure in which the drug can be stored.

Many inorganic carriers such as mesoporous silica nanoparticles, metal-organic nanoparticles [67-69], and carbon nanoparticles [144, 145] have been analyzed through electron microscopy [146, 147]. Due to its advantages compared with conventional techniques and the possibility of analyzing nano-systems with different *in-situ* techniques (e.g., EELS, EDS, etc.), electron microscopy has been successfully used to observe these inorganic nanocarriers interacting with living systems. Although TEM imaging techniques could be employed to image nanocarriers inside cells [148, 149], the sample preparation is problematic due to the complicated treatment processes that can induce modifications in the cells and nanocarriers, preventing the use of TEM in these analyzes. Also, the higher energies of TEM's e-beam can damage the sample due to its organic composition. The use of cryo-TEM has limitations in analyzing systems that need heat as a primary stimulus for drug delivery.

The issues related to preparation, treatment processes, and specimen damage due to the e-beam can be avoided using another electron microscopy technique, scanning electron microscopy (SEM). In this microscopy technique, the morphological and compositional (through EDS) information is obtained using specific emitted electrons. The electrons used for the morphological information are the secondary electrons (with energies smaller than 50 eV) and, for the composition analysis, the backscattered electrons (with energies larger than 50 eV). Also, the low energy use in the e-beam (which could be less than 30 keV) prevents biological specimens' damage. Electron microscopy has mainly been used to determine the cellular interaction between nanocarriers and cells *in-vitro* [150–152], and it is limited to evaluate nanoparticle distribution on the biological entities or only for their morphological studies.

Nowadays, no study is associated with inorganic-based-nanocarriers' drug release in real-time with a high spatial resolution. The closed system of electron microscopy analysis makes it hard to introduce the stimulus for *in vivo* and *in vitro* analyzes.

2.5 Thermal studies of e-beam interactions

In-situ electron microscopy experiments are essential to observe the mechanisms at the nanoscale. However, the electron beam may significantly impact specimens' stability, increasing the difficulty of interpreting the results obtained through *in-situ* observations.

One of the complications it may induce is the transformation of the morphology of nanoparticles. Albrecht *et al.* [174] studied the thermal stability of CTAB-stabilized gold nanorods heated resistively to 400°C and irradiated under the e-beam in an environmental-TEM and compared these results with *ex-situ* heating experiments. Under inert conditions, the gold nanorods were stable when exposed to the e-beam, but in contrast, the nanorods reshaped at temperatures lower than 100°C in *ex-situ* heating experiments. They hypothesized that CTAB is transformed into a carbon layer under e-beam irradiation. This layer prevents the nanorods from deforming. When the nanorods in the *in-situ* experiments are exposed to an oxidizing environment, the carbon layer is removed. It allows the diffusion of the gold atoms in the gold nanorod, tending to form nanospheres.

This work emphasizes the importance of understanding mechanisms taking place under e-beam irradiation. However, the resistive heating they used in *in-situ* experiments does not allow observing the direct effect of the e-beam on the nanosystem. The combination of both heating sources causes the formation of the carbon layer that protects the gold nanorods from deformation. Besides, CTAB degrades at a maximum temperature of 340°C [175]. The carbon layer transformation of CTAB that Albrecht *et al.* observed might be related to the transformation of CTAB into smaller species, being initiated by the resistive heating they used.

Measuring the real temperature of the specimen due to the irradiation of the e-beam in TEM is difficult. The beam will interact with different materials (e.g., insulators, conductive materials, etc.), which will vary the temperature for the specific area being analyzed. In 2012, Huang *et al.* [112] observed through selected area diffraction a phase transition process from VO₂(B) to VO₂(M1) under electron beam irradiation. Although this transition's exact temperature was not determined, the absence of the VO₂(R) phase, which is a phase formation of VO₂ at 68°C, indicates that the specimen temperature is in the gap between room temperature and 68°C. In 2014, Guo *et al.* [96] used a similar approach. They prepared a micro thermometer based on a vanadium dioxide nanowire measuring the specimen's temperature and flow rate. Using the mechanism from Huang *et al.*, the metal-insulator transition of VO₂ (VO₂(M1) to VO₂(R)) at 68 °C provides a change of properties of VO₂ when it is exposed to the e- beam. However, this phase transition is contradictory to what Huang *et al.* observed. This contradiction is a problem that will affect all the experiments when they are compared. The TEM experiment conditions must be equal to compare different systems, such as time of analysis, e-beam energy, and the substrate. Hence, the development of a new approach is essential. A material that will behave similarly in different TEM experiments where its physical properties can be controllable is desirable. This material will aid in detecting the temperature rise when the specimen is exposed to the e-beam.

3 MATERIALS AND METHODS

3.1 Synthesis of silver nanocubes (AgNCs)

The synthesis of AgNCs was performed using the protocol from Skrabalak *et al.* [120]. The Ag nanocubes were prepared by the sulfide-mediated polyol method, in which Ag^+ was reduced to Ag^0 by ethylene glycol in the presence of PVP and Na_2S . However, this protocol is designed just to synthesize nanoparticles with an average size of 45 nm. To obtain different sizes, I modified this protocol by changing the concentration of Ag^+ . In a glass container (vial 20 mL), which was heated at 150°C using silicon oil, a magnetic stirrer was placed, and the speed was set at 260 rpm. Then, 6 mL of ethylene glycol and 70 μL $\text{Na}_2\text{S}\cdot 9\text{H}_2\text{O}$ 3 mM were added to the vial, and the solution was left for 10 min to reach the target temperature and avoid the condensation of H_2O . After 10 min, 1.5 mL of PVP 8 M (55,000 molecular weight) and 0.5 mL of Ag^+ 280 mM were added quickly (the final concentration of Ag^+ was 17.30 mM), and the vial was covered again. The solution was left for 15 min, after which the color of the solution changed from colorless to green ochre.

The solution was transferred to a 50 mL conical tube, and it was centrifuged at 2000 g for 30 min. The supernatant was then removed, and 1.5 mL of distilled water was added to the conical tube, followed by sonication for 1 min. This solution was placed in a 1.5 mL Eppendorf tube, and it was centrifuged at 9000 g for 10 min. The supernatant was removed again, and 1.5 mL of distilled water was added, repeating the process twice. Once the pellet was isolated, this was resuspended with 1.5 mL of distilled water and sonicated for 1 min; then, it was placed in a vial containing 2.5 mL of distilled water. The solution was stored at 4°C . This process was used to obtain the small template of AgNCs to achieve larger sizes of AgNCs; I used the same methodology. However, volumes were modified with 2.865 mL of ethylene glycol, 225 μL $\text{Na}_2\text{S}\cdot 9\text{H}_2\text{O}$, 3.75 mL PVP, and 1.25 mL Ag^+ .

3.2 Synthesis of hollow-MNPs

Hollow-MNPs were synthesized by using the AgNCs. First, 5 mL of PVP 0.001% and a magnetic stirrer were placed in a round-bottom flask. After that, 200 μL of AgNCs for the small template and 100 μL for the large template (previously sonicated for 30 secs) were added into the flask, and the solution was heated until a mild boil condition. Once the water vapor was condensed in the flask, the solution was left for 10 min under continuous stirring. Then, by using a syringe pump, HAuCl_4 0.1 mM was added (with a speed of 0.75 mL per minute), and the solution was refluxed for 10 min. The HAuCl_4 volumes were 4.01, 4.75, 5.75, 7.00, and 8.50 mL for the small template; volumes were 3.00, 4.00, 5.50, 7.00, and 8.50 mL for the large template. After the galvanic replacement process, the solution was centrifuged once at 2000 g for 30 min. The supernatant was removed, and the pellet was re-dispersed in 4 mL of distilled water and stored in a glass vial at 4°C.

3.2.1 Characterization of hollow-MNPs

All the samples of AgNCs and hollow-MNPs were characterized by using UV-Vis-NIR Perkin Elmer Lambda 750 equipment with a scanning wavelength from 300 to 1100 nm. Distilled water was used as a reference.

The structural and statistical analyses for small and large hollow-MNPs were carried out using an SEM Tescan LYRA 3 equipment. Samples (for both, AgNCs and hollow-MNPs) were prepared by re-dispersing 40 μL of the AgNCs/Hollow-MNPs solution in 120 μL of distilled water. Then, 20 μL of the re-dispersed solution was placed on a Si wafer substrate, which was previously washed and cleaned. The complete SEM and high-angle annular dark-field imaging (HAADF) with the scanning transmission electron microscopy (STEM) characterizations of hollow-MNPs can be observed in Appendix I. Image analysis was performed using a Matlab code, which extracts dimensional parameters from particles in the samples. The histograms of wall thickness and total particle sizes are available in Appendix II. A group of 100 nanoparticles was analyzed in each sample.

3.3 Electrodynamic simulation

The computational simulations were performed in a classical electrodynamic framework, solving the Maxwell equations within a finite element method (FEM), as implemented in the commercial software package COMSOL. I have modeled the nanoparticles' key material and geometrical characteristics and calculated their optical response under linearly polarized plane-wave excitation. Given that I am considering colloidal nanoparticles, all the theoretical extinction cross-sections reported in this manuscript were obtained by averaging both orthogonal polarizations for light propagating along each of the three main symmetry axes of the cube, for a total of six illumination conditions (reduced as appropriated by the specific symmetries of the nanoparticle). Besides the interaction cross-sections, some figures depict the surface charge at the inner and outer surfaces of the hollow-MNPs for relevant light incidences and polarizations to illustrate the spatial symmetry of specific plasmonic modes.

In all cases, I have considered the nanoparticles as immersed in water (refractive index of $n = 1.33$) since this is the solvent used in experimental optical characterizations. I have modeled their permittivity using data from the literature, taking the permittivity of pure Au and pure Ag. The alloys from an analytical model created from experimental data in Rioux *et al.* [176] The material composition of the different nanoparticles is divided into the core, an inner wall, and an outer wall to reproduce the two different effective diffusion models under discussion. The regions separated to differentiate alloy distribution through different permittivity data, i.e., inner and outer walls, are schematically described in the captions of Figure 4.9. The nanoparticles developed from the small Ag template have a dominant silver presence in the inner wall ($\text{Ag}_{90}\text{Au}_{10}$) and pure gold at the outer wall, consistent with an atomic diffusion-based on the nanoparticle's defect.

In the hollow-MNPs developed from the large Ag template, the first three models (in which the void extends until homogeneously covering the inner cube volume) are modeled with an inner wall composition of pure silver and an outer wall of $\text{Ag}_{10}\text{Au}_{90}$. Once the void is fully developed, the inner wall will consist of a silver alloy ($\text{Ag}_{70}\text{Au}_{30}$). The outer wall is invariably an alloy with gold's dominant presence, although the proportion of silver increases in the structures with pinholes (changing from $\text{Ag}_{10}\text{Au}_{90}$ to $\text{Ag}_{30}\text{Au}_{70}$).

However, to compare the effect of the different gradients of alloys on the optical properties of hollow-MNPs, I performed electrostatics simulations for small and large particles varying the concentration of the AgAu alloys for the inner wall (small particles) and the outer wall (large particles) considering the parameters from Table 2 and Table 3 for small and large hollow-MNPs, respectively.

Table 2 and Table 3 summarize the structural changes and the walls' compositions for every model used in the computational analyses in Figure 4.7 and Figure 4.9 for reproducing the experimental values. The additional datasets used to reproduce the strong-coupling regime between the particle and void plasmonic modes use fractions of the inner and outer wall thicknesses. At the same time, the remaining geometrical features remain unchanged.

Table 2 Parameters used in the theoretical calculations for a small template with an inner wall = 4 nm, outer wall = 3.5 nm, and a total size of 54 nm.

MODEL	STRUCTURAL CHANGES
1	Void size of 46.5x46.5x40 nm (WxDxH).
2	Full void size of 46.5 nm
3	Void size 47 nm with a pinhole of 5 nm in diameter
4	Void size 47 nm with a pinhole of 10 nm in diameter
5	Void size 47 nm with a pinhole of 10 nm and removal of 4 corners of the cube.
6	Void size 47 nm with a pinhole of 10 nm and removal of 8 corners of the cube.

Table 3 Parameters used in the theoretical calculations for the large template with an inner and outer wall = 5 nm and a total size of 74 nm.

MODEL	STRUCTURAL CHANGES
1	Void size of 65x65x20 nm (WxDxH).
2	Void size of 65x65x40 nm (WxDxH).
3	Full void size of 65 nm
4	Full void size and three random pinholes of 3 nm on each face of the cube
5	Full void size and nine random pinholes of 3 nm on each face of the cube

3.4 Synthesis of a modified large hollow-MNP

A new synthesis method was performed to have similar sub-particle features to small hollow-MNPs. A modified version of the methodology was performed using a large AgNCs template. Here, the volumes and quantities will be explained, and the detailed steps are the same as in section 3.1-Synthesis of silver nanocubes (AgNCs).

In a round-bottom flask of 50 mL, 5 mL of PVP 0.1% and a stirrer were placed. Then, 2 mL of large silver nanocubes (AgNCs) template were added to the flask. After, H_{AuCl₄} 10 mM was added, and the solution was refluxed for 10 min. The H_{AuCl₄} volumes were 8.5, 15, 22 mL. After the galvanic replacement process, the solution was centrifuged and washed three times at 2000 g for 30 min with distilled water. The supernatant was removed, and the pellet was re-dispersed in 4 mL of distilled water and stored in a glass vial at 4°C.

3.5 Cargo loading into hollow-MNP

The process for loading the cargo in the hollow-MNPs was used following the method from Moon *et al.* [149]. In my experiments, I use 1-tetradecanol as cargo. In a glass flask, 4 mL of the previously synthesized hollow-MNPs were centrifuged and re-dispersed in 4 mL of isopropyl alcohol. From this solution, 3 mL of the hollow particles were mixed with 5 mL of 1-tetradecanol at 70°C. After the evaporation of isopropanol (approx. 30 min), the hollow-MNPs were dispersed only in 1-tetradecanol. During the evaporation process,

some of the nanoparticles were stuck in the beaker's walls. In order to re-dispersed them, they were placed under ultrasonication for 1 min. Notice that the ultrasonication's water temperature must be above 40°C to avoid the solidification of 1-tetradecanol. Once the nanoparticles were re-dispersed, the beaker was placed in a sand-bath (previously heated to 100°C) for 8 hrs under mild stirring.

After the cargo loading, the sample was transferred to a previously heated (90°C) Eppendorf tube containing distilled water. It is important to have a higher temperature than 40°C to maintain the cargo in the liquid phase and to avoid solidification during the handling. Here, there will be a formation of two different phases due to the alcohol and water's polarity. Due to their densities' differences, the alcohol phase will be in the upper part, and the aqueous phase will be at the bottom of the tube.

Then, the tube was centrifuged at 4600 g for 5 min. During this process, the nanoparticles from the upper phase (1-tetradecanol) were transferred into the aqueous phase by centrifugal forces. This process was repeated until the majority of the 1-tetradecanol was removed. It is important to notice that 1-tetradecanol may solidify during the centrifugation process. To minimize this problem, water from the tube must be close to the boiling point, and centrifugation time could be decreased to make a faster separation. After the centrifugation, nanoparticles were dispersed in 1 mL of distilled water and stored at 4°C.

3.6 *In-situ* cargo delivery of hollow-MNPs

Once the hollow-MNPs were loaded with the cargo, they were placed onto a TEM grid. The nanoparticles' solution was diluted 1:1 with distilled water, then 20 uL of this solution was placed in a copper grid with silicon monoxide as a substrate with 15-30 nm of thickness. The solution was left to evaporate at room temperature.

Bright-field images of samples were collected with a TEM JEOL 2100Plus at 200 keV. The cargo release from the hollow-MNPs started immediately right after the contact with the e-beam. The release was captured in a frame every ~2.3 sec (from now on named stack) for 30 min using a slit of 20 eV for the GIF camera. The slit aids in increasing the contrast in the bright field image between the substrate and the cargo released.

The hollow-MNPs for small and large (modified) templates were categorized depending on their number of open corners. The analysis for every category was repeated from 4 to 8 times with different hollow-MNP to obtain statistical information. All the stacks were processed using a MATLAB software code, detailed described in 3.8 Data analysis of bright-field TEM images.

3.6.1 Substrate comparison for the cargo delivery

The large hollow-MNPs with three open corners were used to compare the effect of two substrates on the cargo release. These substrates were silicon monoxide (15-30 nm thick) and a single graphene layer. The particles were analyzed using bright-field imaging for 30 min and processed with the MATLAB code.

3.7 *Ex-situ* cargo delivery of hollow-MNPs

An experiment *ex-situ* was performed to observe if there was cargo inside the particles that did not show any release. The hollow-MNPs analyzed were the large ones with the half void, full void, and full void with pores. In a closed Eppendorf tube, 1 mL of every nanoparticles' solution was heated for 4 h at 80°C. Then, 20 μ L of this solution was diluted with 20 μ L of distilled water. A drop from this solution was placed in a TEM grid with silicon monoxide substrate and dried at room temperature. The nanoparticles were characterized *via* bright-field imaging following the same conditions as *in-situ* experiments, as shown in chapter 3.6 *In-situ* cargo delivery of hollow-MNPs.

3.8 Data analysis of bright-field TEM images

Imaging analysis was performed for every image in the stack. Every sub-particle morphology categorization (small and large with 1, 3, and 4 open corners) was analyzed using Matlab's code. Every stack of images was transformed into a black and white image with a specific threshold; this aids in selecting the darker areas from the images. The darker areas correspond to the organic material (cargo) and the hollow-MNP. Each stack is composed of ~800 images, which were analyzed individually. The areas were plotted depending on their sub-particle feature (open corners) from the initial release until 30 min.

3.8.1 Electron dose calculations

To obtain a value as a reference to reproduce the information with similar conditions, I calculated the electron dose (e-dose) from our Matlab code. In this calculation, we considered a small area of 200 nm² where electrons are not interacting with the particle or the cargo released, and typically the considered area is close to the corners of each analysis.

$$\text{Equation 6 } e - \text{dose} = \frac{e\text{-counts (per } A_{mes})}{A_{mes}}$$

Where e-counts represent the electron counts per considered area and A_{mes} is the area under consideration. The e-dose was calculated for every image in the stack and each image have 1 sec of acquisition time, and it is shown as the average for 30 min of analysis. It is important to note that this value approximates the real e-dose value due that I neglected the substrate's contribution. The substrate in these experiments covers all the areas where the cargo release is shown, and real values must be calculated in areas where there is no interaction e-beam with the specimen (areas in vacuum).

3.9 Surface detection of PVP on hollow-MNPs

Through STEM analysis, hollow-MNPs were analyzed to detect the presence of PVP. Specifically, the nanoparticles were imaged and analyzed using the HAADF detector and EELS using the core-loss energy range with 10 s of time collection. The EELS data collection was performed in a line scan, and the analysis was performed differently, depending on the hollow-MNPs. For small hollow-MNPs, the line scan was taken from one corner, considering the face, open corner, wall, and substrate. The large hollow-MNPs (non-modified) were analyzed considering the face and the pores on the structure. Large hollow-MNPs (modified) were analyzed from side to side, including the substrate (both sides), the face, and the pinholes on the structure.

The data processing for STEM-EELS characterization was performed with an automated code in Matlab using background subtraction with the power-law fitting model. The results were plotted according to their distance position from the line scan (y-axis) versus the energy signal (x-axis).

4 RESULTS AND DISCUSSION

4.1 Structural characterization

AgNCs have different structure changes during the galvanic replacement reaction to demonstrate the effects of structural changes on full nanocubes; the hollow-MNPs were first analyzed by SEM.

Figure 4.1 shows a low-magnification SEM image of the small (47 nm) AgNCs template and their respective transformation to hollow-MNPs. Since the secondary electrons were used to form the figure's images, the parts with high-mass thickness appear bright, which allows us to identify the full nanocubes and hollow-MNPs. Complete information on the SEM characterization and the HAADF-STEM characterization for every sample's representative nanoparticle is shown in Appendix I.

The measurement of the total sizes of the AgNCs and hollow-MNPs and the wall thickness of the hollow-MNPs were automated through a custom segmentation code (results in Appendix II and II). This code can analyze each particle separately: create intensity profiles along the two principal axes of the particles (

Figure 4.1c) and fit these intensity profiles with square functions convolved with the microscope's point spread function (Figure 4.1d).

In this fashion, I obtained accurate structural measurements for hundreds of particles at once for further statistical analysis. For each batch I synthesized (12 in total: 6 different H_{Au}Cl₄ concentrations for each small and large template), the histograms of wall thickness and total particle sizes are presented in Appendix II.

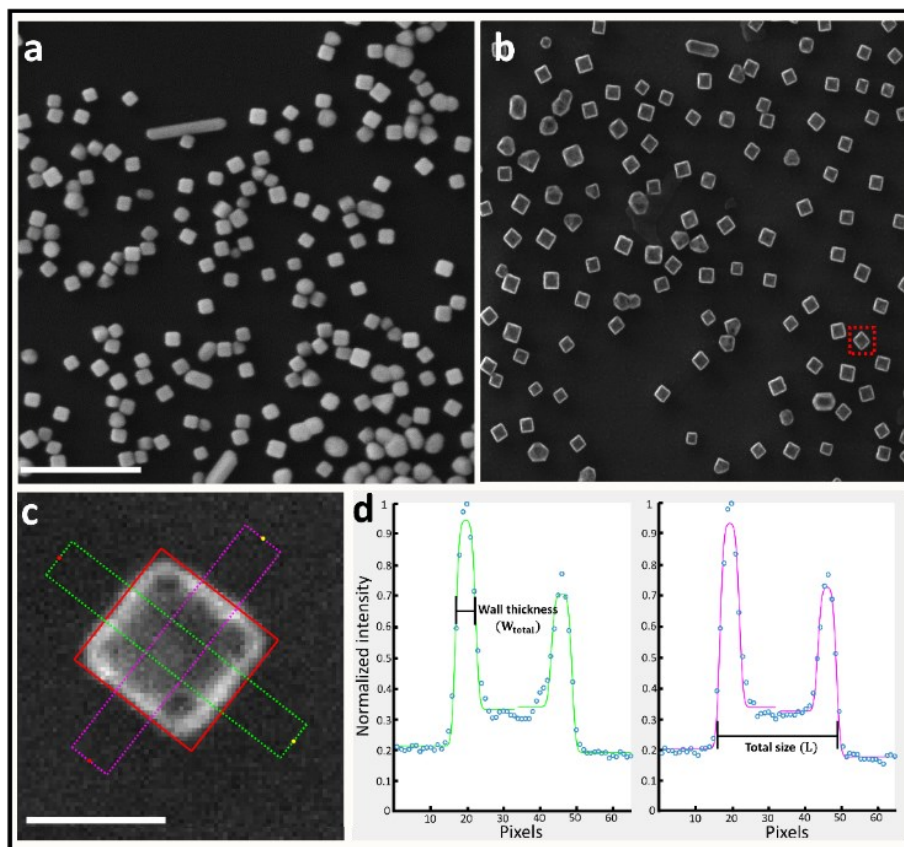


Figure 4.1 Structural characteristics of (a) AgNCs template and (b) its corresponding hollow-MNPs, visualized *via* SEM imaging. c) Analyses of a single hollow nanocube. d) Intensity profiles that correspond to the regions shown in c). The scale bar in a) is 500 nm, and in c) is 50 nm. The dotted red square in b) denotes the particle in c).

The statistics of the structural behavior of the small and large hollow-MNPs are compared in Figure 4.2. The evolution of their total size and wall thicknesses as a function of H_{Au}Cl₄ concentration is different for the two templates. For the small template, the total size of the hollow cubes increases by ~7 nm, on average, from the total size of the AgNCs template, and it stays constant with increasing concentration of H_{Au}Cl₄. On the other hand, the large hollow cubes (Figure 4.2b) show a different pattern. The size increment of the hollow cubes, from the large template's size, is negligible for the lowest concentration of H_{Au}Cl₄. However, as the synthesis is performed with more H_{Au}Cl₄, the hollow cubes' total size increases linearly. For the highest concentration of H_{Au}Cl₄, the hollow cubes are ~8 nm larger on average than their template. The hollow cubes' total wall thickness is the same for each template (~10 nm) and remains constant with H_{Au}Cl₄.

To further quantify this behavior and to set up reference regions for the physical discussion that will follow, here I introduce two geometrical quantities: "inner" and "outer" walls, such that their sum is equal to the total wall thickness of the hollow cubes. The reference boundary that defines these two regions is the full Ag nanocubes' outer surface, i.e., the template.

Therefore, the expression for these quantities can be written as:

$$\text{Equation 7} \quad W_{outer} = \frac{L_{hollowMNP} - L_{template}}{2},$$

$$\text{Equation 8} \quad W_{inner} = W_{total} - W_{outer},$$

Where W represents the wall thickness and L the size of the particle for each system, from a geometrical point of view, the outer wall corresponds to material that aggregates over the Ag template's surface. In contrast, the inner wall corresponds to the wall's component within the original template's surface, these representations are shown in the diagrams in Figure 4.2a, b. For instance, for the small template (47 nm) and lowest H_{AuCl₄} concentration (Figure 4.2a), the hollow cubes' total measured size is 54 nm, with a total wall thickness of 9 nm. It follows that the thickness of the outer wall for this synthesis condition is 3.5 nm, while the inner wall is 5.5 nm. This observation implies two things: 1) that some quantity of Au³⁺ ions have accrued over the surface of the Ag template, as the outer wall thickness is greater than zero; and 2) that some Au atoms have diffused into the outer layers of the Ag template, as the void stopped its development before reaching an inner wall thickness of zero.

For both templates, during the galvanic replacement process, Ag atoms are oxidized to reduce the Au³⁺ ions (presented in AuCl₄⁻), depositing Au atoms on the surface of the nanoparticle. With more Au atoms deposited, the outer wall increases its thickness while the void inside the particle simultaneously grows by the oxidation of Ag from the core.[49], [177] Additionally, inner wall thickness gets reduced by the spontaneous process of inter-diffusion, which occurs between the interfaces of Au (outer wall) and Ag (inner wall), as observed in Figure 4.2b, as well as the continuous oxidation of Ag under the galvanic replacement reaction. This process sets the geometrical limit to the expansion of the tetragonal void inside the nanoparticle.

Importantly, after the void is fully developed, morphologies on the nanoparticles' surfaces take distinct routes, depending on the template's size.

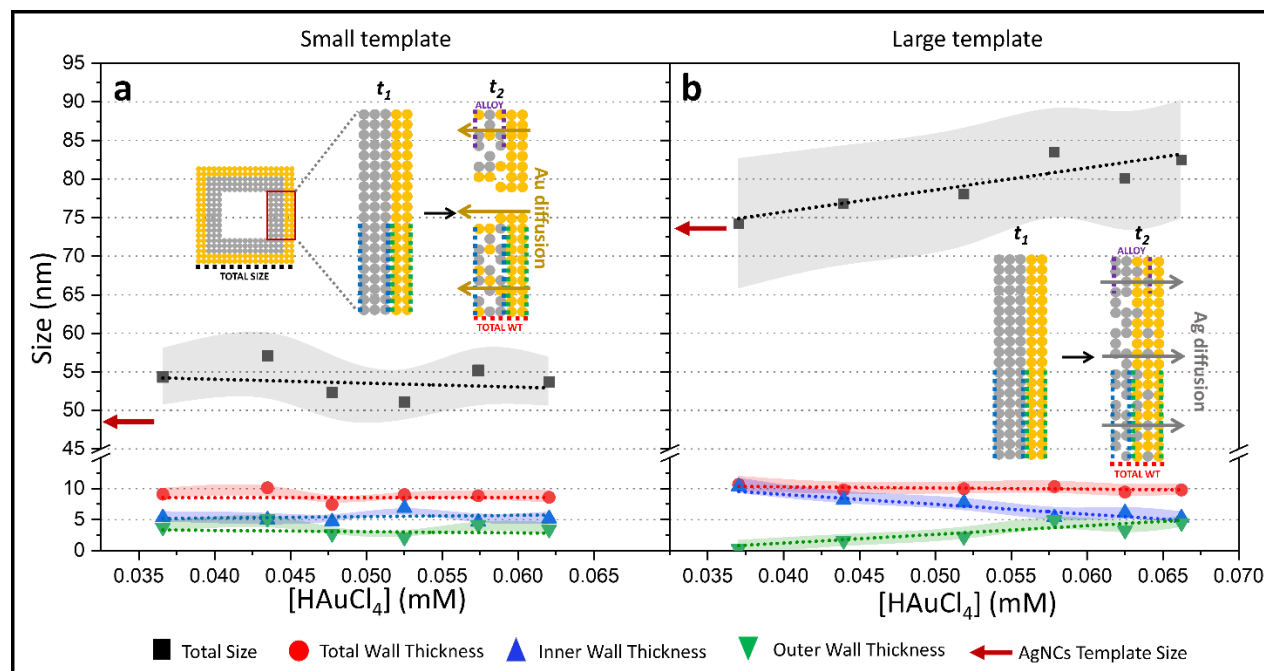


Figure 4.2 Evolution of total particle sizes and wall thicknesses of hollow-MNPs as a function of HAuCl₄ concentration for small and large AgNC templates. a) Total particle size and wall thickness remain the same with HAuCl₄. Inner and outer walls also remain the same. b) Total particle size increases linearly with HAuCl₄ concentration, but the total wall thickness remains the same.

Sub-particle features can be observed in Figure 4.3, which reveals surprising structural differences between the small and large templates. For the small template (Figure 4.3, top), increasing the concentration of HAuCl₄ beyond the point of the full void development produces pinholes on the face of the cube. The pinhole grows in diameter as the HAuCl₄ concentration increases, and the corners of the cube become truncated, adding additional holes to the structure. On the other hand, the large template (Figure 4.3, bottom) shows a different pattern after the inner void's full development. In this case, small pinholes appear upon increasing the concentration of HAuCl₄, and instead of growing in size, they grow in number.

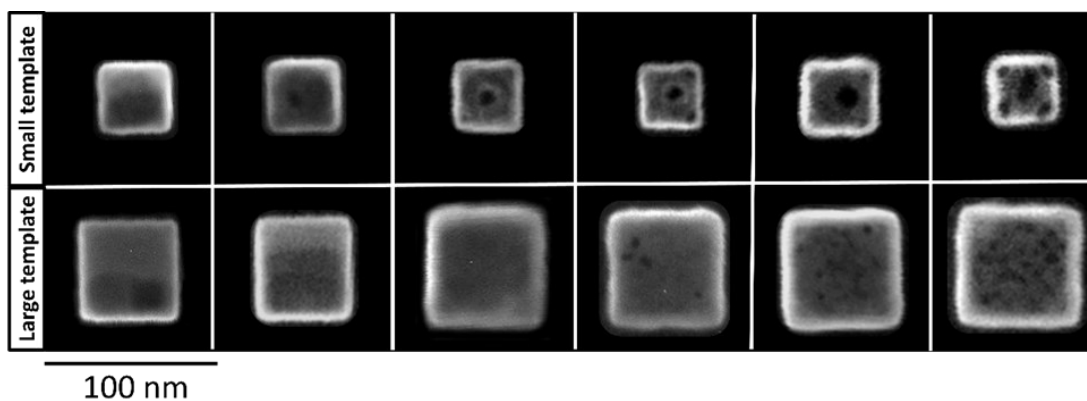


Figure 4.3 Structural evolution of the sub-particle features, voids, and pinholes, with increasing HAuCl_4 concentration (increases from left to the right) for the small (top) and larger templates (bottom).

This data demonstrates different surface features for the small and large template, which implies different chemical mechanisms involved in their formation. This difference can be explained in terms of the metallic species' net diffusion dynamics composing the alloyed nanoparticles. On the other hand, this diffusion dynamics is governed by the Kirkendall effect, a general phenomenon describing the net diffusion of two species with different diffusion times through vacancy exchange [178] and different surface tensions experienced by nanoparticles at different sizes.

For the large template, the dominant phenomenon driving the morphology evolution is based on the Kirkendall effect.[158, 159] The diffusion rate of Ag is higher than that of Au. Thus, Ag and Au's effective interface moves towards the outer surface as a larger number of Ag atoms migrate to the outer wall of the void nanoparticle, forming an alloy. In doing so, these Ag atoms close to the particle's outer surface can act as small nucleation sites. Once the GRR oxidizes the elemental Ag from the core, the Ag atoms diffused to the outer wall will get oxidized. This preference correlates with the species' stability, where elemental Ag is less stable than alloyed Ag. After the oxidation of these Ag-alloyed atoms, there will be small surface openings that I refer to as pores.

The hollow-MNP for the small template experiences larger surface tension, caused by its higher surface-to-volume ratio, to alter the alloy's net diffusion dynamics. As the studies of Murch *et al.* have shown it.,[63] small particles of metallic alloys will show defects such as partial Shockley dislocations, which can play an essential role in reconstructing the particle. [181] Importantly, the density of such defects on the outer wall increases with reduced nanoparticle size. It was shown that a Shockley partial dislocation could transport material from the outside to the inside for small nanoshells.[63] As the dislocation creates a channel for atoms to diffuse, atoms at the outer surface will preferentially diffuse to the inner surface due to the system's tendency to suppress the void formation.[63, 161] Contrary to what occurred with the larger particles, the occurrence of crystalline defects is sensitive to the nanoparticle's geometrical structure. They will appear preferentially at certain sites of the hollow cube instead of being distributed across its surface. Thus, a smaller number of nucleation sites for the pinholes appear in the small nanoparticles, growing in diameter as the galvanic replacement progresses.

I have captured bright field high-resolution transmission electron microscopy images of representative samples, which were synthesized by employing different reaction conditions depending on the use of small or large templates and depending on the concentration of H_{AuCl}₄. Those images are presented in Figure 4.4. Images of hollow-MNPs demonstrate the effect of galvanic replacement processes, including small and large templates, on their structure. In these images, the voids and pinholes' evolution is evident as it was observed already in SEM images presented before.

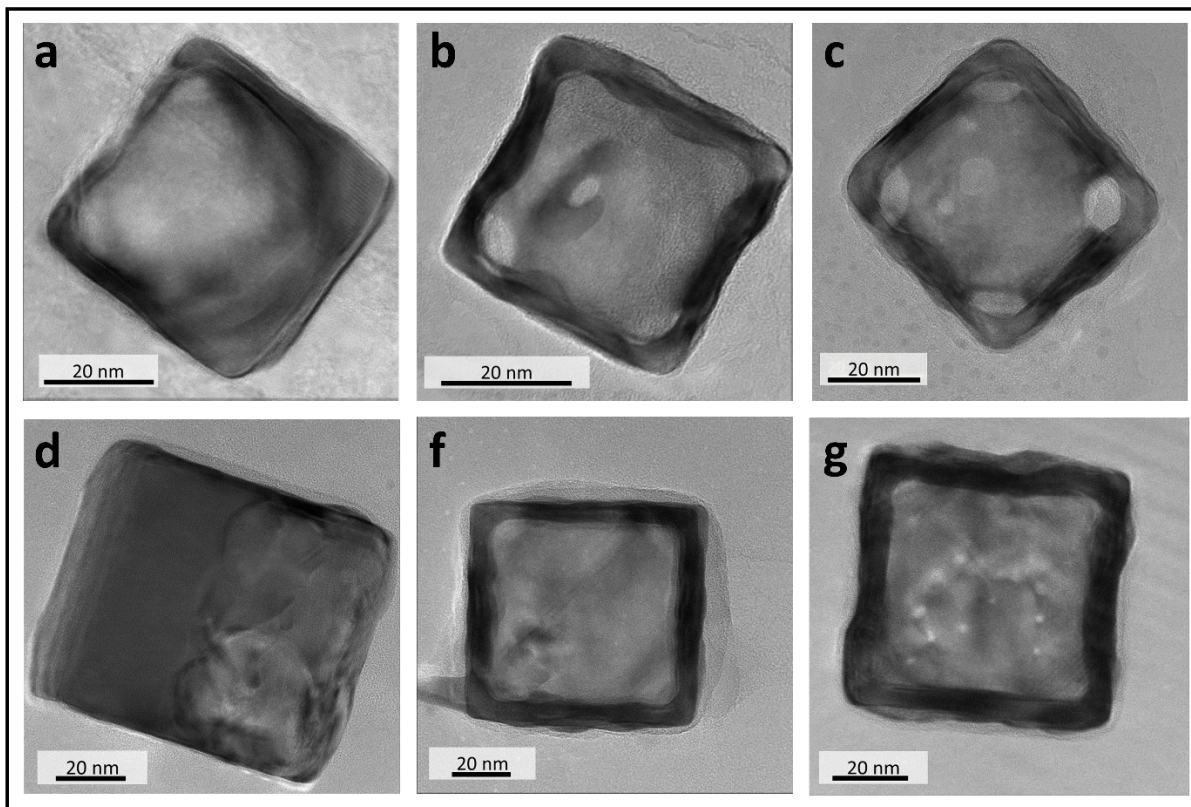


Figure 4.4 High resolution-TEM (HR-TEM) images for the representative hollow-MNPs for the small (a, b, c) and large (d, f, g) templates depending on the HAuCl_4 concentration increase from left to right.

Figure 4.5a shows a bright field HR-TEM of a hollow-MNP, which corresponds to the small template having the highest concentration of HAuCl_4 . With holes at the corners and the face, this representative image matches the corresponding SEM image, which I used for the statistical analyses. This agreement between SEM and the HR-TEM images. The lattice spacing value obtained from Figure 4.5b is 0.2 nm, which corresponds to the $\{200\}$ planes of Au or Ag face-centered cubic (FCC) structures.[162–164]

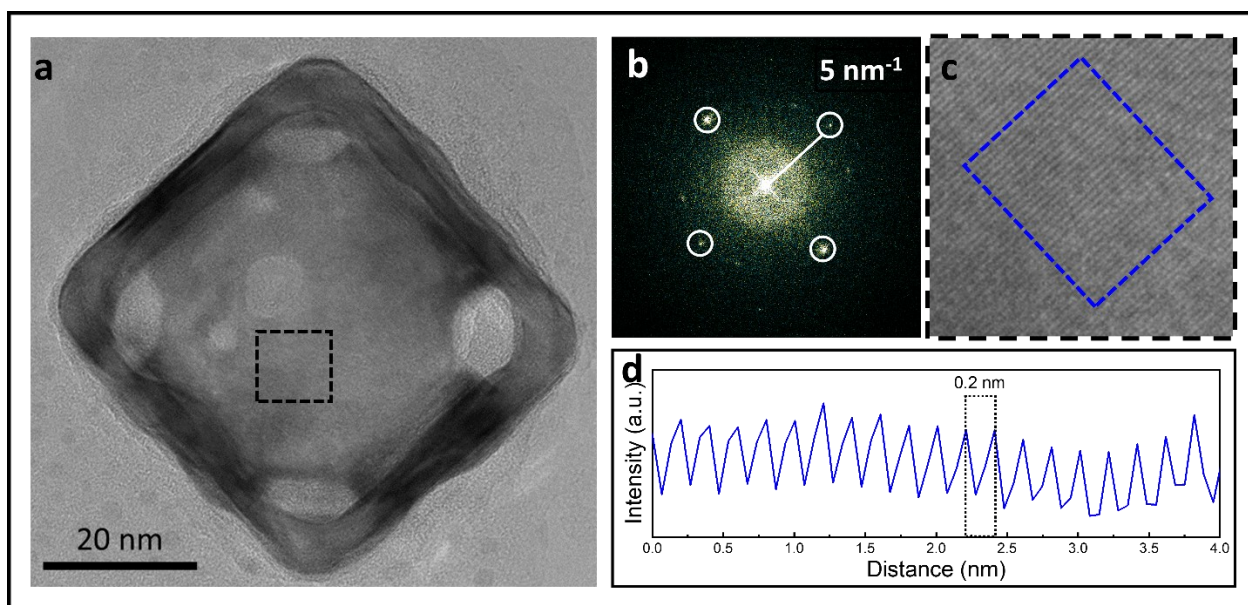


Figure 4.5 a) Representative high-resolution TEM image of a hollow-MNP synthesized using the small template and 0.062 mM of H_{AuCl₄}. b) Particle's Fourier transform in (a) showing a lattice measured at 5 nm⁻¹ from the center. c) Zoomed-in image of the region shown in (a). d) Line profile across the atomic columns reveals an interplanar spacing of 0.2 nm.

4.2 Optical characterization

Sub-particle morphologies observed above alter the optical properties of these nanoparticle systems. UV-Vis-NIR analyses were performed to connect optical properties to the concentration of H_{AuCl₄} and, hence, to different structural morphologies of the particles. Also, electrodynamic simulations were performed to support and understand experimental observations.

Figure 4.6 shows the UV-vis-NIR analysis for small and large hollow-MNPs as well as the AgNCs templates for each size. The spectra for AgNCs show the characteristic plasmonic absorptions for these nanoparticles, which is similar to the results reported by Hung *et al.* [186]. For small hollow-MNPs (Figure 4.6a), there is a red shifting of the main LSPR peak by increasing the concentration of H_{AuCl₄}. Similarly, large hollow-MNPs also show a red LSPR peak shifting by increasing the chloroauric solution's concentration.

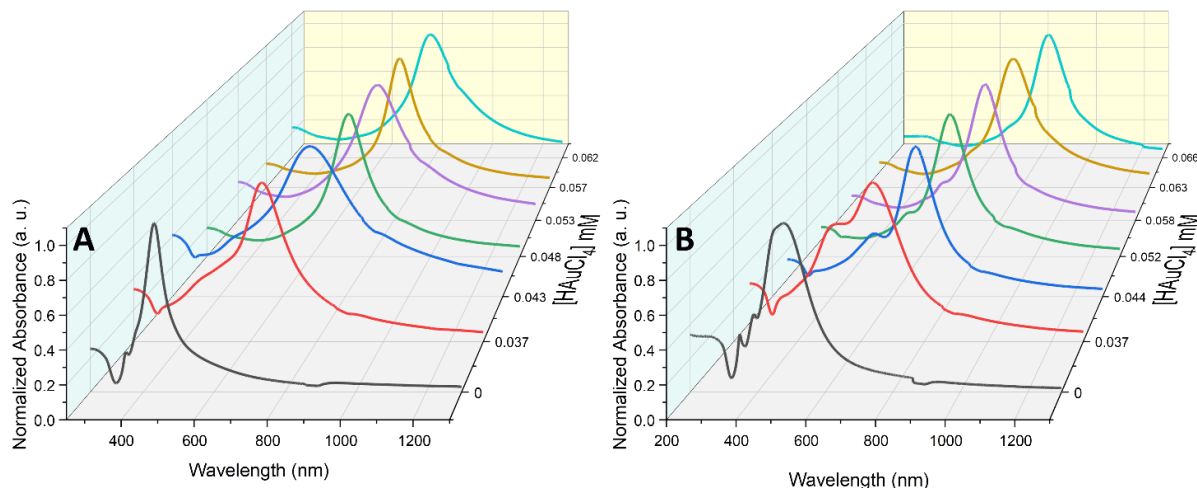


Figure 4.6 Absorbance spectra of AgNCs (black) and hollow-MNPs for the a) small and b) large templates at different concentrations of HAuCl₄. The main LSPR peak has a red shifting in both templates by increasing the concentration of HAuCl₄ during the GRR.

4.2.1 Structural and alloy effect on the optical properties of hollow-MNPs

In section 4.1, Structural characterization, we observed that the structural information such as the total size and wall thicknesses lead to different diffusion mechanisms on the hollow particles, small templates have a diffusion of Au into the inner wall (rich in Ag atoms), and large templates have a diffusion of Ag into the outer wall (rich in Au atoms). These mechanisms explain the behavior of hollow-MNPs during the GRR. With this information and observing the sub-particle morphologies for both templates through electron microscopy, I decided to compare the red LSPR shifting of the experimental analysis with electrodynamic simulations of models of hollow-MNPs for both templates. These models include the information of the structural dimensions of the particles (e.g., size and wall thickness) and the variation of different alloy gradients for small (variation in the inner wall) and large (variation in the outer wall).

Figure 4.7 reveals a linear relationship between HAuCl₄ concentration and the main peak's central wavelength of experimental analysis. The redshift is also observed in the electrodynamic simulations that follow the models shown at the top of the figure. Initially, it begins with the development of the void, and the redshift trend continues after the void is fully developed due to the additional morphological features appearing on the surfaces of the hollow-MNPs. Pinholes open up in the particle's walls, further shifting the plasmonic

resonances towards higher wavelengths. The underlying physics behind this behavior is like the particle-cavity mode hybridization. However, the interaction occurs between the resonances extending across the particle's total size and those localized around the surfaces' hollow features. The explanation about the plasmonic modes' hybridization with the sub-particle features will be discussed in section 4.2.2.

The LSPR location of the simulations inside the FWHM of the experimental LSPR peak of the nanoparticles' ensemble explains the broadening of the peak in experimental results caused by the variation of distinct sub-particle morphologies during the GRR.

Moreover, the alloying gradient is shown in Figure 4.7 using the dielectric functions for several Au/Ag alloys and the dielectric functions of pure Au and Ag in two distinct wall regions. In this alloy variation, we can observe that when the pure elements are selected (for each size's respective wall thickness), the redshift is large compared to the LSPR position when the alloy gradients are used. This behavior is due to the large difference in Au and Ag's dielectric function that causes the large redshift compared to the short shift when alloys are used. Changes in the alloy composition do not affect the position of the plasmonic resonances significantly. The dominant contribution to the LSPR is from the geometrical features, voids, and pinholes. Due to the no major contribution from the alloys gradient in the hollow nanoparticles' walls, I decided to perform from now on alloy gradients closer to the experimental expectation. The gradients that will be used for our electrostatics simulation will be for small hollow-MNPs on the inner(Au10Ag90)/outer(Au) walls and for large hollow-MNPs an inner(Ag)/outer(Au90Ag10) walls thicknesses.

Finally, I also simulated the experimentally observed structures with a wall thickness corresponding to 50% of the measured average wall thickness. The redshift increment is higher if we compare the LSPR peak position for the experimentally calculated wall thickness and its half. This comparison shows that the variation of the wall thickness we have in our synthesis may also affect the FWHM of the plasmonic modes due to the presence of different thicknesses.

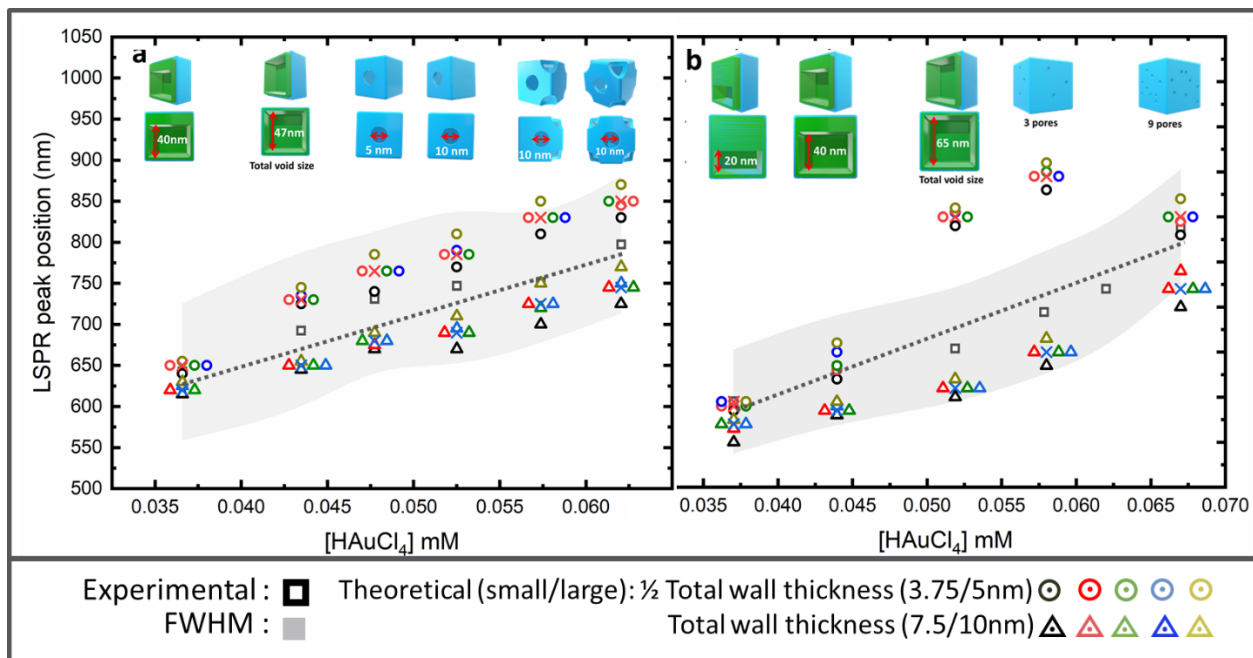


Figure 4.7 LSPR peak wavelength from the experimental absorbance spectra as a function of HAuCl₄. Theoretical results for various structures shown at the top, which corresponds to experimental structures, with a total wall thickness of 7.5 nm (blue) and 3.75 nm (red) for the small template in a); 10 nm (blue) and 5 nm (red) for the large template in b).

The hybridization model for a nanoshell can explain these redshifts caused by the thinner wall thicknesses. The model is schematically shown in Figure 4.8. The energy-level diagram describes the excitation mechanism of the hybridized plasmon resonances in metal nanoshells by the interaction between the sphere surface (ω_{sp}) and inner cavity (ω_c) surface plasmons. In this mechanism, two dipolar modes are created due to the interaction of a void/shell system created due to the hybridization of a metallic sphere's dipolar modes and a dielectric void in a metallic substrate. The hybridization is enhanced if the thickness of the shell decreases, as shown in Figure 4.8b,c; and this process causes a shifting of the plasmon resonances. This redshift means that an anti-symmetrically coupled anti-bonding mode (ω_+) and symmetrically coupled bonding mode (ω_-) are generated in the metallic shell.

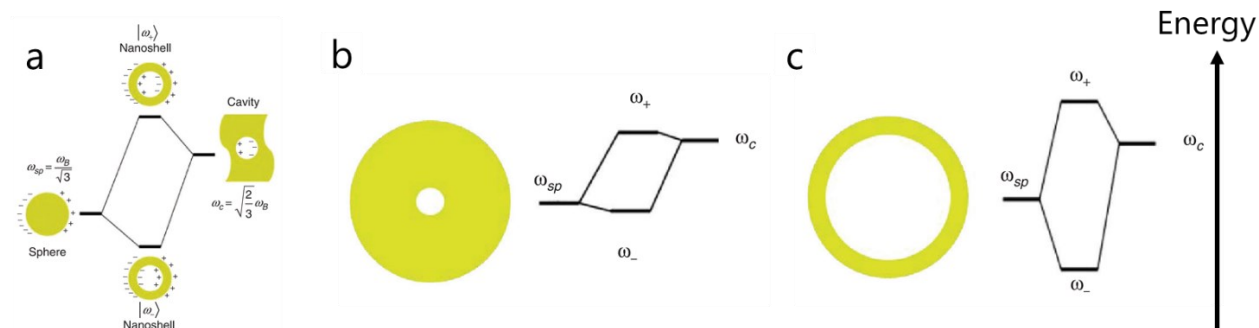


Figure 4.8 Schematic representation of a plasmon hybridization mechanism (a) with thick (b) and thin (c) shells. The general explanation is describing the plasmons that a metal nanoshells shows, due to the coupling between the anti-symmetrically mode (ω_+) and symmetrically mode (ω_-). The hybridization is enhanced when if a thick metallic shell (b) gets thinner (c). Adapted from “Playing with Plasmons: Tuning the Optical Resonant Properties of Metallic Nanoshells”. Halas N. Cambridge University Press. 2011. [187]

The wall thickness effect can be also observed during the formation of the void of hollow-MNPs. Figure 4.9a shows the absorbance spectra for the AgNCs templates and the corresponding hollow-MNPs. In the figure, a redshift in the main resonance peak with an increasing concentration of HAuCl_4 is evident. Furthermore, the optical response of these partially hollowed nanocubes (due to low concentrations of HAuCl_4) shows a clear change in the spectral shape of the main absorption peak, with a shoulder's appearance on the high-energy side of the main resonance. This shoulder is particularly clear in the data for the large template. The development of the void in the nanocube's body plays a critical role in this shoulder resonance's appearance and strength, as shown in Figure 4.9b.

As the internal void grows within the MNP, its fundamental dipolar mode becomes more complex due to the individual modes' coupling on the outer and inner surfaces.[166, 167] Here, the outer surface is associated with the nanocube, and the inner surface with the void, illustrated in the inset of Figure 4.9b. This figure also compares one experimental spectrum with three theoretical spectra. Synthesis-wise, the experimental spectrum corresponds to a concentration of 0.038 mM of HAuCl_4 , and its representative SEM image can be seen in the leftmost bottom panel of Figure 4.3. Importantly, the void does not develop from the center but from one side of the MNP, as seen in the figure, thus breaking

the cube's symmetry. This phenomenon induces an off-center cavity mode that interacts strongly with the charge distribution on the outer surface of the MNP, hybridizing the outer and inner-surface modes and, hence, shifting their energies.

In Figure 4.9b, three theoretical spectra highlight the critical role of this coupling in optical absorption. The first spectrum (blue) shows the extinction cross-section, averaged over light's incidence direction, of a nanoparticle with a void and a wall thickness of 10 nm. The theoretical plasmon peak agrees well with the colloidal nanoparticles' main absorbance peak, but it lacks the high-energy shoulder present in the experimental data. In the second and third spectra, I included the coupling and tuned its strength by changing the model structure's wall thickness. Thus, when I scale the wall thickness down by 25%, I observe a new plasmonic mode arising in the theoretical extinction profile.

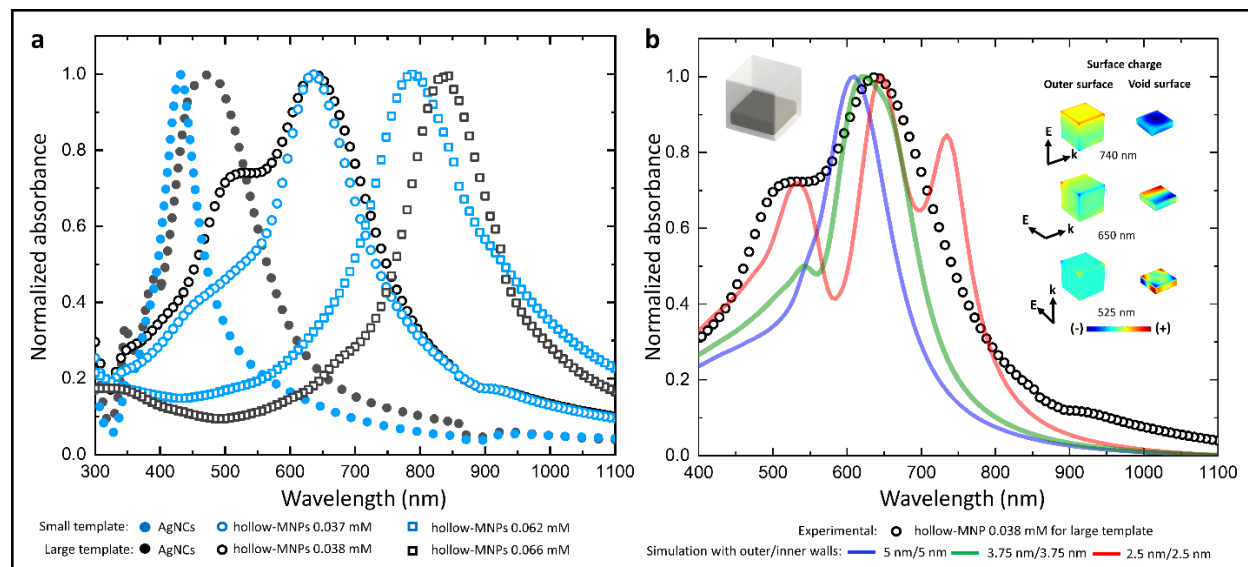


Figure 4.9 a) Optical response of nanocube ensembles: absorbance spectra of AgNCs templates and hollow-MNPs. b) Optical spectra comparison between experimental and theoretical results. The theoretical simulation was performed for a particle with a total size of 75 nm and an inner/outer wall composition of Ag (pure)/ Au₉₀Ag₁₀ with a void along the z-direction.

By further increasing the coupling strength, corresponding to a wall thickness of 50% of the original value, we find that a more complex optical response arises from the hybridization of the plasmonic modes. In Figure 4.9b, a good agreement between the experimental data and the theoretical results is evident, with hybridization explaining

certain parts (the shoulder) better than without hybridization. Overall, this comparison highlights the strong impact the internal geometry of the MNPs has on the optical absorption of these nanoparticles.

Furthermore, as the concentration of HAuCl_4 increases, the shoulder peak decreases in intensity, as seen in Figure 4.9a, a strong experimental indication that a void inside the nanocube causes the shoulder. In parallel, as the void increases in size, the interaction between the particle and void-plasmonic modes couple stronger, which further contributes to the redshift of the main LSPR resonance.

4.2.2 Effect of structural properties of hollow-MNPs on the hybridization of the plasmonic modes

In the previous section, we observed how the redshift of the small and large hollow-MNPs is explained by the structural modification (e.g., size and wall thicknesses) and sub-particle morphologies formation coupling of the plasmonic modes associated with the inner and outer surfaces in the MNPs. However, in this section, I will explain the hybridization of the plasmonic modes for our hollow-MNPs and the effect of a thinner wall thickness on the redshift of the plasmonic peak.

Figure 4.10 and Figure 4.11 show detailed data for the three irreducible light polarizations for the MNPs with a void height of 20 nm (panel a) compared to the equivalent geometry with a fully developed void (panel b). Together, panels (a) and (b) illustrate the impact of the geometrical asymmetry over the optical spectra.

The difference between Figure 4.10 and Figure 4.11 is the degree of coupling between particle and cavity plasmonic modes, modeled through the wall thickness. Figure 4.10 shows results obtained from the geometry with wall thickness equal to the mean experimental value (See Table 2 and Table 3), while Figure 4.11 uses half of these values.

For Figure 4.10 and Figure 4.11, panels a, complement the discussion around Figure 4.9b in the main text. Here we see the spectra of each independent light polarization, and we can better identify the interaction between specific modes and how do they relate to the broken cube symmetry of the model's geometry. Particularly, we see the clear

difference between the spectra under light polarized along the y and z directions in Figure 4.10a.

The equivalent difference is not as appreciable in the weak coupling regime, i.e., Figure 4.10a, which is partly why this geometry did not produce the shoulder in the average data depicted in Figure 4.9b in the main text. The other factor is that for the thicker wall data (Figure 4.10), the coupling is not strong enough to hybridize the outer and inner modes.

The high-energy cavity modes in Figure 4.10 can be seen in the absorption cross-sections (or through monitoring the quadrupole component of the multipolar expansion of the charge distribution), but this is not enough to appreciably change the global extinction spectrum. This changes when the coupling becomes strengthened (Figure 4.11a), and the hybridization of the modes separates them in energy and changes their spatial symmetry, converting both high- and low-energy resonances in bright modes noticeably contribute to the global extinction cross-section of the MNP.

Comparing panels (b) from Figure 4.10 and Figure 4.11 straightforwardly evidences the effect of the increased coupling. The main plasmonic peak becomes strongly redshifted upon reducing the wall thickness (increasing coupling strength), and so does the secondary peak as additional higher-order modes appear at higher frequencies.

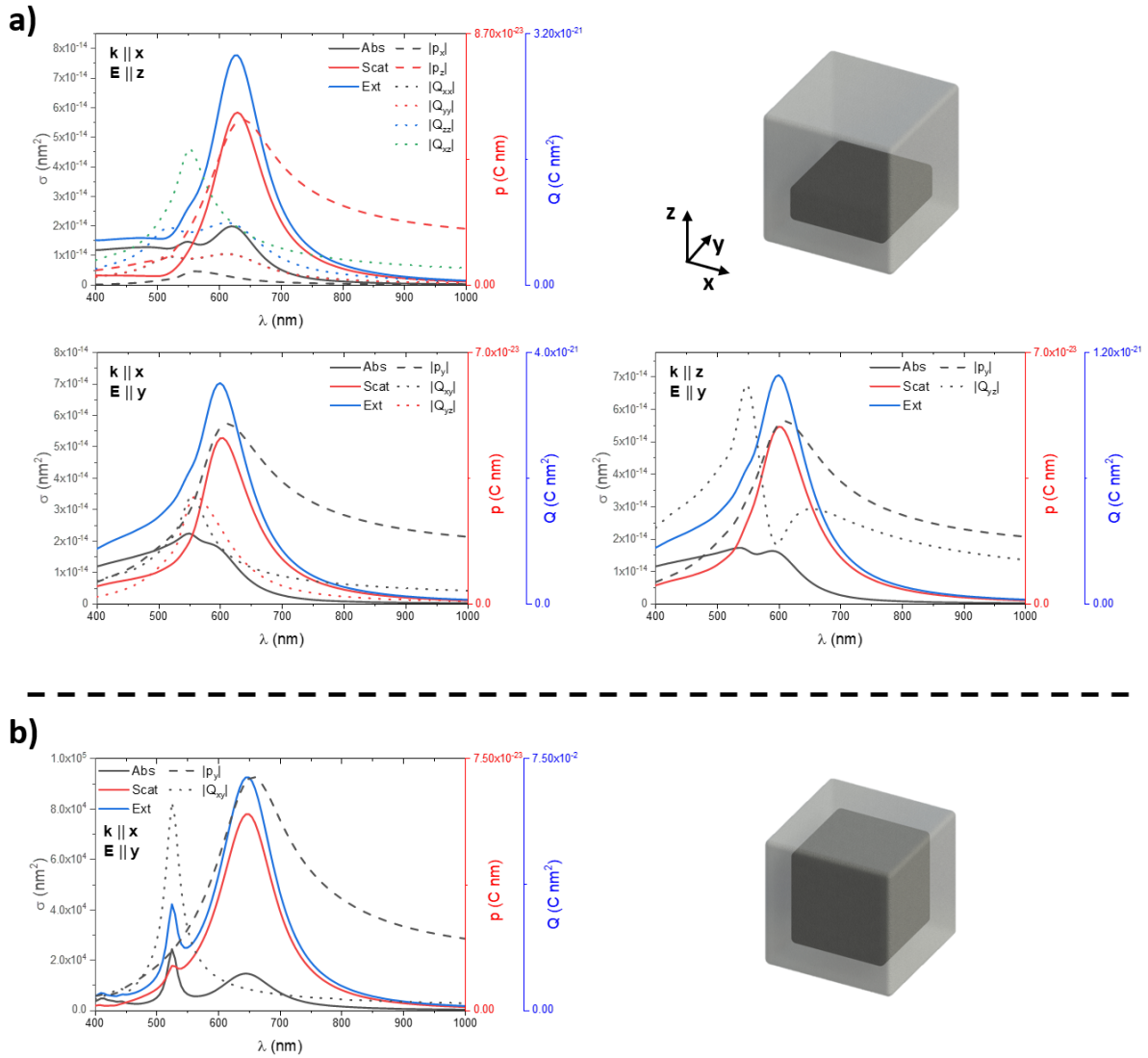


Figure 4.10 Weak coupling. Optical cross sections (σ) and dominant dipolar (p) and quadripolar (Q) moments of the charge distribution in the particle with a $55 \times 55 \times 20$ nm void (panel a) and a $55 \times 55 \times 55$ nm void (panel b).

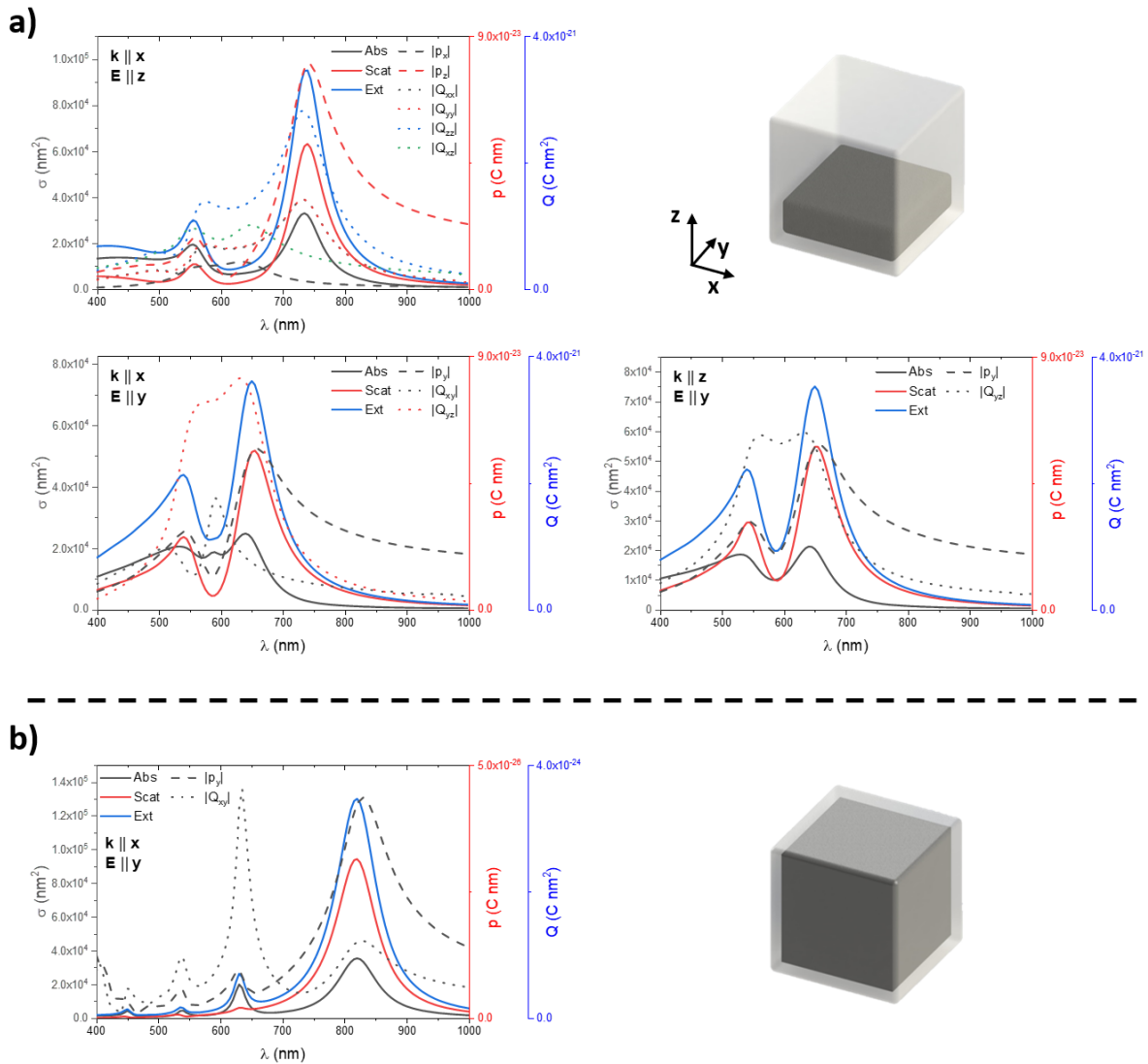


Figure 4.11 Strong coupling. Optical cross sections (σ) and dominant dipolar (p) and quadripolar (Q) moments of the charge distribution in the particle with a 65x65x20 nm void (panel a) and a 65x65x65 nm void (panel b).

Lastly, Figure 4.12 illustrates a similar phenomenon, occurring in the MNPs with open features at their surfaces, which explains the continuing redshift when increasing Au concentration after reaching the point of full void development. In this case, it is the additional high-frequency hole plasmonic modes that interact with the main full-particle excitation and thus drive the redshift in the last sets of datapoint in Figure 4.7 in 4.2

Optical characterization. Interestingly, we can see that these high-frequency modes are dark modes, and their scattering cross section is negligible.

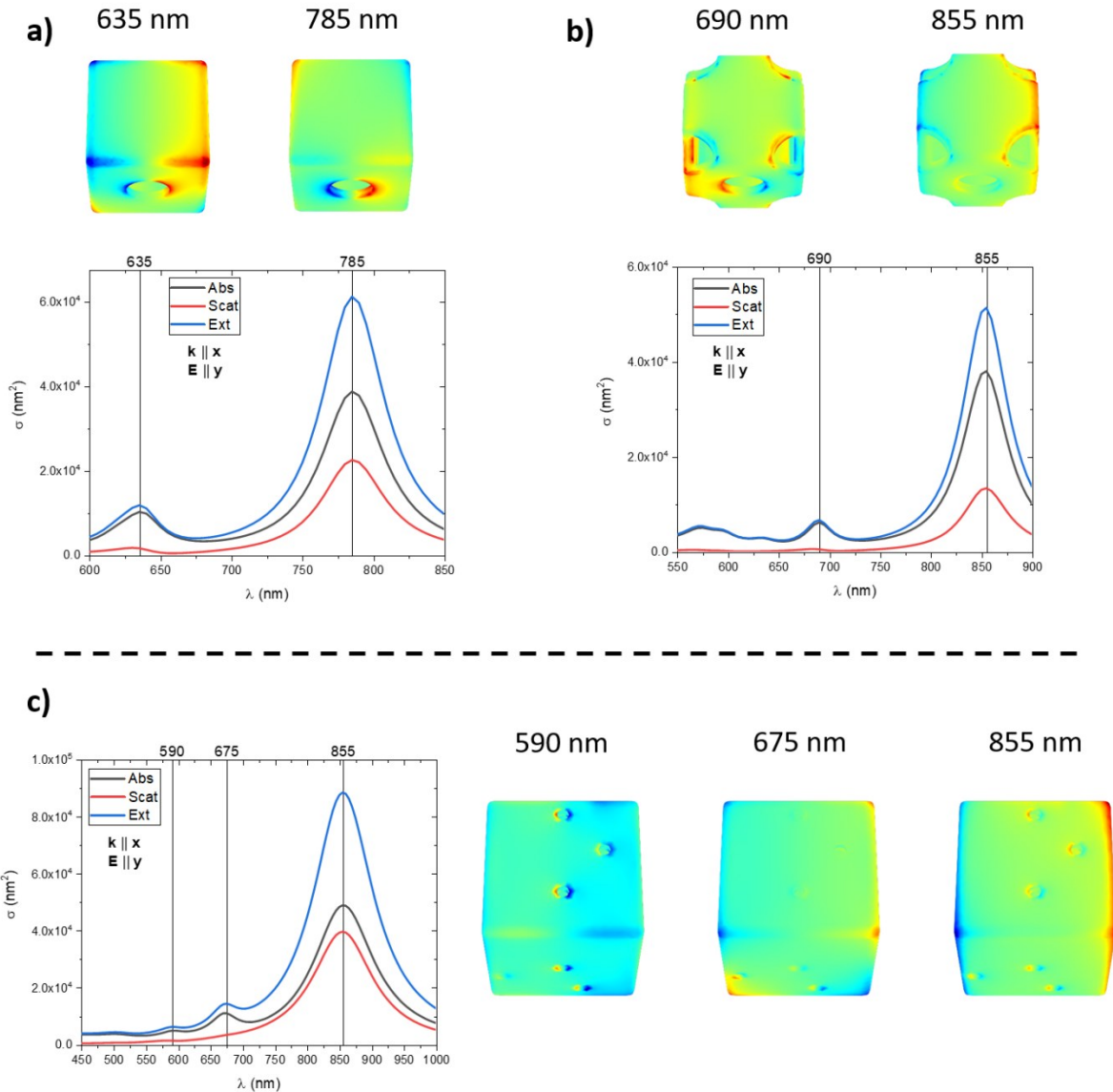


Figure 4.12 Strong coupling. Interaction cross-sections σ and surface charges for MNPs with wall thickness equal to one half the values presented in Table 1 and Table 2, showing the strong-coupling regime between the charges at the outer and inner MNPs' surfaces. We showcase results for specific light incidences, illustrating the spatial symmetry of the main plasmonic modes. The data has been

chosen from representative geometries with fully developed voids and hollow surface features. a) Small template, single pinhole. b) Small template, single pinhole, eight truncated holes. c) Large template, three pinholes per face.

4.3 Cargo release of hollow-MNPs

In the previous chapter, we observed the changes in the optical properties by modifying the structure of the hollow-MNPs. The LSPR, which is a structure-dependent property, is also directly correlated to the thermal property of hollow-MNPs. When an external energy source interacts with a plasmonic particle, strong surface fields are induced due to the electrons' coherent excitation (LSPR). The rapid relaxation of these excited electrons produces strong localized heat. In our work, I will use the interaction of an e-beam with hollow-MNPs, increasing the local heat of the hollow particle, triggering a cargo release. Specifically, cargo-loaded hollow-MNPs will be exposed to an e-beam at 200 kV, which is also used for imaging characterization. Figure 4.13 summarizes the physical steps involved in our experiment.

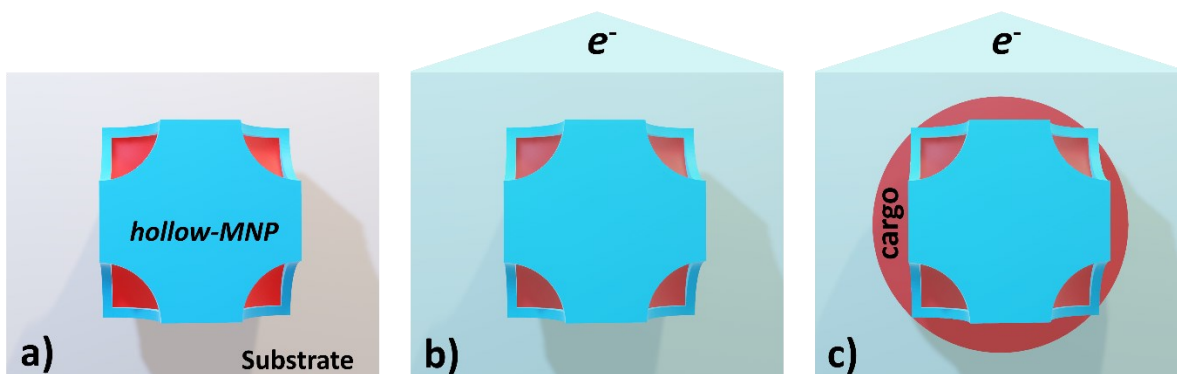


Figure 4.13 Schematic representation of the e-beam induced cargo release process from a hollow-MNP. First, the hollow-MNP filled with cargo is placed into a TEM grid (a). The particle is irradiated under the e-beam (b), increasing the local temperature, causing cargo melt (c).

I performed a collection of bright-field TEM images of hollow-MNP that vary in sizes and sub-particle features such as open corners, pores, pinholes and compared their effect on

the cargo release rate. All the experiments were done under the same conditions on the same substrate for the TEM grid with similar e-dose for every experiment.

The analysis of the cargo release was performed using Matlab software with a custom image processing algorithm. The images were analyzed by applying a threshold to select the darker areas for both the hollow-MNP and the cargo released. Then a mask was applied to the specimen's area, and then the calculation of area was automatically taken from the dimension value in nanometers. It is important to mention that each image from the same stack was analyzed automatically. Each stack of bright-field TEM images contains approximately 800 images. Each image is taken at a specific time from the initial release until 30 min. Figure 4.14 shows the image processing performed in Matlab.

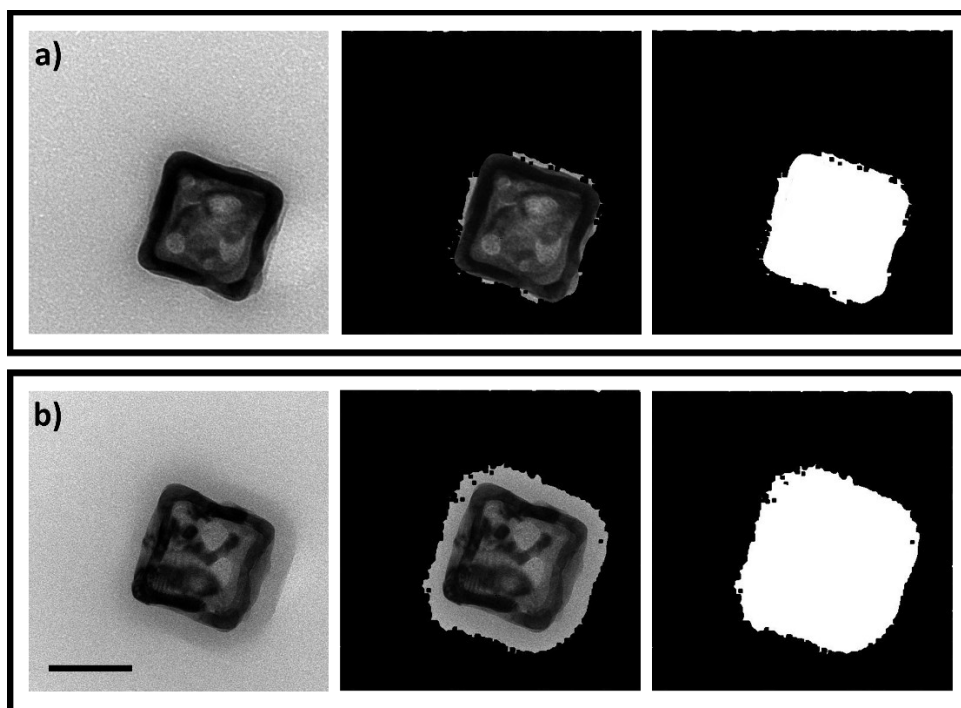


Figure 4.14 Imaging processing through Matlab software. Bright-field images for a small hollow-MNP at initial (a) and 30 min (b) after release. The images are treated with a threshold that will select darker areas that will be masked (right images). The area is calculated through the conversion of pixels to nanometers. The scale bar is 50 nm.

The original image is transformed into a black and white image, differentiating the cargo and the nanoparticle from the rest of the image, which corresponds to the substrate. The process begins with the first image of the stack, which is considered the first area value.

The first image contains an "extra" area from the cargo due to the immediate release. Equation 9 represents the value obtained by comparing the areas from the initial image to the consequent ones. The value obtained is the ARR, where A_i and A_f represent the initial and final areas, respectively.

$$\text{Equation 9} \quad ARR = \frac{A_f}{A_i}$$

I will discuss the differences in cargo loading and release on small and large nanoparticles in the following paragraphs. The ARR calculation will be plotted and compared for each category of the number of open corners for different sizes. These categories are four, three, and one open corner, represented from now on as 4-OpCo, 3-OpCo, and 1-OpCo, respectively.

4.3.1 Structural characterization of hollow-MNPs by bright-field TEM imaging

In these experiments, the e-beam from the TEM microscope will interact with the hollow-MNPs increasing their local temperature. The heat produced by this interaction will be transferred to the cargo and the substrate. The cargo, composed mainly of 1-tetradecanol, possesses a melting point of around $\sim 40^\circ\text{C}$. The increase of temperature overpasses the cargo's melting point, causing its release and expansion from the hollow-MNPs and the substrate.

Figure 4.15 shows the small hollow-MNPs with different sub-particle features after the process of cargo loading. The nanoparticles were exposed to the e-beam, and bright-field images were taken from the initial release until 30 min after exposure. In Figure 4.15a, the hollow-MNP with half void does not release any cargo, compared to the particles with three and four open corners, as seen in Figure 4.15b and c. Because all the experiment was done under the same conditions, it suggests that either the cargo was not loaded initially, or its release was prohibited. One explanation for this behavior is that the pore or pinhole size will affect how the hollow-MNPs will load or release the cargo.

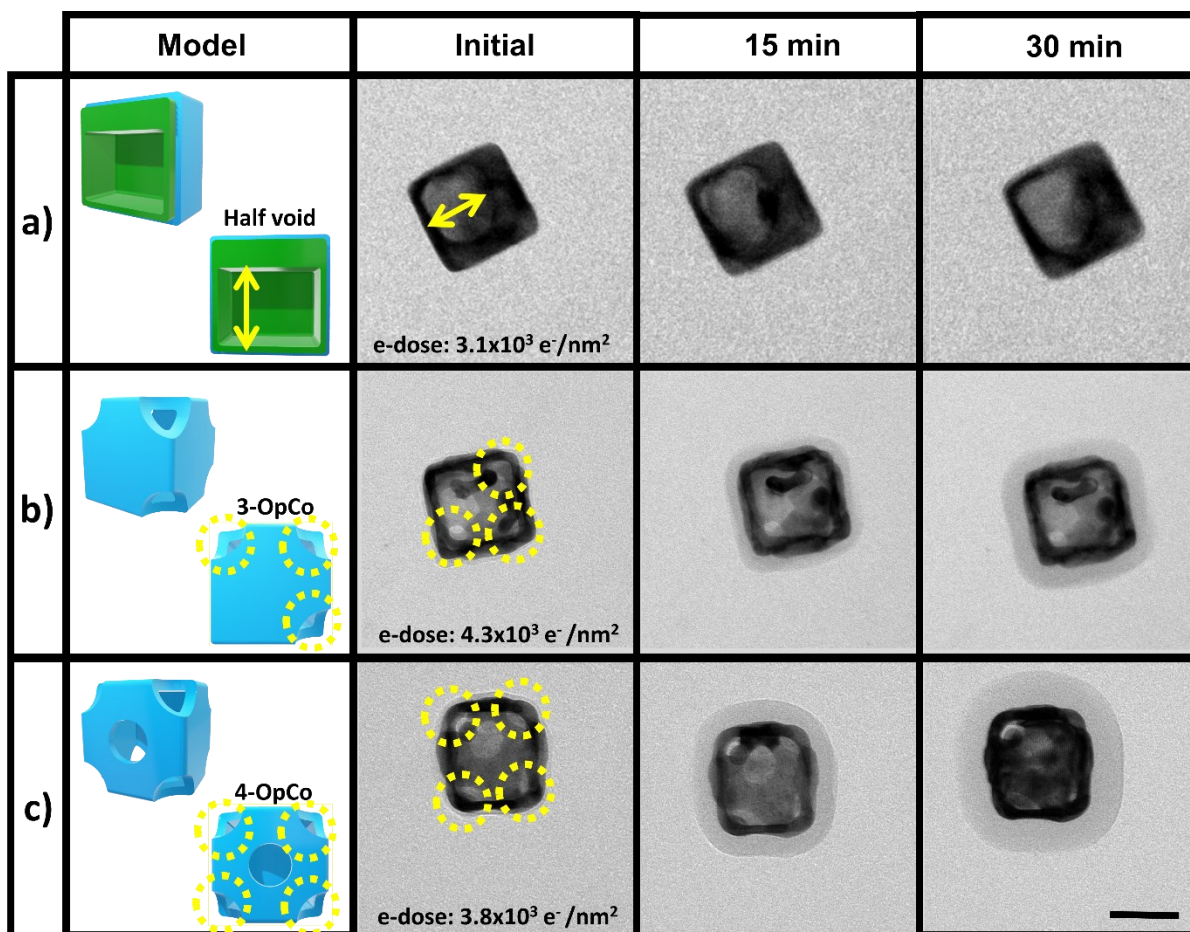


Figure 4.15 Bright-field images for different sub-particles morphologies for small hollow-MNPs after the cargo loading process. The comparison is made for the observable sub-particle morphologies in the structure, for (a) half void, (b) three open corners (3-OpCo), and (c) four open corners (4-OpCo). Models shown on the left represent the sub-particle morphology for the corresponding analyzed category. The scale bar is 50 nm.

To understand the behavior of hollow-MNPs before and after the cargo loading process, I decided to irradiate un-loaded, hollow nanoparticles with the e-beam. Figure 4.15 shows hollow-MNPs exposed to the e-beam for 30 min with the same sub-particle morphology as the particles with a cargo loading process. Here, we could observe that for all the morphology categories, the nanoparticles do not show any modification during the irradiation with the e-beam. This analysis also helps to explain the surrounding gray area presented in the initial image of Figure 4.15c. This grey area is not shown in any hollow-

MNPs that did not undergo a cargo loading process. It means that the grey area presented in Figure 4.15c is due to the instant cargo release, while not due to PVP presence.

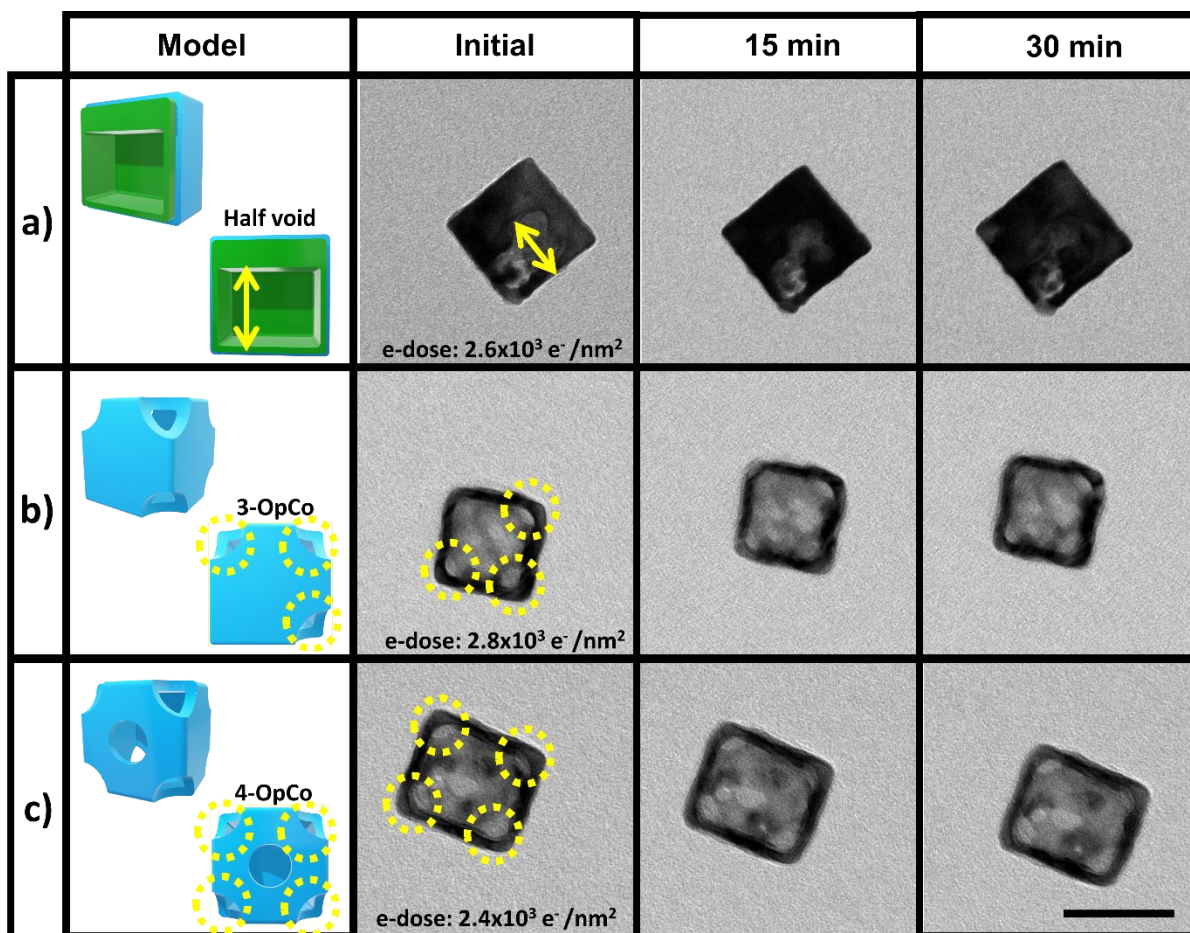


Figure 4.16 Bright-field images for different sub-particles morphologies for small hollow-MNPs without a cargo loading process. The comparison is made for the observable sub-particle morphologies in the structure, for (a) half void, (b) three open corners (3-OpCo), and (c) four open corners (4-OpCo). Models shown on the left represent the sub-particle morphology for the corresponding analyzed category. The scale bar is 50 nm.

In another experiment, large hollow-MNPs with sub-particle morphologies of half void, full void, and pores underwent a cargo loading process. Figure 4.17 shows the bright-field images of large hollow-MNPs with different sub-particle morphologies during the process of cargo release. In Figure 4.17a, b and c, it is observable that none of these particles release cargo as it was seen in the small hollow-MNP during the TEM imaging process.

Here, I still doubt if the cargo was not loaded initially or if the release was prohibited, like in small hollow-MNPs with a half void.

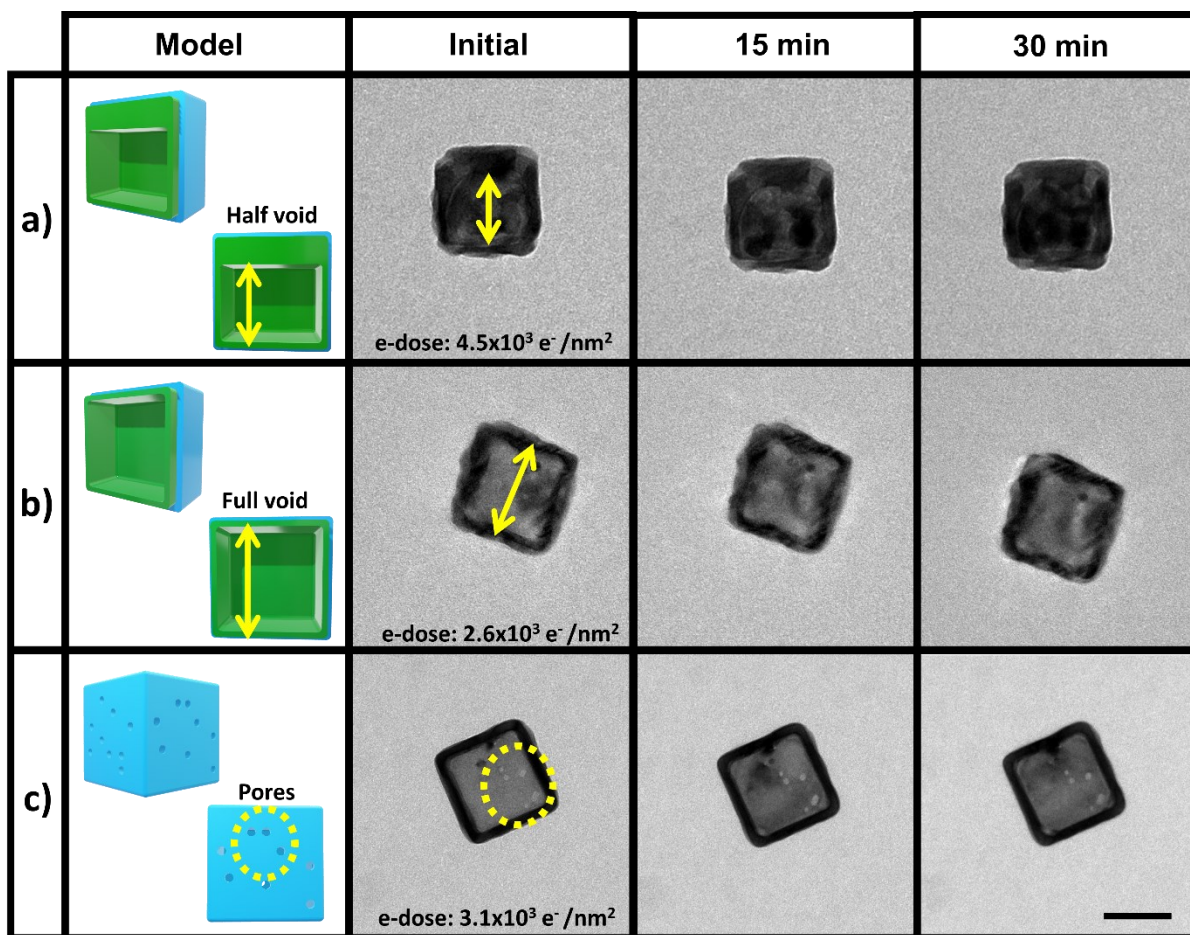


Figure 4.17 Bright-field images for different sub-particles morphologies for large hollow-MNPs after the cargo loading process. The comparison is made for the observable sub-particle morphologies in the structure for (a) half void, (b) full void, and (c) pores. The scale bar is 50 nm.

As was observed by Skrabalak *et al.* [49], there is a formation of a small pore at the beginning of the galvanic replacement reaction. Half void hollow-MNPs (for small and large templates) are the initial structure obtained during the GRR. Also, they are the ones that possess the small pore in which the ionized Ag ions can be taken out from the inside of the structure that creates the void. The tiny pore with a size smaller than 3 nm formed here is not large enough to allow 1-tetradecanol to be loaded or released from the structures. The same hypotheses can be used to explain the absence of cargo release

for the large hollow-MNPs. Large hollow-MNPs with the full void and those with both full void and small pores on their surface do not release for the same reason as half void particles. As seen in chapter 4.1-Structural characterization, with increasing concentration of HAuCl_4 , pores' development on the cube faces is evident, and they become larger as the reaction continues. However, the pore's diameter is 5 nm, smaller than the open corners (~ 10 nm in diameter) presented in small hollow-MNPs. This dimension difference of these sub-particle features could explain the absence of cargo in large hollow-MNPs. In the following title of this chapter, I will explain the importance of the size of the sub-particle morphology and the PVP presence with the release of cargo. Figure 4.18 shows the hollow-MNPs that were not exposed to the cargo loading process. These particles do not show any change or modification on the structure or the surrounding area, as shown by the large particles exposed to the cargo. These observations suggest that the cargo was not loaded or released in the particles at any sub-particle morphology shown in Figure 4.17.

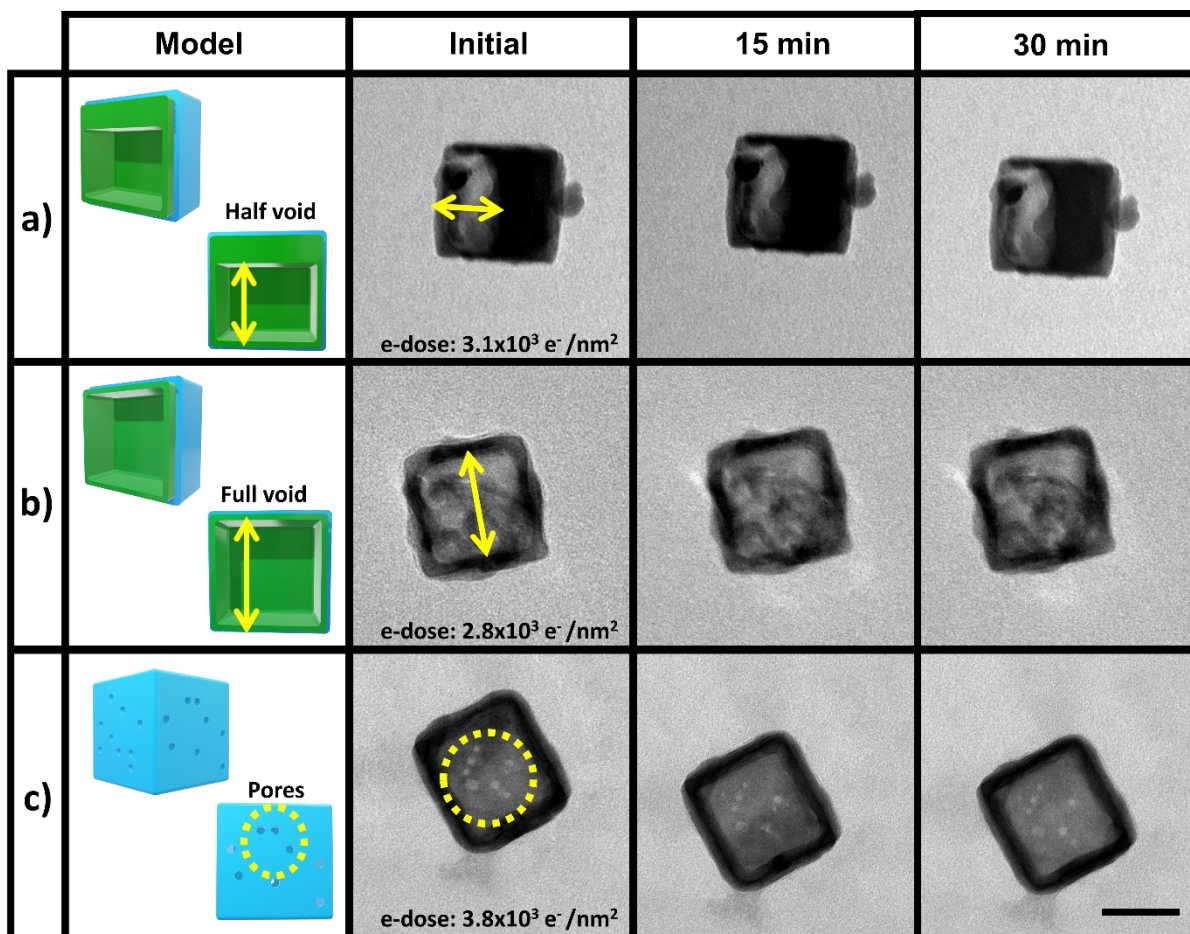


Figure 4.18 Bright-field images for different sub-particles morphologies for large hollow-MNPs without the cargo loading process. The comparison is made for the observable sub-particle morphologies in the structure for (a) half void, (b) full void, and (c) pores. The scale bar is 50 nm.

4.3.2 Cargo detection on small and large hollow-MNPs

In another experiment, I observed in detail the releasing process from a small hollow-MNP with 1-OpCo. Figure 4.19 shows that the release starts from the open corner covering the surrounding nanoparticle before expanding. These observations allow us to infer that open corners are important to load the cargo and release the cargo through the matrix, which, in our case, is the substrate.

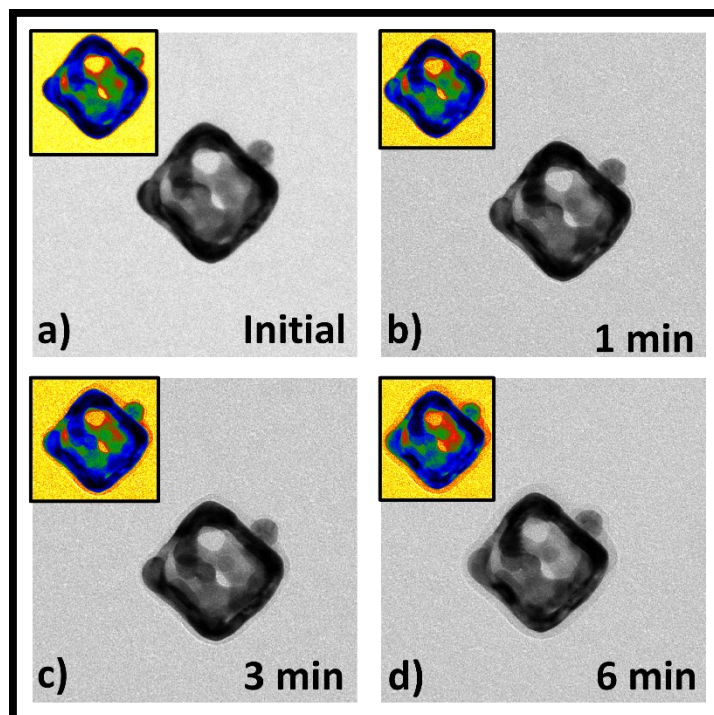


Figure 4.19 Bright-field images for a small hollow-MNP with 1-OpCo. The hollow nanoparticle is exposed to the e-beam (a), the temperature increases, and the cargo is then released through the open corner at 1 min (b). The cargo covers the particle at 3 min (c) to expand at 6 min (d). The inserts show a contrast-colored image that differentiates the cargo release (red color) from the hollow-MNP (blue color).

There is no difference between an open corner and a pore formed in a hollow particle in physical terms. Both should be able to allow the entrance of small molecules such as 1-tetradecanol. However, chemically they have differences. During the synthesis and formation of AgNCs and hollow-MNPs, the PVP plays an important role. PVP binds preferentially to the facets (100) of both particles rather than the corners (111) of these nanostructures. I hypothesize that with the presence of PVP in the facets of the hollow-MNPs, this molecule could block a load of cargo, as shown in large hollow-MNPs. To test this hypothesis, I performed a STEM-EELS analysis to monitor the presence of carbon from the PVP in the hollow-MNPs.

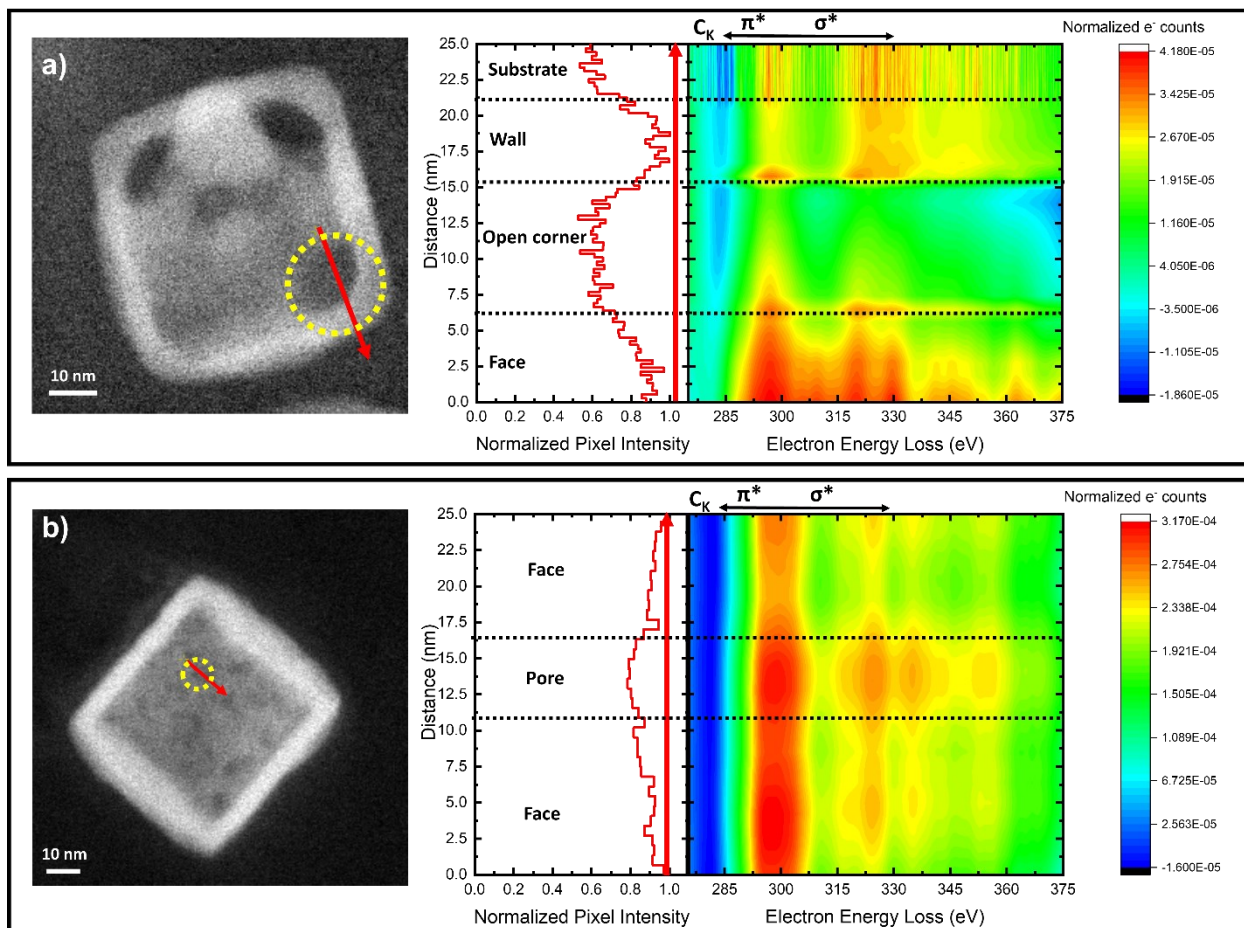


Figure 4.20 HAADF images and STEM-EELS analysis for small (a) and large (b) hollow-MNPs. The red arrow indicates the order of the line scan of the analysis. The histograms (middle) and contour maps (right images) are represented by the initial and final distances analyzed in the line scan. The contour maps exhibit the characteristic energy loss values for carbon. The yellow dotted-circles indicate the sub-particle morphology analyzed during the data acquisition.

Figure 4.20 shows the STEM and EELS analysis of the sub-particle morphologies for small and large hollow-MNPs. The open corner for the small particle (Figure 4.20a) is analyzed by performing the line scan across it for the STEM-EELS analysis. The histogram shows the carbon distribution at different positions along the arrow marked in this nanoparticle: the face, an open corner with ~9.5 nm in diameter, a wall with ~6 nm thickness, and the substrate. The carbon signals correspond to the higher energy molecular orbital for antibonding molecular orbital for the carbon hybridizations sp^3 and

sp², both presented in the PVP molecule. The signal's intensities are particularly strong along the face, wall, and substrate compared to the open corner. In the open corner, the carbon signal is in the borders of the face and wall of the hollow-MNP. The size of this sub-particle morphology is larger enough to avoid the full coverage of PVP.

For smaller sub-particle morphologies such as the pores, the PVP covers the feature totally, as is shown in Figure 4.20b. The STEM-EELS analysis was performed only in the particle's face to have a better resolution of the sub-particle morphologies presented in this type of hollow-MNPs. The pore diameter in this nanoparticle is around ~5 nm, and the carbon signal is present completely in all the pore's diameter and on the particle's face. This information provides new insight into how the PVP locates in this sub-particle feature and the effect on the cargo's releasing observed in the bright-field images. However, the cargo's loading process occurs in the liquid phase, and PVP is expanded through the whole particle. The effect of PVP during cargo release is different from the cargo loading process because both processes occur in different phases. In the solid phase, the cargo release occurs, while in the liquid phase, the loading process is performed.

To understand and prove the hypothesis made through the observations of the PVP presence on hollow-MNPs, I decided to perform an *ex-situ* experiment for the nanoparticles that did not have any cargo release. In this case, the solution of hollow-MNPs was heated at 80°C for 4 h. With these conditions, I could induce the cargo release in the liquid phase as shown in Figure 4.21. This experiment will compare the role of PVP in cargo release for both the liquid and solid phases.

Figure 4.21 shows the bright-field images of the three different large hollow-MNPs that did not have any release in the previous experiments. The sub-particle morphologies analyzed were half void, a full void, and a full void with pores. The solution containing these hollow-MNPs was heated, and then part of this solution was placed into the TEM grid. Here, we can observe how all of the three hollow particles released cargo.

This experiment shows that the non-cargo release observed during the in-situ experiments was due to PVP's blockage to the small sub-particle morphologies that these particles present.

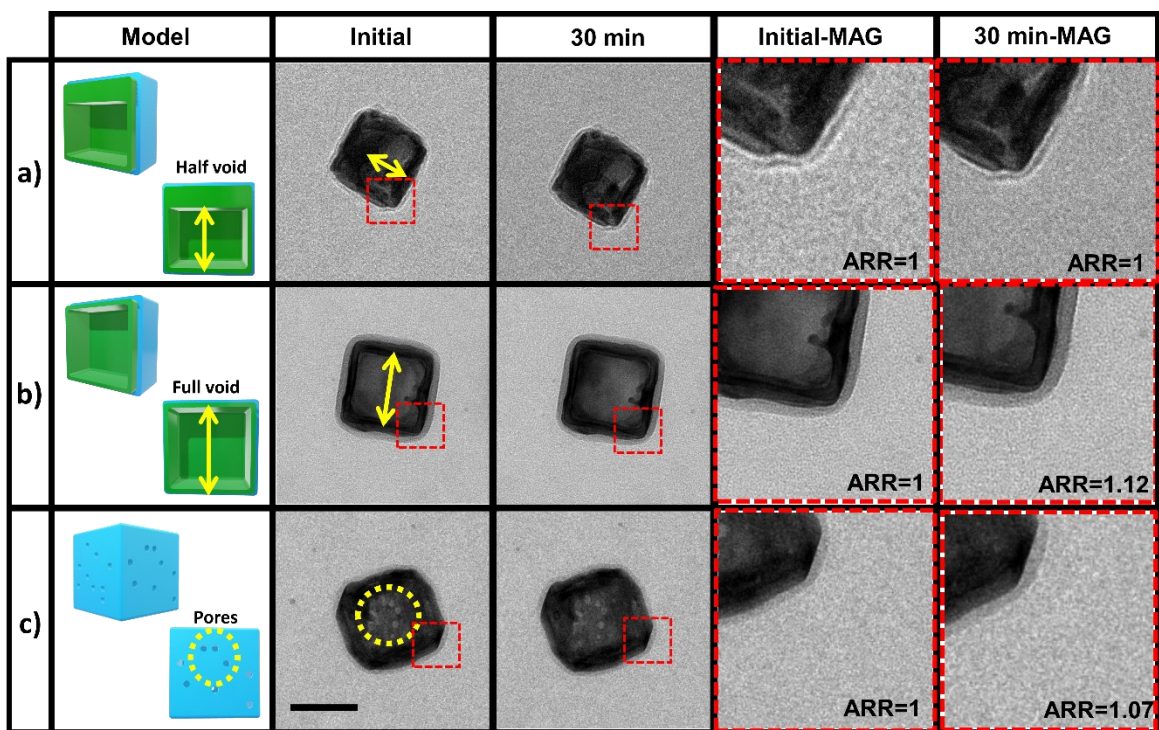


Figure 4.21 Bright-field images for different sub-particles morphologies for cargo release of large hollow-MNPs in an *ex-situ* experiment for the initial release after 4 h of heating and 30 min after the contact with the e-beam. The right images represent the magnification of the corresponding bright-field images. The comparison is made for the observable sub-particle morphologies in the structure for (a) half void, (b) full void, and (c) pores. The scale bar is 50 nm.

Also, I irradiated the particles for 30 min to compare the behavior of the cargo. We can observe that there is no visible change in the cargo release after 30 min. To increase the level of detection, I analyzed the bright-field images with the Matlab code to obtain the ARR value at the beginning and after 30 min of e-beam irradiation. The ARR values do not show any important variation, indicating that it was the maximum cargo that large hollow-MNPs could release in the *ex-situ* experiment.

During the cargo's loading process, 1-tetradecanol (cargo) acts as the matrix in which hollow-MNPs are embedded. In this process, the hollow-MNPs and the cargo are heated at 80°C. It has been found that PVP in alcohol/water mixtures possess a structure of "ideal chain" when it is heated at 40°C. [190] This chain-structural behavior of PVP may allow the transfer of the alcoholic matrix (1-tetradecanol) to the inside of the hollow

nanoparticles. Then, when the nanoparticles are isolated and cooled, the cargo inside of these nanoparticles remains. PVP's different structures in water/alcohol solvents such as coil, globule, and chain overpass the 45 nm. [191]

However, in the solid phase, when the nanoparticles are deposited and analyzed in the TEM microscope, the PVP collapses due to the system's high pressure. This behavior was previously observed in Figure 4.20, where the PVP blocks the small sub-particle features such as pores. This is the reason that I could not observe a cargo release in large hollow-MNPs. As PVP is conformed in a different structure (chain) in the liquid phase, it makes the pores open, allowing the release of the cargo. Figure 4.22 shows a schematic representation of the cargo release for small and large hollow-MNPs in the solid and liquid phases.

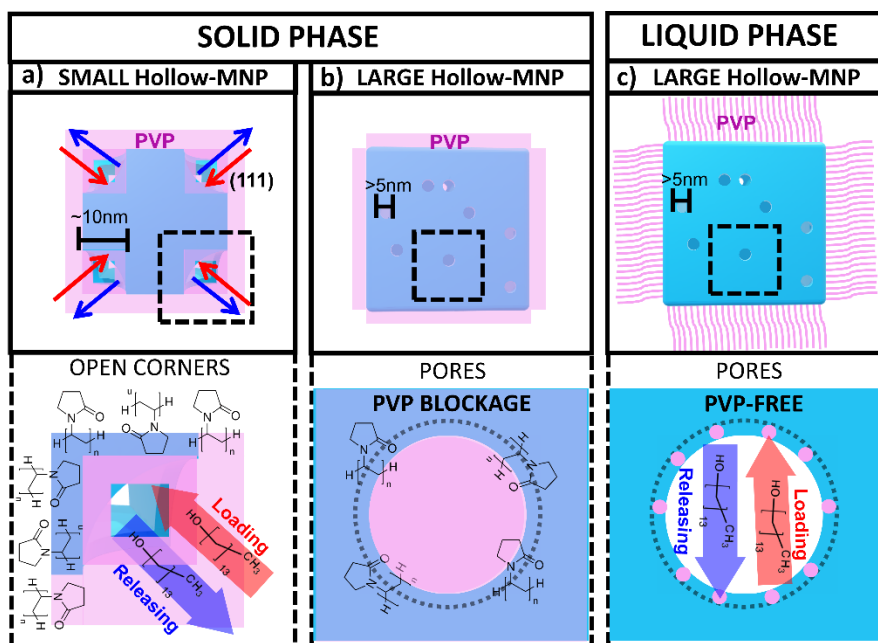


Figure 4.22 Schematic representation of the cargo release process for small (a) and large (b) hollow-MNPs in the solid phase and large (c) hollow-MNPs in the liquid phase. For small hollow-MNP, the PVP does not cover the open corners allowing the cargo loading and release in both phases. Large hollow-MNP have a blockage of pores caused by the collapse of PVP, and it cannot release any cargo. When large hollow-MNPs are in a hot liquid phase, the PVP does not cover the pores and allows the cargo release. The cargo loading process is presented in all the structures because it takes place in the liquid phase, where PVP is not blocking any sub-particle morphology.

4.3.3 Structural characterization of large hollow-MNPs (modified particle)

To compare small and large sizes on the cargo's release, I synthesized a modified large template with similar sub-particle morphologies in small hollow-MNPs. With the knowledge obtained with large and small particles' observations, I decided to synthesize large hollow-MNPs with open corners, avoiding half-void structures.

Figure 4.23 shows the bright-field TEM images of the modified version of large hollow-MNPs after their contact with the cargo. For the 1-OpCo (Figure 4.23a), it is possible to observe that the cargo release is constant for 15 min and 30 min. The release increases by increasing the number of open corners. This behavior can be seen in 3-OpCo and 4-OpCo that release a much larger cargo quantity than 1-OpCo. This observation agrees with the one made for small hollow-MNPs for 3-OpCo and 4-OpCo (Figure 4.15).

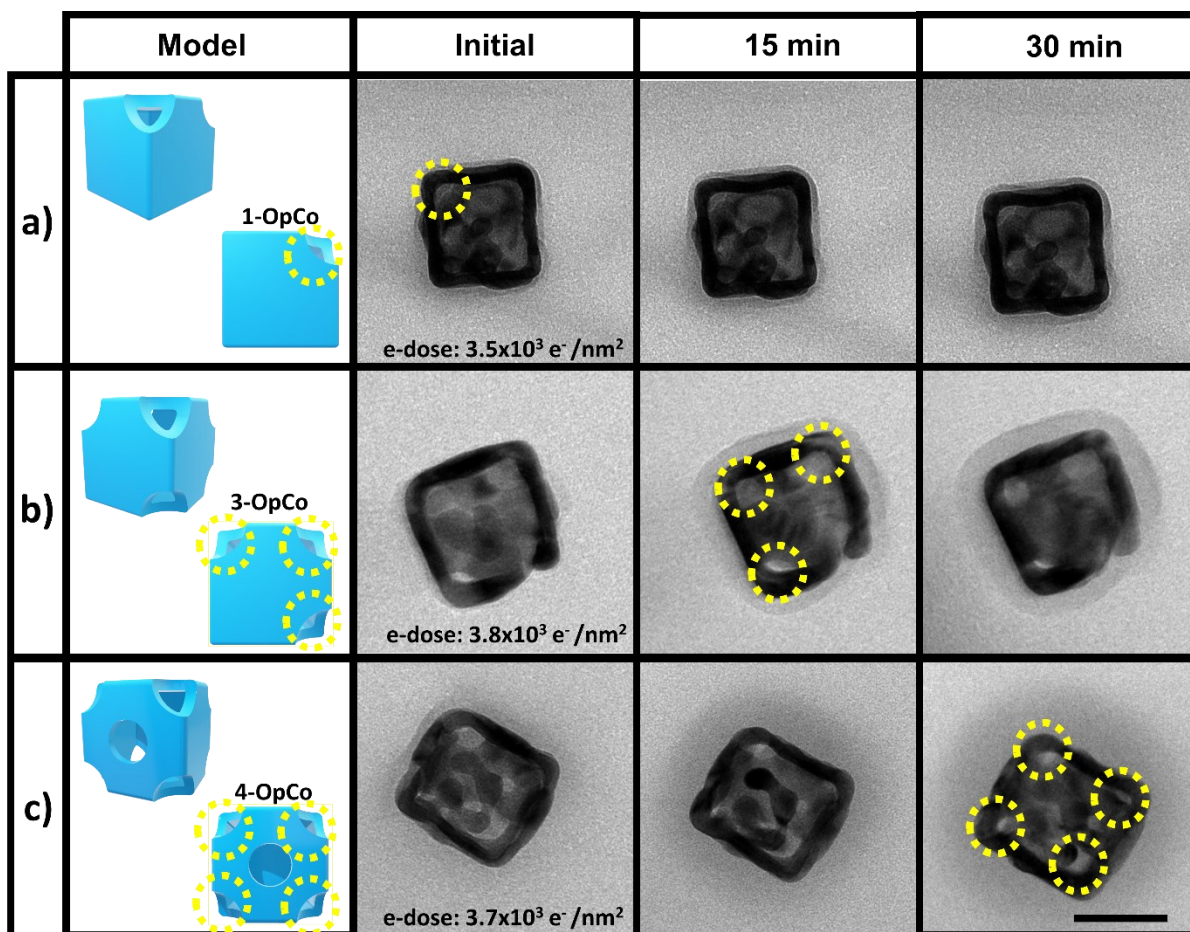


Figure 4.23 Bright-field images for different sub-particles morphologies for modified large hollow-MNPs with a cargo loading process. The comparison is made for the observable sub-particle morphologies in the structure for (a) 1-OpCo, (b) 3-OpCo, (c), and 4-OpCo. The scale bar is 50 nm.

The comparison with the particles that were not exposed to the cargo loading process is shown in Figure 4.24. This figure shows that the large hollow-MNPs did not have any modification during the e-beam irradiation for 30 min. As shown in small hollow-MNPs, large hollow-MNPs for 1-OpCo and 4-OpCo (Figure 4.23a and c) initial release a bit of cargo when they are exposed to the e-beam. It is possible to confirm that this observation is related to the cargo release because the particles that were not exposed to the loading process do not show this behavior.

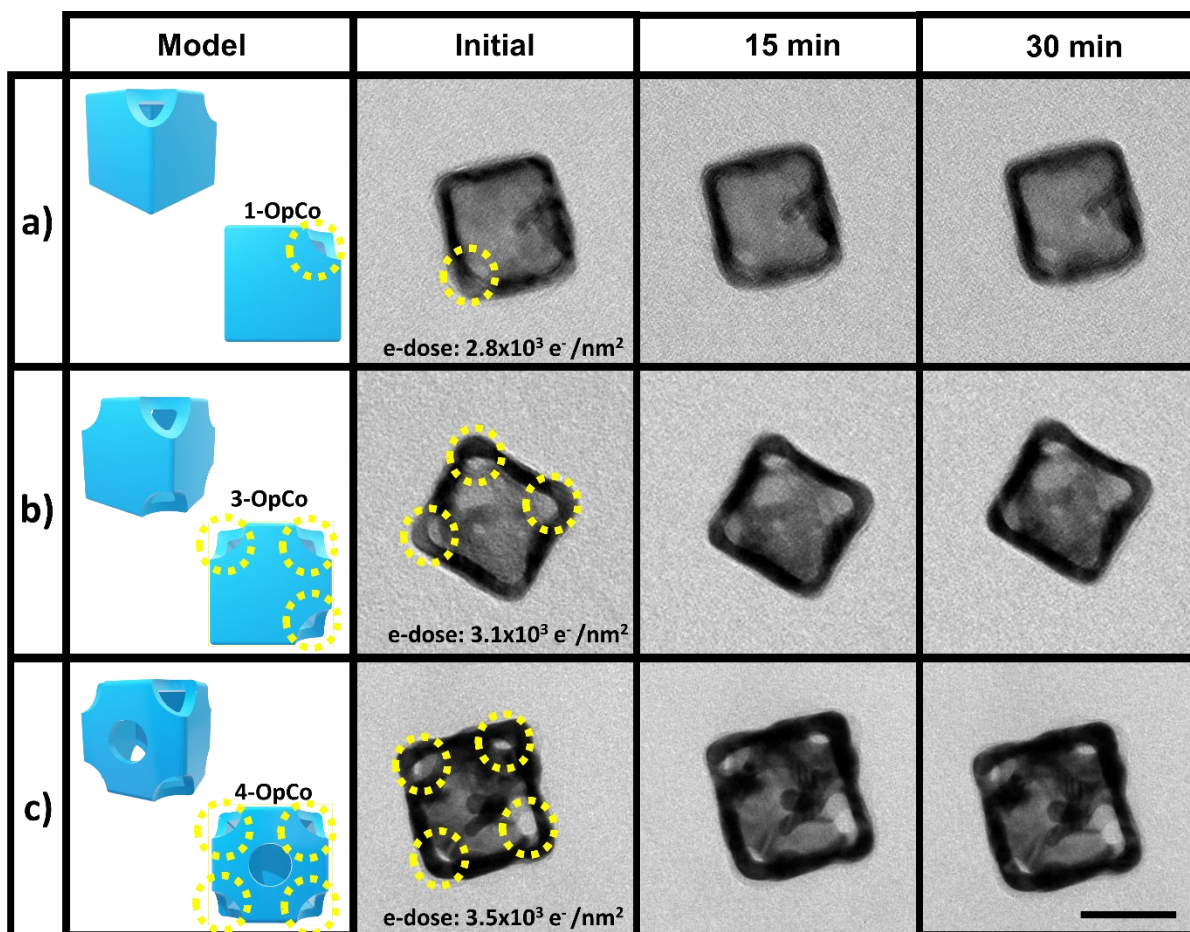


Figure 4.24 Bright-field images for different sub-particles morphologies for the modified large hollow-MNPs without a cargo loading process. The comparison is made for the observable sub-particle morphologies in the structure for (a) 1-OpCo, (b) 3-OpCo, (c), and 4-OpCo. The scale bar is 50 nm.

4.4 Cargo delivery quantification for small and large hollow-MNPs

4.4.1 Small hollow-MNPs cargo delivery

To quantify the cargo release from hollow-MNPs, I analyzed the bright-field images through a custom algorithm that quantifies the pixels that cover the particles plus the cargo. Technically, the algorithm quantifies the "darker" pixels based on a threshold that was selected for each stack of images, and the threshold was constant for every stack. Figure 4.25 shows the cargo release from small hollow-MNPs with different sub-particle features at different times. It is shown that the increment of open corners increases the

area covered by the released cargo. The particle with four open corners shows a larger release at 30 min than the other sub-particle morphologies.

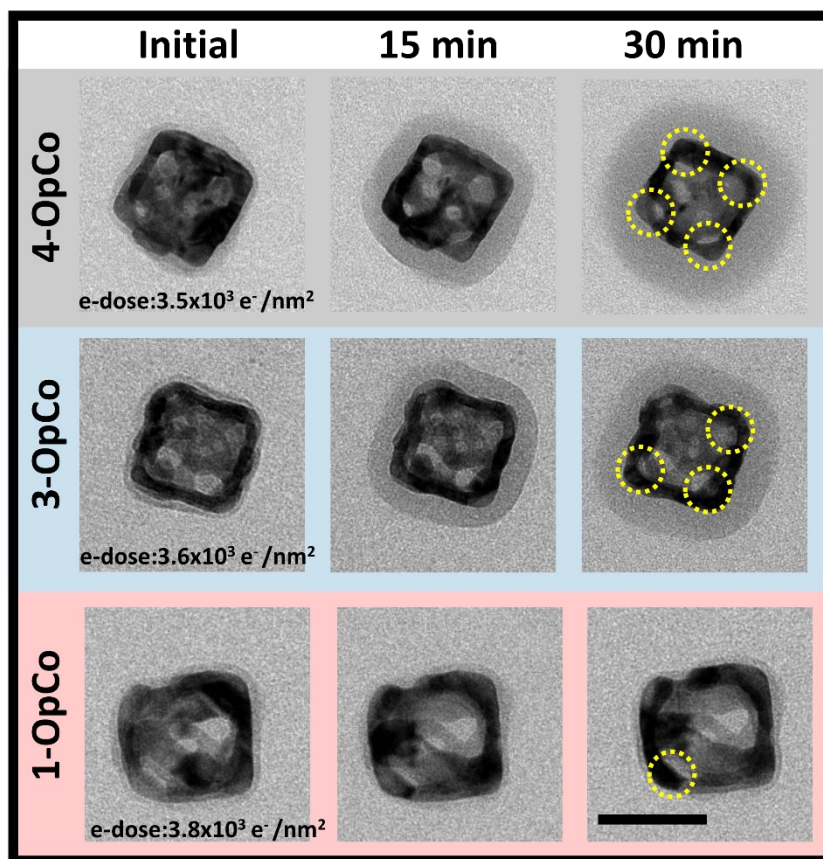


Figure 4.25 Bright-field images for characteristic small hollow-MNPs analyzed based on their number of open corners. The yellow circles identify the open corners for every category. The scale bar is 50 nm.

The quantification of the cargo release is shown in Figure 4.26. The statistical analyses made for each stack of bright-field images prove that the increment of open corners increases the area covered by the cargo release.

The sub-particle morphology with four open corners also delivers more cargo release compared to the others. The 4-OpCo hollow-MNP has a mean ARR=1.6. This value means that the cargo release has an area of 0.6 compared to 1.0, representing the nanoparticle's area. ARR values decrease by decreasing the number of open corners. The 3-OpCo possesses an ARR of 1.2, having a cargo release three times smaller than 4-OpCo. The hollow-MNP with the less open corners (1-OpCo) has a mean ARR value

of 1.03, which is relatively smaller than the rest. These experiments show how the sub-particle features are affecting the release profiles of the nanoparticles.

The difference in the ARR values could be explained by the loading process observed in section 4.3.1. The open corners aid in the increment of the cargo that is loaded into the hollow nanoparticle. The much is loaded, the higher is the release.

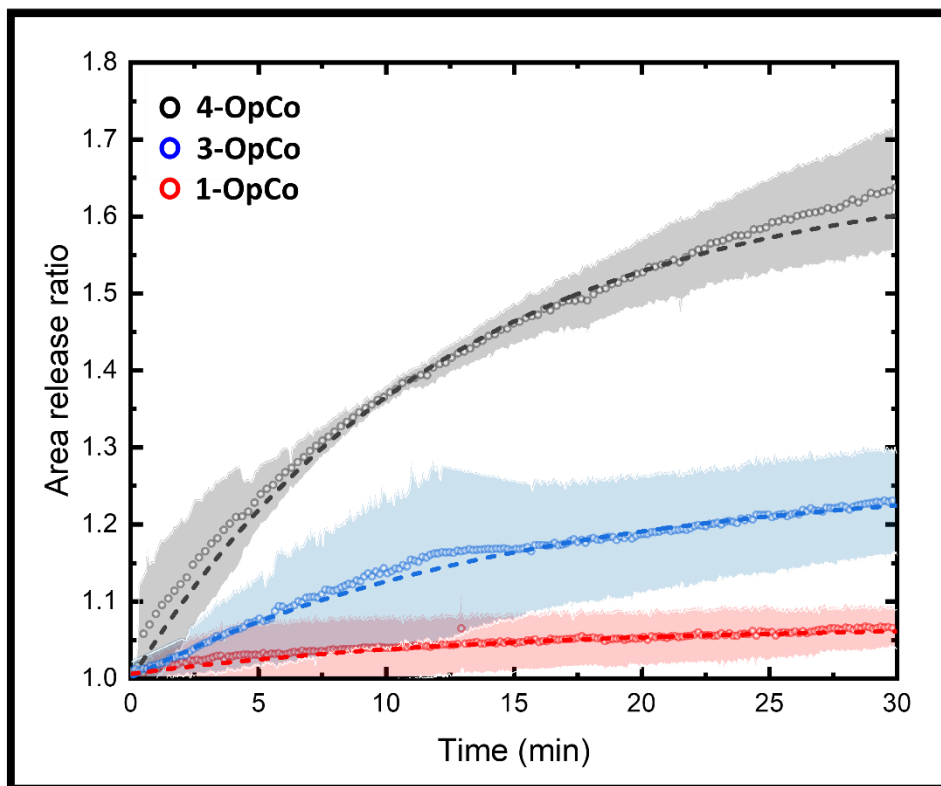


Figure 4.26 Area release ratio (ARR) analyses for the three different categories of small hollow-MNPs. The statistical values were obtained from four to eight analyzed particles per category. The circles represent the data obtained from the code, and the dash lines correspond to the fitting through exponential decay for every category. The standard deviation is represented as a shaded area in black for 4-OpCo, blue for 3-OpCo, and red for 1-OpCo.

I hypothesize that the open corners are the sub-particle morphology that dominates the mechanism of loading and releasing the cargo for small hollow-MNPs. As open corners are not directly affected by PVP, open corners influence the releasing mechanism. If the number of open corners increases, the ARR will be increased.

However, in every category of open corners, there are variations in the ARR values. The upper and lower values for the tendency lines in Figure 4.26 are the standard deviation of the ARRs values found in the multiple particle analyses. At the beginning of the release, the difference is smaller than the release time of 30 min. This difference could be attributed to another sub-particle morphology, the pinholes.

In contrast to open corners, pinholes could appear during the GRR in different sizes and numbers in the hollow cube's facets. Different pinholes appear in the different OpCo categories. The PVP presence on these pinholes will affect the release depending on their sizes. This cargo release variation can be observed in Figure 4.27.

Figure 4.27 shows the bright-field images of small hollow-MNPs with 4-OpCo that have variations on their pinholes. For Figure 4.27a, we can observe different types of pinholes on the facet of the cubes. The one with a higher number of pinholes has a slightly higher ARR value than the nanoparticle with a big-defined pinhole, as shown in Figure 4.27b. Besides, the pinholes shown in Figure 4.27a are larger than 5 nm. With the information obtained before regarding the size of sub-particle morphologies (e.g., pores), the PVP will not cover those pinholes (Section 4.3-Cargo release of hollow-MNPs, translating in larger cargo storage with a larger release than the one with a defined pinhole).

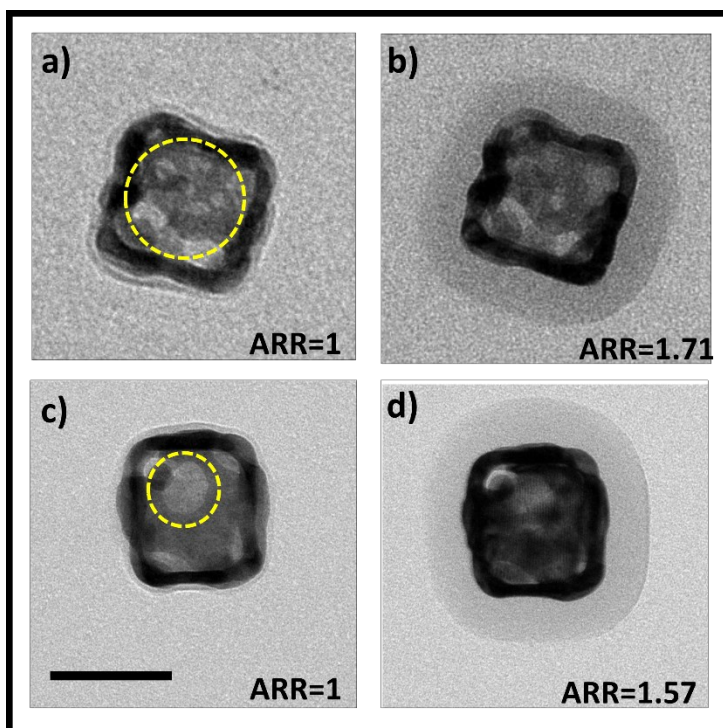


Figure 4.27 Bright-field images for small hollow-MNPs with 4-OpCo with multiple small pinholes (a) and large well-defined (c) pinhole on their structure. After 30 min, the particle with multiple pinholes (b) released more cargo than its counterpart (d). The yellow circles identify the pinholes for every particle. Scale bar in (c) is 50 nm.

4.4.2 Large hollow-MNPs cargo delivery (modified particle)

Large hollow-MNPs exhibit similar behavior to small hollow-MNPs for every category. Figure 4.28 shows the bright-field images of large hollow-MNPs with similar sub-particle features to smaller particles. For all the morphologies, it is shown that the cargo release is enhanced by increasing e-beam exposure time. However, as observed for small hollow-MNPs, the four open corners feature a higher amount of cargo release than the other sub-particle features.

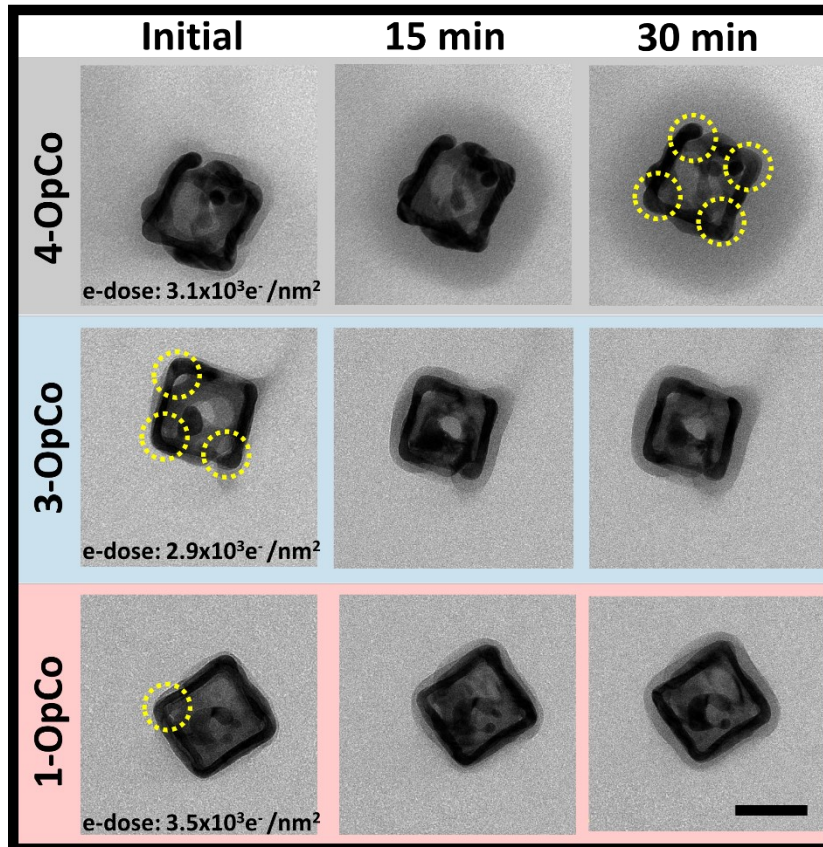


Figure 4.28 Bright-field images for a representative large (modified) hollow-MNPs analyzed based on their number of open corners. The yellow circles identify the open corners for every category. The scale bar is 50 nm.

Figure 4.29 shows the ARR's values plotted as a function of time for different open corners in single particles. The large particle with the highest number of open corners has a mean ARR of 2.0, indicating that the total area (hollow-MNPs+Cargo) becomes twice the initial area (hollow-MNP). The ARR's values drop drastically with a decreasing number of open corners. The release behavior for the four open corners is also different from the rest. The release is much faster in the first 5 min. Then between 5 and 15 min, the release is slower to then stabilize after this time. Figure 4.30 shows the bright-field images of the cargo release for a large hollow-MNPs with 4-OpCo.

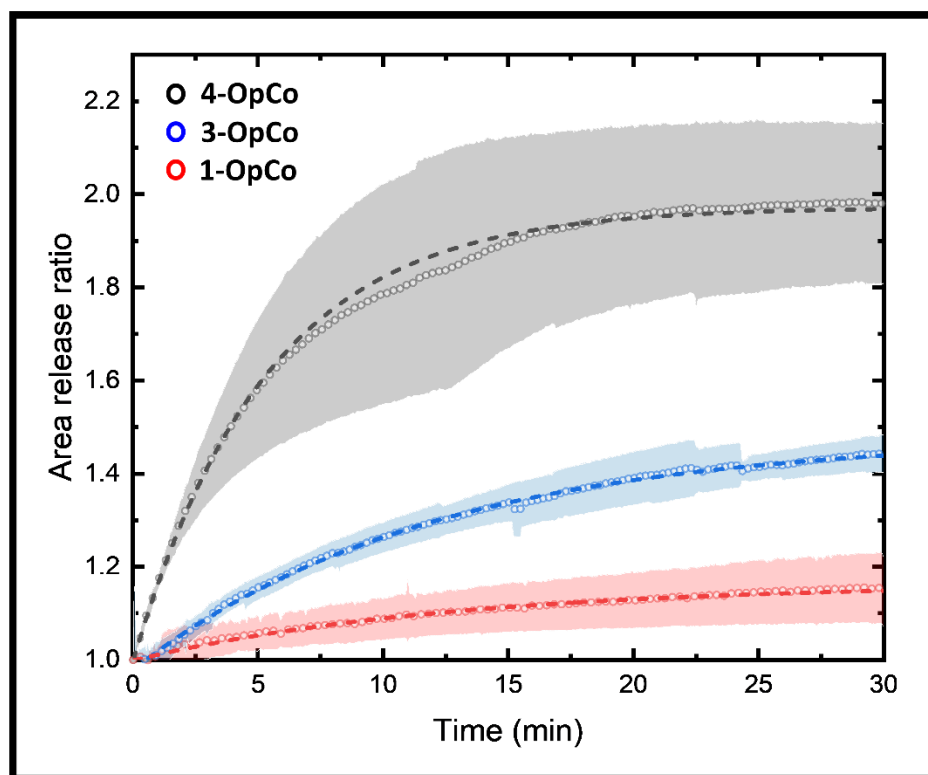


Figure 4.29 Area release ratio (ARR) analyses for the three different categories of large hollow-MNPs. The statistical values were obtained from five to ten analyzed particles per category. The circles represent the data obtained from the code, and the dash lines correspond to the fitting through exponential decay for every category. The standard deviation is represented as a shaded area in black for 4-OpCo, blue for 3-OpCo, and red for 1-OpCo.

The 3-OpCo category has an ARR=1.43 at 30 min, about half of the release shown for 4-OpCo. The 1-OpCo reaches an ARR of 1.15, being much smaller than the rest. The saturation starts at the beginning of the release for 1-OpCo. For 3-OpCo and 4-OpCo, reaching saturation takes a longer time than 1-OpCo.

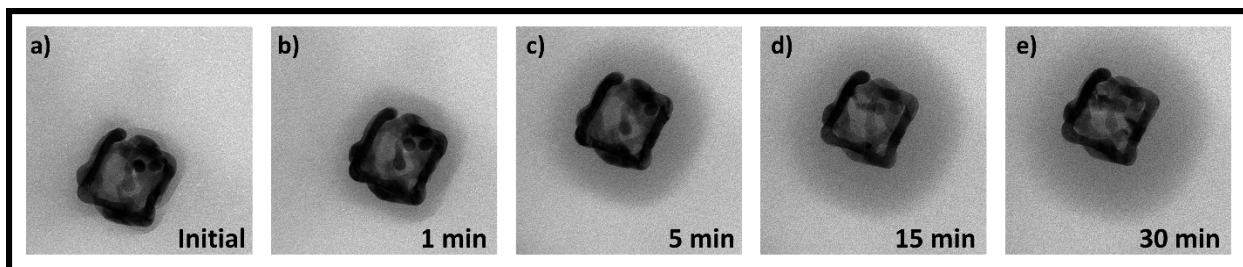


Figure 4.30 Bright-field images for the cargo release from a large hollow-MNP with 4-OpCo. The particle releases the cargo immediately (a). The release increases at 1 min (b) and 5 min (c). The area covered by the cargo release stabilizes at 15 min (d), similar to the release at 30 min (e).

Nevertheless, 4-OpCo exhibits a large standard deviation of cargo release. Figure 4.31 shows the difference in cargo release of large hollow-MNPs with 4-OpCo but different pinholes. In the image, we can observe the difference in the size of pinholes in both nanostructures. For the particle with the larger pinhole (Figure 4.31a, b), the ARR is 2.3 and for its counterpart, which has a smaller pinhole, the ARR is 1.95. In this case, the size of the pinhole is affecting the cargo release mechanism.

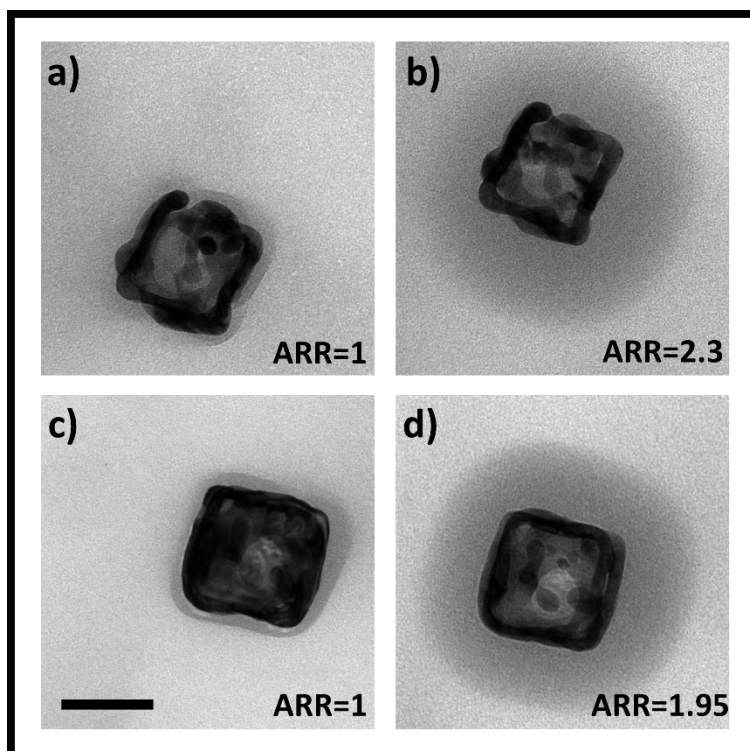


Figure 4.31 Bright-field images for large hollow-MNPs with 4-OpCo with a large (a) and small (c) pinhole on their structure. After 30 min, the large pinhole (b) released more cargo than its counterpart (d). Scale bar in (c) is 50 nm.

The observation of how the rest of the sub-particle morphologies (pinholes) affects the cargo release, apart from open corners, agrees with the hypothesis made in the small hollow-MNPs discussion where different sub-particle morphologies large enough (such as open corners) may influence the cargo delivery as well. Figure 4.32 shows the STEM-EELS characterization for large hollow-MNPs and their corresponding sub-particle morphologies.

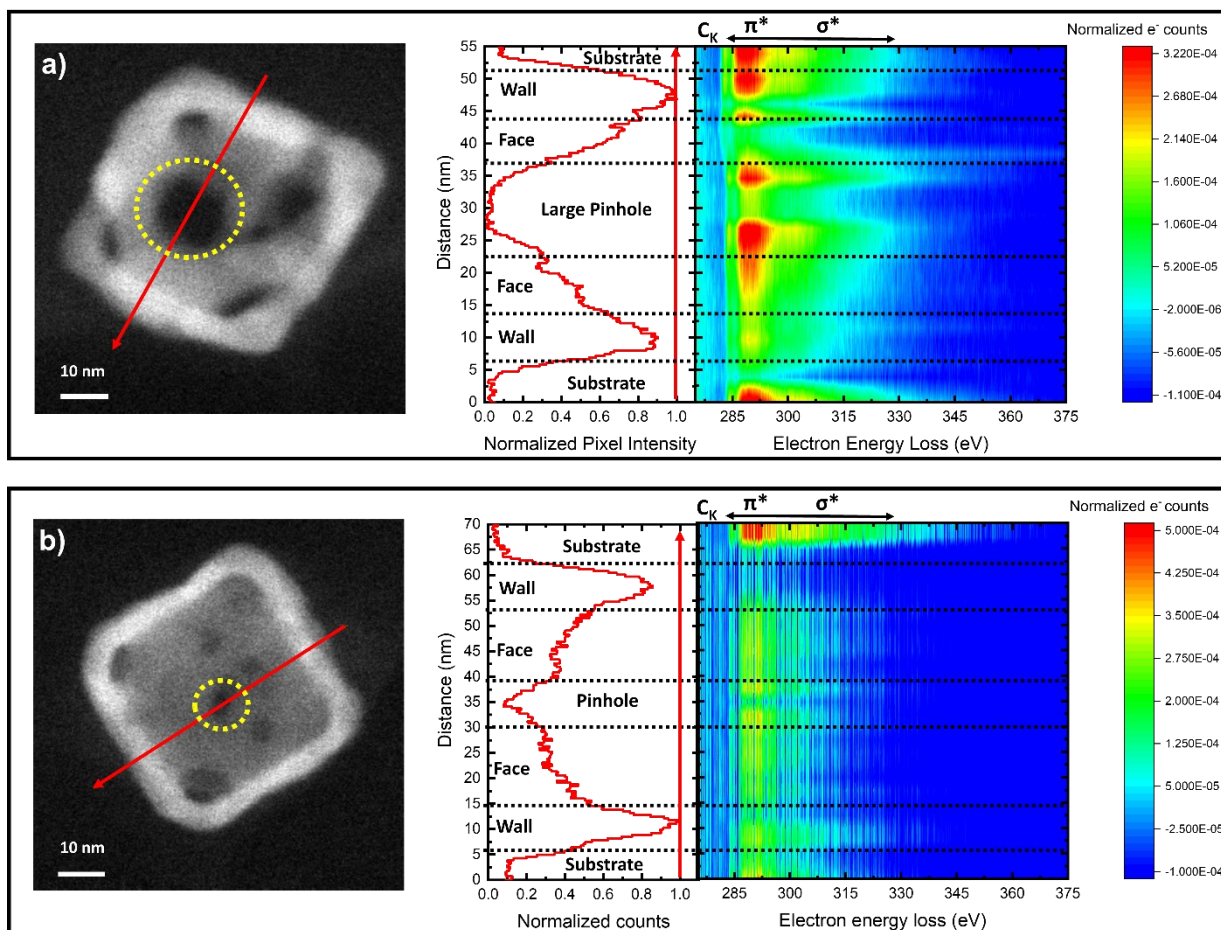


Figure 4.32 HAADF images and STEM-EELS analysis for large (a) and small (b) pinhole for the large hollow-MNPs. The red arrow indicates the order of the line scan of the analysis. The histograms and contour maps (right images) are represented by the initial and final distances analyzed in the line scan. The contour maps exhibit the characteristic energy loss values for carbon. The yellow dotted circles indicate the sub-particle morphology analyzed during the data acquisition.

Figure 4.32 compares the presence of PVP in pinholes with different diameters. For the larger pinhole, with 15 nm of diameter (Figure 4.32a), we can observe that the carbon signal is stronger in the sub-particle morphology edges, as shown in open corners for small hollow-MNPs. The signal decreases to nearly zero in the center of the pinhole; this means that the PVP presence in this part of the sub-particle morphology is considerably lower than the edges. As in open corners, this absence of PVP could make that pinhole serves as another way of loading and releasing cargo. However, PVP was found present

on smaller pinholes. This phenomenon is presented in Figure 4.32b, where the pinhole's diameter is smaller than the one in Figure 4.32a. These pinholes are identified in the yellow-dotted circles. However, the carbon signal's presence is much higher, and it is almost distributed in all the pinhole area, with stronger intensities at the borders of the sub-particle morphology.

The pinhole's diameter and distribution on the hollow-MNPs will affect the loading and releasing of the cargo. If the pinholes are small, PVP will allow less cargo loading; thus, the open corners will govern the loading and releasing mechanism. However, if the pinholes are large, PVP's effect will be minimized. The loading mechanism will be enhanced, releasing more cargo faster because of the combination of open corners and pinholes. The small pores presented in the non-modified large hollow-MNPs support this hypothesis.

In the HAADF images, shown in Figure 4.32, it is possible to observe the variation in the pinhole's diameter and number in two different hollow-MNPs. Control over the pinhole's diameter and size is more difficult than other sub-particle morphologies while developing the larger particles' in the GRR. This lack of control means that the particles with the 4-OpCo will present larger variations of pinholes. These findings explain the observations made in Figure 4.29 and Figure 4.31. Figure 4.33 summarizes the findings and observations made for large hollow-MNPs.

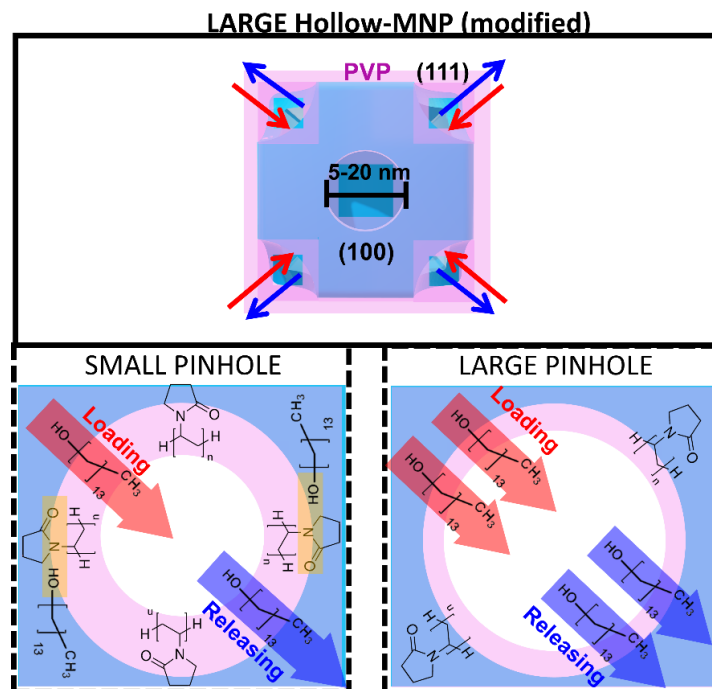


Figure 4.33 Schematic representation of the cargo release and loading mechanisms in large (modified) hollow-MNP. Small pinholes will have a higher effect of PVP on the mechanisms due to hydrogen bonds and steric hindrance. This phenomenon is minimized in larger pinholes causing a major effect on cargo loading and releasing, such as the open corners.

4.4.3 The area release rate for hollow-MNPs

Section 4.3 discussed the different delivery profiles (represented by ARR values) for different categories of hollow-MNPs. The ARR values visualize the cargo release profiles by considering the final area concerning the initial area. Herein, I further perform a derivative of those values and compare the behavior of different sub-particle morphologies of hollow-MNPs prepared from small and large templates. Figure 4.34 compares the normalized area release rates at different times for small and large hollow-MNPs. This figure shows that for the 1-OpCo and 3-OpCo, the small and larger particles have a similar tendency in cargo release. In contrast, for 4-OpCo, the larger particles have significantly faster cargo release at the beginning.

Besides, large hollow-MNPs with 4-OpCo finish the cargo release at 25 min, indicating no more cargo to release. In contrast, the rest of the particles, including smaller ones,

continue to release cargo at 30 min. As discussed in section 4.4.2, the cargo release of large hollow-MNPs with 4-OpCo is also affected by the pinholes on their structure. The combination of these sub-particle features with the open corners enhances the cargo release at a faster rate.

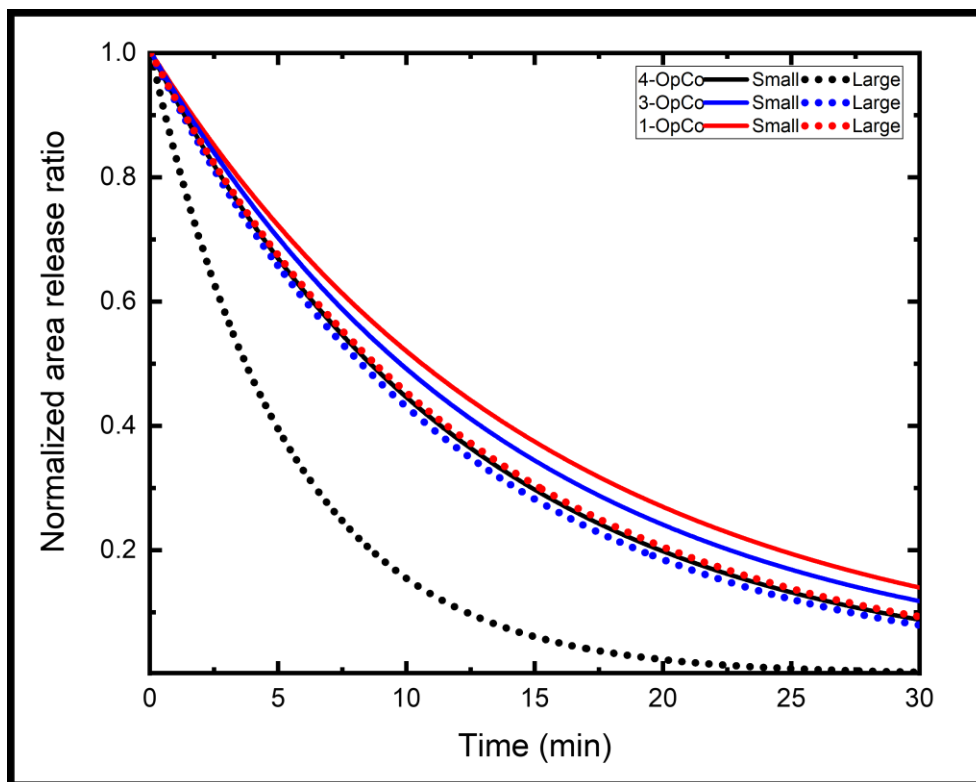


Figure 4.34 Comparison of the normalized area release rates for small (line) and large (dotted line) hollow-MNPs for 30 min.

Since I provide new insights and observations on the cargo release of different types of hollow nanoparticles, these findings can help researchers engineer different types of particles depending on their use, combining their sub-particle features by releasing more or less cargo in a faster or slower way.

4.4.4 Effect of substrate on cargo release

In TEM experiments, not only is the specimen irradiated with the e-beam, but the substrate is also interacting with the beam and could affect the thermal properties of the sample. To observe the substrate's effect on the cargo release, I compared two different

materials, an insulator, represented by SiO, and a good thermal conductor, the graphene (Gf).

In our experiments, the substrate plays an important role in the cargo release mechanisms. Its function is to increase the system's local temperature (hollow-MNP+cargo). Figure 4.35 shows the comparison of ARR values of a large hollow-MNP (3-OpCo) on different substrates. The cargo release is three times higher on the SiO substrate compared to graphene material at 30 min.

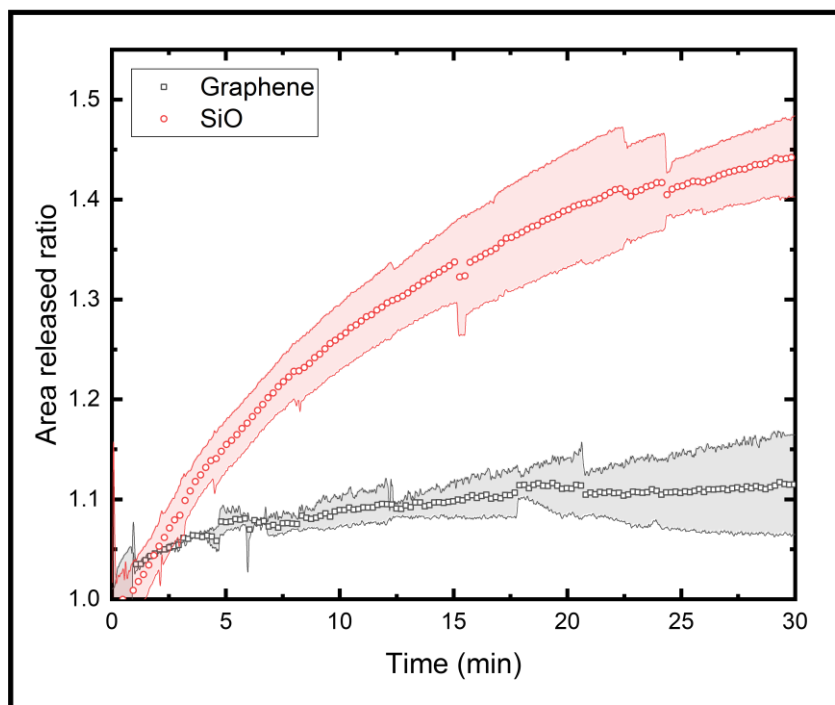


Figure 4.35 Area release ratio comparison for 3-OpCo using SiO (red) and graphene (black).

Once the particle is irradiated with the e-beam, the interaction with the e-beam will cause a rise in the local temperature of the system. [174, 175] The cargo is then melted in this fashion; it can flow through the substrate due to its higher temperature (above 40 °C). However, if the substrate is a good thermal conductor, such as graphene, the heat will be dissipated faster. The local temperature will then be confined in a much smaller area, preventing the cargo from flowing through the substrate.

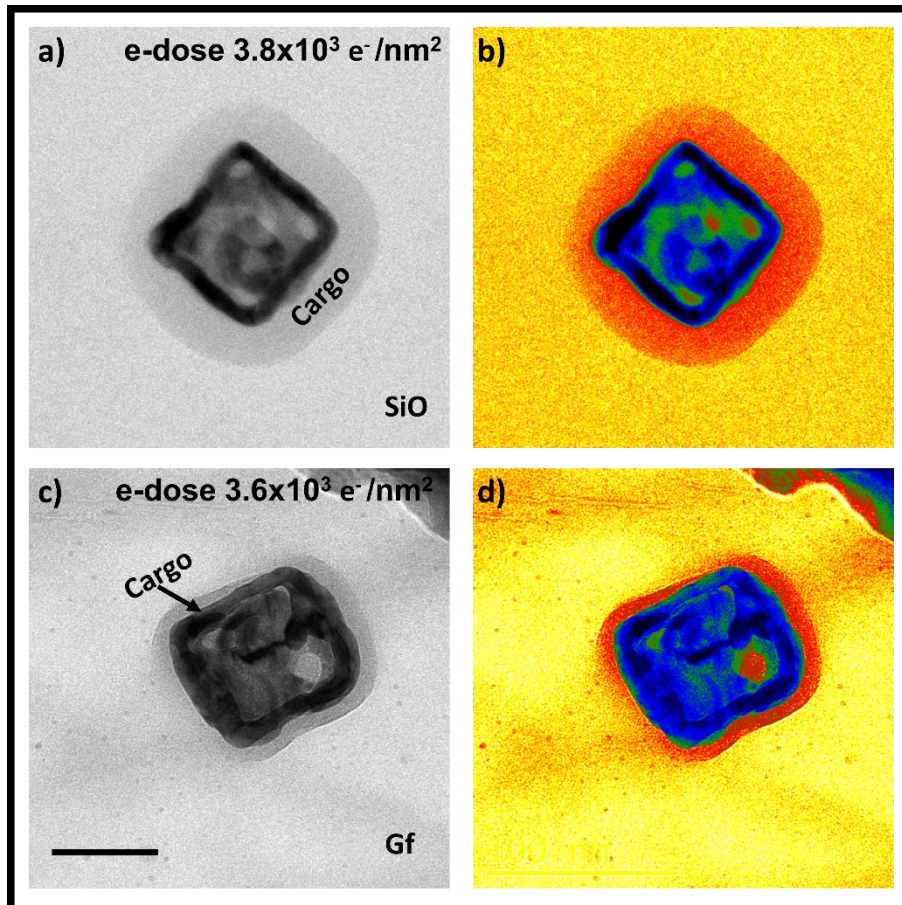


Figure 4.36 Bright-field images of the cargo release for a 3-OpCo hollow-MNPs on SiO (a) and graphene (c) at 30 min; the right images are the contrast-colored bright-field images for SiO (b) and graphene (d). Scale bar in (c) is 50 nm. Notice that the graphene substrate can be folded due to its thickness, and hollow-MNP will be tilted. The sub-particle features will not appear as flat substrates.

As seen in section 1.4.2-Thermodynamics of heating through electron-matter interaction using a TEM and Figure 1.10, a thermionic source (LaB₆) like in the substrate comparison experiments increases the ΔT in the experiments with low thermal conductivity.

The ΔT estimation from Figure 1.10 provides a better insight into how these materials behave under e-beam irradiation. Materials with high thermal conductivity (Au and graphene) do not contribute to local temperature increment as materials with lower

thermal conductivity (SiO and tetradecanol). With this information, I can infer that the interaction of tetradecanol with the e-beam will increase this material's temperature above its melting point. In graphene experiments, as graphene does not contribute to the ΔT , the substrate dissipates heat having a cold surface where the tetradecanol cannot flow. In SiO experiments, the substrate could be above the melting point of tetradecanol, allowing this material to flow over the surface.

From a different perspective, these results can be applied as a physical way of mapping the temperatures caused by the external energy sources' interaction (such as e-beam and lasers) with the specimens depending on the substrate. Using different PCM materials with higher melting points could detect temperature with higher precision (between the melting points range). These experiments will also provide information on the range in which the temperature will be increased by the electron-matter interaction and the optimal substrate to avoid or increase the local temperature.

5 CONCLUSIONS

5.1 Structural analysis of hollow-MNPs

This thesis has addressed the structural studies of hollow-MNPs and the effects of sub-particle features on the optical properties and cargo release studies. Through experimental studies, I characterized the galvanic replacement reaction's intermediate steps that transform AgNCs into hollow-MNPs. I observed that hollow-MNPs follow different morphological development during the GRR, determined by the initial template's size.

Smaller AgNCs templates begin with a half-void development. As the GRR continues, other sub-particle morphology development appears, such as the full development of the void in all the structure and then the pinhole's appearance, and then the corners' modification and aperture. Similarly, larger AgNCs showed void-like structures, but the last sub-particle morphologies in the GRRs created small pores on hollow cubes' facets. I attribute these structural differences to changes in the dominant diffusion mechanism for nanoparticles with different surface-to-volume ratios.

The sub-particle morphologies formed for the different templates had a major effect on the plasmonic resonances and, hence, on the nanoparticles' optical absorption. Through optical characterization, I could observe that every structure has an absorption in a specific wavelength. These absorptions are the LSPR, which are characteristic for every particle depending on the sub-particle morphology. However, void-like structures shown different modes. Through computational analysis, I could explain that the phenomena presented in void-like structures are due to the hybridization of the plasmonic modes and their interaction with the outer surfaces of the hollow-MNPs.

Also, computational analysis shows that the characteristic LSPR absorptions from optical analysis agree with those obtained by electromagnetic simulations. However, the difference is attributed to different sub-particle morphologies in the hollow-MNPs, causing a broadened LSPR peak. The values obtained are in the range of the FWHM width of the experimental analysis.

5.2 Cargo delivery of hollow-MNPs

The hollow-MNPs obtained through the GRR were used for cargo delivery studies. I observed that the different sub-particle morphologies presented in the hollow-MNPs directly affect the cargo's loading and release.

Smaller hollow-MNPs showed that a higher number of open corners increases the cargo release of the structures. Large hollow-MNPs do not release in any structure, including the one with pores in the facet. The absence of cargo release was due to the presence of PVP on sub-particle morphologies. I observed that in the solid phase (TEM experiments), PVP accumulates on the borders of the sub-particle features causing the structure's block and impeding the cargo release. However, via *ex-situ* experiments, I observed that when the particles are heated in the liquid phase, they have cargo release. This information confirms that tiny sub-particle features such as small pores can load and release cargo but in the liquid phase, where the morphology of PVP molecules appears differently from that in the solid phase. Larger hollow-MNPs with open corners also have the same tendency of cargo release as small hollow-MNPs.

The quantification of the release *via* automatized code demonstrated that by increasing the number of open corners on the hollow structures, the cargo release increases. However, in all these cases, there were certain variations on the release. Specifically, 4-OpCo in large hollow-MNPs showed a large standard deviation compared to the rest of the particles, including small hollow-MNPs. This phenomenon is explained by the presence of pinholes on hollow-MNPs. For small hollow-MNPs, the variation is due to the number of pinholes shown on their structure. Large particles evidenced that the variation is larger if the pinhole diameter increases, and this is due to the interaction of PVP with the rest of the sub-particle morphologies. If the pinhole is large, the effect of PVP will be less strong, contributing to an increase in the cargo loading and, by consequence, an increase in the release.

The e-beam interaction with the hollow-MNPs and their use as nanocarriers evidenced the importance of electron-matter studies to evaluate different mechanisms. Specifically, in our methodology, I could elucidate that the temperature rises above 40 °C because this is the melting point of our PCM material (cargo).

Besides, I evaluated the effect on the cargo release of hollow-MNPs by comparing two different substrates. The insulator substrate, represented by SiO₂, shows a larger cargo release than the one with a higher thermal conductivity, graphene. This cargo release difference suggests that insulator substrates will significantly affect local temperature increment than conductive substrates. However, our findings address the importance of the different studies that can be made in electron microscopy. The interaction of the e-beam with the specimen will cause an increment in the temperature of the system. Thus, the observation of the different mechanisms by this characterization technique needs to consider this factor.

5.3 Perspectives

In this thesis, I observed the steps involved in the formation of hollow-MNPs during the GRR. These findings are of greater importance because they allow a new path to study the sub-particle morphologies and their effect on different properties. Besides, these studies can be generalized to different systems that have varying sub-particle morphologies. The advantage of our work is providing studies at the single nanoparticle level. Specifically, areas such as catalysis, sensing, and optics could use our technique to address different challenges on their applications in the plasmonic field.

5.3.1 Structural studies of hollow-MNPs

I synthesized different hollow-MNPs for small and larger templates, and I analyzed their structures *ex-situ* via electron microscopy. A new approach, such as *in-situ* analysis, could provide more information about the intermediate structures developed during the GRR for single nanoparticles. Liquid-cell studies in TEM are a technique capable of analyzing chemical reactions and acquiring images simultaneously. The examples of the new information that could be obtained are:

- Sub-particle morphology evolution with time in single nanoparticles.
- Initial conversion and the subsequent corners' modification during GRR.
- Pinhole formation and modification and comparison with other sub-particle morphologies.

- *In-situ* atomic diffusion observation *via* elemental mapping.

5.3.2 Dynamics studies of single hollow-MNPs

The use of UEM as a characterization and measure technique can provide new insights into the dynamics of these nanoparticles. Specifically, the studies of thermal properties could complement our findings. The absorption and dissipation of heat are of great importance and could explain the initial states in how the nanoparticles could behave when they are irradiated with an external source. However, these studies must be done with sources (e.g., lasers) apart from the e-beam. In UEM, the e-beam is necessary to observe the processes that occur in nanoparticles. Even though photons are used to irradiate hollow-MNPs, observing the dynamics of the heat processes' mechanisms via UEM could help understand these nanoparticles' behavior during the temperature changes.

These studies could be divided into two sections:

- Ultrafast studies of hollow-MNPs with femto/pico lasers *via* UEM.
 - This study will help in the comprehension of the absorption mechanism involved in the metallic nanoparticles.
 - The dissipation mechanisms could be addressed here by studying the interaction between the hollow-MNP and the substrate or matrix.

Both studies can be correlated and complemented to the cargo delivery application.

5.3.3 Cryo-TEM studies of single hollow-MNPs

In theory, using a cryo technique could make the nanoparticle in a basal state, where the interaction of the temperature with the e-beam will be minimized. Thus, external sources such as lasers to irradiate the nanoparticles can be studied as the only energy interaction source with the specimen.

5.3.4 Nanothermometer development

Hollow-MNPs serve as a host in which different materials can be stored inside of their structure. In this thesis, I used a PCM material that has a melting point of 40°C. New synthesis methods for loading different cargos (PCM materials) inside hollow-MNPs with different melting points could help study the mechanisms driven by varying temperature ranges when the nanoparticles are exposed to an e-beam in TEM.

The different melting points of the PCM materials could provide a range in which the temperature is located. For instance, hollow-MNPs are synthesized with two different PCM as cargos, which have melting points of 40°C and 100°C, respectively. When the hollow-MNPs are exposed to the e-beam, if only one PCM (with a 40°C melting point) is released, it means that the system's local temperature will be higher than 40°C but less than 100°C. Then, loading another PCM material with a melting point less than 100°C and repeating the same experiment will reduce the range of the temperature to be found.

5.3.5 Cargo delivery studies

Similar to structural studies, using a liquid-cell holder in TEM could open many possibilities to study the mechanisms that I observed but in the liquid phase. This approach will help to correlate our findings with those obtained in the liquid phase. The studies that this approach could address are :

- Studies of the presence of PVP in the sub-particle morphologies in hollow-MNPs
 - The structure of PVP is different in liquid than in the solid phase. Thus, studies in the liquid phase could provide the formation of this material's interaction to explain cargo delivery and the cargo loading mechanisms.
- *In-situ* studies in liquid-cell holder for the cargo loading mechanisms in hollow-MNPs
- Cargo delivery applications
 - In this study, the parameters and environment in which nanocarriers are exposed to biological media for delivery applications could be simulated in liquid-phase TEM studies. For instance, it is possible to prepare a serum

that simulates many species in blood, to observe the behavior of hollow-MNPs in these conditions.

- Also, the correlation of studies between liquid and solid phases could be made, and it could be of great importance for scientists involved in these applications. Liquid-cell TEM holders are expensive. Understanding both phases and their correlation is crucial to help scientists choose which approach is better to understand the different mechanisms.

6 REFERENCES

- [1] J. K. Patra *et al.*, “Nano based drug delivery systems: Recent developments and future prospects 10 Technology 1007 Nanotechnology 03 Chemical Sciences 0306 Physical Chemistry (incl. Structural) 03 Chemical Sciences 0303 Macromolecular and Materials Chemistry 11 Medical and Health Sciences 1115 Pharmacology and Pharmaceutical Sciences 09 Engineering 0903 Biomedical Engineering Prof Ueli Aebi, Prof Peter Gehr,” *Journal of Nanobiotechnology*, vol. 16, no. 1. BioMed Central Ltd., Sep. 19, 2018, doi: 10.1186/s12951-018-0392-8.
- [2] G. Yang, S. Chen, and J. Zhang, “Bioinspired and Biomimetic Nanotherapies for the Treatment of Infectious Diseases,” *Front. Pharmacol.*, vol. 10, p. 751, Jul. 2019, doi: 10.3389/fphar.2019.00751.
- [3] S. Tran, P.-J. DeGiovanni, B. Piel, and P. Rai, “Cancer nanomedicine: a review of recent success in drug delivery,” *Clin. Transl. Med.*, vol. 6, no. 1, p. 44, Dec. 2017, doi: 10.1186/s40169-017-0175-0.
- [4] A. Chowdhury, S. Kunjiappan, T. Panneerselvam, B. Somasundaram, and C. Bhattacharjee, “Nanotechnology and nanocarrier-based approaches on treatment of degenerative diseases,” *Int. Nano Lett.*, vol. 7, no. 2, pp. 91–122, Jun. 2017, doi: 10.1007/s40089-017-0208-0.
- [5] B. Fortuni *et al.*, “Polymeric Engineering of Nanoparticles for Highly Efficient Multifunctional Drug Delivery Systems,” *Sci. Rep.*, vol. 9, no. 1, pp. 1–13, Dec. 2019, doi: 10.1038/s41598-019-39107-3.
- [6] E. B. Manaia, M. P. Abuçafy, B. G. Chiari-Andréo, B. L. Silva, J. A. Oshiro Junior, and L. A. Chiavacci, “Physicochemical characterization of drug nanocarriers,” *International Journal of Nanomedicine*, vol. 12. Dove Medical Press Ltd., pp. 4991–5011, Jul. 13, 2017, doi: 10.2147/IJN.S133832.
- [7] Q. Liu, J. Guan, L. Qin, X. Zhang, and S. Mao, “Physicochemical properties affecting the fate of nanoparticles in pulmonary drug delivery,” *Drug Discovery Today*, vol. 25, no. 1. Elsevier Ltd, pp. 150–159, Jan. 01, 2020, doi: 10.1016/j.drudis.2019.09.023.
- [8] I. J. Macha *et al.*, “Drug Delivery From Polymer-Based Nanopharmaceuticals—An Experimental Study Complemented by Simulations of Selected Diffusion Processes,”

- Front. Bioeng. Biotechnol.*, vol. 7, no. MAR, p. 37, Mar. 2019, doi: 10.3389/fbioe.2019.00037.
- [9] S. Chen *et al.*, "Inorganic nanomaterials as carriers for drug delivery," *Journal of Biomedical Nanotechnology*, vol. 12, no. 1. American Scientific Publishers, pp. 1–27, Jan. 01, 2016, doi: 10.1166/jbn.2016.2122.
- [10] J. H. Lee and Y. Yeo, "Controlled drug release from pharmaceutical nanocarriers," *Chem. Eng. Sci.*, vol. 125, pp. 75–84, Mar. 2015, doi: 10.1016/j.ces.2014.08.046.
- [11] A. Khalid *et al.*, "Strategies for improving drug delivery: nanocarriers and microenvironmental priming," *Expert Opinion on Drug Delivery*, vol. 14, no. 7. Taylor and Francis Ltd, pp. 865–877, Jul. 03, 2017, doi: 10.1080/17425247.2017.1243527.
- [12] F. U. Din *et al.*, "Effective use of nanocarriers as drug delivery systems for the treatment of selected tumors," *International Journal of Nanomedicine*, vol. 12. Dove Medical Press Ltd., pp. 7291–7309, Oct. 05, 2017, doi: 10.2147/IJN.S146315.
- [13] S. D. Anderson, V. V. Gwenin, and C. D. Gwenin, "Magnetic Functionalized Nanoparticles for Biomedical, Drug Delivery and Imaging Applications," *Nanoscale Research Letters*, vol. 14. Springer New York LLC, 2019, doi: 10.1186/s11671-019-3019-6.
- [14] S. Thambiraj, S. Hema, and D. Ravi Shankaran, "Functionalized gold nanoparticles for drug delivery applications," in *Materials Today: Proceedings*, Jan. 2018, vol. 5, no. 8, pp. 16763–16773, doi: 10.1016/j.matpr.2018.06.030.
- [15] S. W. Choi, W. S. Kim, and J. H. Kim, "Surface-functionalized nanoparticles for controlled drug delivery.,," *Methods Mol. Biol.*, vol. 303, pp. 121–131, 2005, doi: 10.1385/1-59259-901-x:121.
- [16] K. A. Howard and D. Peer, "Providing the full picture: A mandate for standardizing nanoparticle-based drug delivery," *Nanomedicine*, vol. 8, no. 7. Future Medicine Ltd., pp. 1031–1033, Jun. 25, 2013, doi: 10.2217/nnm.13.95.
- [17] G. Canavese *et al.*, "Nanoparticle-assisted ultrasound: A special focus on sonodynamic therapy against cancer," *Chem. Eng. J.*, vol. 340, pp. 155–172, May 2018, doi: 10.1016/j.cej.2018.01.060.
- [18] Q.-L. Zhou, Z.-Y. Chen, Y.-X. Wang, F. Yang, Y. Lin, and Y.-Y. Liao, "Ultrasound-Mediated Local Drug and Gene Delivery Using Nanocarriers," *Biomed Res. Int.*, vol. 2014, 2014, doi: 10.1155/2014/963891.

- [19] P. Tharkar, R. Varanasi, W. S. F. Wong, C. T. Jin, and W. Chrzanowski, "Nano-Enhanced Drug Delivery and Therapeutic Ultrasound for Cancer Treatment and Beyond," *Frontiers in Bioengineering and Biotechnology*, vol. 7. Frontiers Media S.A., Nov. 22, 2019, doi: 10.3389/fbioe.2019.00324.
- [20] J. Liu *et al.*, "Heat-triggered drug release systems based on mesoporous silica nanoparticles filled with a maghemite core and phase-change molecules as gatekeepers," *J. Mater. Chem. B*, vol. 2, no. 1, pp. 59–70, Jan. 2014, doi: 10.1039/c3tb21229g.
- [21] E. G. Fuller *et al.*, "Externally Triggered Heat and Drug Release from Magnetically Controlled Nanocarriers," *ACS Appl. Polym. Mater.*, vol. 1, no. 2, pp. 211–220, Feb. 2019, doi: 10.1021/acsapm.8b00100.
- [22] E. Guisasola, A. Baeza, L. Asín, J. M. de la Fuente, and M. Vallet-Regí, "Heating at the Nanoscale through Drug-Delivery Devices: Fabrication and Synergic Effects in Cancer Treatment with Nanoparticles," *Small Methods*, vol. 2, no. 9, p. 1800007, Sep. 2018, doi: 10.1002/smt.201800007.
- [23] P. M. Price, W. E. Mahmoud, A. A. Al-Ghamdi, and L. M. Bronstein, "Magnetic drug delivery: Where the field is going," *Frontiers in Chemistry*, vol. 6, no. DEC. Frontiers Media S.A., 2018, doi: 10.3389/fchem.2018.00619.
- [24] A. Raza, U. Hayat, T. Rasheed, M. Bilal, and H. M. N. Iqbal, "'smart' materials-based near-infrared light-responsive drug delivery systems for cancer treatment: A review," *Journal of Materials Research and Technology*, vol. 8, no. 1. Elsevier Editora Ltda, pp. 1497–1509, Jan. 01, 2019, doi: 10.1016/j.jmrt.2018.03.007.
- [25] A. M. Goodman *et al.*, "Near-infrared remotely triggered drug-release strategies for cancer treatment," *Proc. Natl. Acad. Sci. U. S. A.*, vol. 114, no. 47, pp. 12419–12424, Nov. 2017, doi: 10.1073/pnas.1713137114.
- [26] E. C. Dreaden, L. A. Austin, M. A. MacKey, and M. A. El-Sayed, "Size matters: Gold nanoparticles in targeted cancer drug delivery," *Therapeutic Delivery*, vol. 3, no. 4. NIH Public Access, pp. 457–478, Apr. 2012, doi: 10.4155/tde.12.21.
- [27] K. O. Shittu, M. T. Bankole, A. S. Abdulkareem, O. K. Abubakre, and A. U. Ubaka, "Application of gold nanoparticles for improved drug efficiency," *Adv. Nat. Sci. Nanosci. Nanotechnol.*, vol. 8, no. 3, p. 035014, Jul. 2017, doi: 10.1088/2043-6254/AA7716.
- [28] M. U. Farooq *et al.*, "Gold Nanoparticles-enabled Efficient Dual Delivery of Anticancer

- Therapeutics to HeLa Cells,” *Sci. Rep.*, vol. 8, no. 1, pp. 1–12, Dec. 2018, doi: 10.1038/s41598-018-21331-y.
- [29] P. Ma *et al.*, “Inorganic nanocarriers for platinum drug delivery,” *Materials Today*, vol. 18, no. 10. Elsevier, pp. 554–564, Dec. 01, 2015, doi: 10.1016/j.mattod.2015.05.017.
- [30] R. Liang, M. Wei, D. G. Evans, and X. Duan, “Inorganic nanomaterials for bioimaging, targeted drug delivery and therapeutics,” *Chem. Commun.*, vol. 50, no. 91, pp. 14071–14081, Nov. 2014, doi: 10.1039/c4cc03118k.
- [31] C. Xiong, W. Lu, M. Zhou, X. Wen, and C. Li, “Cisplatin-loaded hollow gold nanoparticles for laser-triggered release,” *Cancer Nanotechnol.*, vol. 9, no. 1, Dec. 2018, doi: 10.1186/s12645-018-0041-9.
- [32] J. You, G. Zhang, and C. Li, “Exceptionally high payload of doxorubicin in hollow gold nanospheres for near-infrared light-triggered drug release,” in *ACS Nano*, Feb. 2010, vol. 4, no. 2, pp. 1033–1041, doi: 10.1021/nn901181c.
- [33] R. T. Hill, “Plasmonic biosensors.,” *Wiley Interdiscip. Rev. Nanomed. Nanobiotechnol.*, vol. 7, no. 2, pp. 152–68, 2015, doi: 10.1002/wnan.1314.
- [34] H. A. Atwater and A. Polman, “Plasmonics for improved photovoltaic devices,” *Nat. Mater.*, vol. 9, no. 3, pp. 205–213, Mar. 2010, doi: 10.1038/nmat2629.
- [35] J. Zeng, Q. Zhang, J. Chen, and Y. Xia, “A Comparison Study of the Catalytic Properties of Au-Based Nanocages, Nanoboxes, and Nanoparticles,” 2010, doi: 10.1021/nl903062e.
- [36] X. Zhang, S. Wang, Y. Liu, L. Li, and C. Sun, “Catalytic enhancement of gold nanocages induced by undercoordination-charge-polarization,” *APL Mater.*, vol. 5, no. 5, p. 053501, May 2017, doi: 10.1063/1.4978041.
- [37] D. Manzoor, S. Krishnamurty, and S. Pal, “Endohedrally doped gold nanocages: efficient catalysts for O₂ activation and CO oxidation,” *Phys. Chem. Chem. Phys.*, vol. 18, no. 10, pp. 7068–7074, Mar. 2016, doi: 10.1039/C5CP05624A.
- [38] A. Genç *et al.*, “Tuning the Plasmonic Response up: Hollow Cuboid Metal Nanostructures,” *ACS Photonics*, vol. 3, no. 5, pp. 770–779, May 2016, doi: 10.1021/acsphotonics.5b00667.
- [39] R. Weissleder, “A clearer vision for in vivo imaging,” *Nat. Biotechnol.*, vol. 19, no. 4, pp. 316–317, Apr. 2001, doi: 10.1038/86684.
- [40] A. M. Smith, M. C. Mancini, and S. Nie, “Second window for in vivo imaging,” *Nat.*

- Nanotechnol.*, vol. 4, no. 11, pp. 710–711, Nov. 2009, doi: 10.1038/nnano.2009.326.
- [41] †,‡ B. Devika Chithrani, †,‡ and Arezou A. Ghazani, and †,‡,§ Warren C. W. Chan*, “Determining the Size and Shape Dependence of Gold Nanoparticle Uptake into Mammalian Cells,” 2006, doi: 10.1021/NL052396O.
- [42] B. Pang, X. Yang, and Y. Xia, “Putting gold nanocages to work for optical imaging, controlled release and cancer theranostics.,” *Nanomedicine (Lond)*., vol. 11, no. 13, pp. 1715–28, 2016, doi: 10.2217/nnm-2016-0109.
- [43] S. Huang *et al.*, “A54 peptide-mediated functionalized gold nanocages for targeted delivery of DOX as a combinational photothermal-chemotherapy for liver cancer.,” *Int. J. Nanomedicine*, vol. 12, pp. 5163–5176, 2017, doi: 10.2147/IJN.S131089.
- [44] S. Jain, D. G. Hirst, and J. M. O’Sullivan, “Gold nanoparticles as novel agents for cancer therapy.,” *Br. J. Radiol.*, vol. 85, no. 1010, pp. 101–13, Feb. 2012, doi: 10.1259/bjr/59448833.
- [45] Z. Zhang *et al.*, “Photothermal gold nanocages filled with temperature sensitive tetradecanol and encapsulated with glutathione responsive polycurcumin for controlled DOX delivery to maximize anti-MDR tumor effects,” *J. Mater. Chem. B*, vol. 5, no. 27, pp. 5464–5472, Jul. 2017, doi: 10.1039/C7TB01253E.
- [46] J. Chen *et al.*, “Gold Nanocages: Bioconjugation and Their Potential Use as Optical Imaging Contrast Agents,” 2005, doi: 10.1021/nl047950t.
- [47] A. G. M. da Silva, T. S. Rodrigues, S. J. Haigh, and P. H. C. Camargo, “Galvanic replacement reaction: recent developments for engineering metal nanostructures towards catalytic applications,” *Chem. Commun.*, vol. 53, no. 53, pp. 7135–7148, Jun. 2017, doi: 10.1039/C7CC02352A.
- [48] S. E. Skrabalak *et al.*, “Gold Nanocages: Synthesis, Properties, and Applications,” *Acc. Chem. Res.*, vol. 41, no. 12, pp. 1587–1595, Dec. 2008, doi: 10.1021/ar800018v.
- [49] S. E. Skrabalak, L. Au, X. Li, and Y. Xia, “Facile synthesis of Ag nanocubes and Au nanocages,” *Nat. Protoc.*, vol. 2, no. 9, pp. 2182–2190, Sep. 2007, doi: 10.1038/nprot.2007.326.
- [50] B. Goris, L. Polavarapu, S. Bals, G. Van Tendeloo, and L. M. Liz-Marzán, “Monitoring Galvanic Replacement Through Three-Dimensional Morphological and Chemical Mapping,” *Nano Lett.*, vol. 14, no. 6, pp. 3220–3226, Jun. 2014, doi: 10.1021/nl500593j.

- [51] L. Au, X. Lu, and Y. Xia, "A Comparative Study of Galvanic Replacement Reactions Involving Ag Nanocubes and AuCl(2) or AuCl(4).," *Adv. Mater.*, vol. 20, no. 13, pp. 2517–2522, 2008, doi: 10.1002/adma.200800255.
- [52] J. Chen, J. M. Mclellan, A. Siekkinen, Y. Xiong, Z.-Y. Li, and Y. Xia, "Facile Synthesis of Gold-Silver Nanocages with Controllable Pores on the Surface," *J. AM. CHEM. SOC.*, vol. 128, pp. 14776–14777, 2006, doi: 10.1021/ja066023g.
- [53] H. Nakajima, "The discovery and acceptance of the Kirkendall Effect: The result of a short research career," *JOM*, vol. 49, no. 6, pp. 15–19, Jun. 1997, doi: 10.1007/BF02914706.
- [54] Y. Yin, R. M. Rioux, C. K. Erdonmez, S. Hughes, G. A. Somorjal, and A. P. Alivisatos, "Formation of Hollow Nanocrystals Through the Nanoscale Kirkendall Effect," *Science (80-.)*, vol. 304, no. 5671, pp. 711–714, 2004, doi: 10.1126/science.1096566.
- [55] S. W. Chee, S. F. Tan, Z. Baraissov, M. Bosman, and U. Mirsaidov, "Direct observation of the nanoscale Kirkendall effect during galvanic replacement reactions," *Nat. Commun.*, vol. 8, no. 1, p. 1224, Dec. 2017, doi: 10.1038/s41467-017-01175-2.
- [56] A. D. S. and E. O. Kirkendall, "A. D. Smigelskas and E. O. Kirkendall, 'Zinc Diffusion in Alpha Brass,' Transactions of AIME, Vol. 171, 1947, pp. 130-142.," *Trans. AIME*, vol. 171, no. 1, pp. 130–142, 1947, doi: 10.1103/PhysRevB.86.014426.
- [57] A. Cabot, M. Ibáñez, P. Guardia, and A. P. Alivisatos, "Reaction Regimes on the Synthesis of Hollow Particles by the Kirkendall Effect," *J. Am. Chem. Soc.*, vol. 131, no. 32, pp. 11326–11328, Aug. 2009, doi: 10.1021/ja903751p.
- [58] A.-A. El Mel, R. Nakamura, and C. Bittencourt, "The Kirkendall effect and nanoscience: hollow nanospheres and nanotubes," *Beilstein J. Nanotechnol.*, vol. 6, pp. 1348–1361, Jun. 2015, doi: 10.3762/bjnano.6.139.
- [59] K.-Y. Niu, J. Park, H. Zheng, and A. P. Alivisatos, "Revealing Bismuth Oxide Hollow Nanoparticle Formation by the Kirkendall Effect," *Nano Lett.*, vol. 13, no. 11, pp. 5715–5719, Nov. 2013, doi: 10.1021/nl4035362.
- [60] G. G. Li, M. Sun, E. Villarreal, S. Pandey, S. R. Phillpot, and H. Wang, "Galvanic Replacement-Driven Transformations of Atomically Intermixed Bimetallic Colloidal Nanocrystals: Effects of Compositional Stoichiometry and Structural Ordering," *Langmuir*, vol. 34, no. 14, pp. 4340–4350, Apr. 2018, doi: 10.1021/acs.langmuir.8b00448.
- [61] D. Thiry *et al.*, "The Kirkendall Effect in Binary Alloys: Trapping Gold in Copper Oxide

- Nanoshells,” *Chem. Mater.*, vol. 27, no. 18, pp. 6374–6384, Sep. 2015, doi: 10.1021/acs.chemmater.5b02391.
- [62] A. Mori, Y. Suzuki, S.-I. Yanagiya, T. Sawada, and K. Ito, “Shrinking stacking fault through glide of the Shockley partial dislocation in hard-sphere crystal under gravity,” *Mol. Phys.*, vol. 105, no. 10, pp. 1377–1383, May 2007, doi: 10.1080/00268970701348725.
- [63] G. E. Murch, A. V. Evteev, E. V. Levchenko, and I. V. Belova, “Recent Progress in the Simulation of Diffusion Associated with Hollow and Bi-Metallic Nanoparticles,” Accessed: Mar. 05, 2018. [Online]. Available: [http://www.qucosa.de/fileadmin/data/qucosa/documents/18982/diff_fund_11\(2009\)42.pdf](http://www.qucosa.de/fileadmin/data/qucosa/documents/18982/diff_fund_11(2009)42.pdf).
- [64] Q. Chen, H. Qi, Y.-T. Ren, J.-P. Sun, and L.-M. Ruan, “Optical properties of truncated Au nanocages with different size and shape,” *AIP Adv.*, vol. 7, no. 6, p. 065115, Jun. 2017, doi: 10.1063/1.4990409.
- [65] L. Graham and J. M. Orenstein, “Processing tissue and cells for transmission electron microscopy in diagnostic pathology and research,” *Nat. Protoc.*, vol. 2, no. 10, pp. 2439–2450, Oct. 2007, doi: 10.1038/nprot.2007.304.
- [66] J. R. McIntosh, “Electron microscopy of cells: A new beginning for a new century,” *Journal of Cell Biology*, vol. 153, no. 6. Rockefeller University Press, p. f25, Jun. 11, 2001, doi: 10.1083/jcb.153.6.F25.
- [67] M. J. Talbot and R. G. White, “Methanol fixation of plant tissue for Scanning Electron Microscopy improves preservation of tissue morphology and dimensions,” *Plant Methods*, vol. 9, no. 1, p. 36, Oct. 2013, doi: 10.1186/1746-4811-9-36.
- [68] N. F. Cheville and J. Stasko, “Techniques in Electron Microscopy of Animal Tissue,” *Vet. Pathol.*, vol. 51, no. 1, pp. 28–41, Jan. 2014, doi: 10.1177/0300985813505114.
- [69] “scanR | Vision and visual servoing for nanomanipulation and nanocharacterization using scanning electron microscope.” <https://scanr.enseignementsup-recherche.gouv.fr/publication/these2013BESA2014> (accessed Apr. 13, 2021).
- [70] M. Winey, J. B. Meehl, E. T. O’Toole, and T. H. Giddings, “Conventional transmission electron microscopy,” *Molecular Biology of the Cell*, vol. 25, no. 3. American Society for Cell Biology, pp. 319–323, Feb. 01, 2014, doi: 10.1091/mbc.E12-12-0863.
- [71] “Transmission Electron Microscopy - an overview | ScienceDirect Topics.” <https://www.sciencedirect.com/topics/materials-science/transmission-electron-microscopy>

(accessed Apr. 13, 2021).

- [72] M. Ohtsuki, M. S. Isaacson, and A. V. Crewe, “Dark field imaging of biological macromolecules with the scanning transmission electron microscope,” *Proc. Natl. Acad. Sci. U. S. A.*, vol. 76, no. 3, pp. 1228–1232, 1979, doi: 10.1073/pnas.76.3.1228.
- [73] A. Ponce, S. Mejía-Rosales, and M. José-Yacamán, “Scanning transmission electron microscopy methods for the analysis of nanoparticles,” *Methods Mol. Biol.*, vol. 906, pp. 453–471, 2012, doi: 10.1007/978-1-61779-953-2_37.
- [74] S. Hettler, M. Dries, P. Hermann, M. Obermair, D. Gerthsen, and M. Malac, “Carbon contamination in scanning transmission electron microscopy and its impact on phase-plate applications,” *Micron*, vol. 96, pp. 38–47, May 2017, doi: 10.1016/j.micron.2017.02.002.
- [75] C. M. McGilvery, A. E. Goode, M. S. P. Shaffer, and D. W. McComb, “Contamination of holey/lacey carbon films in STEM,” *Micron*, vol. 43, no. 2–3, pp. 450–455, Feb. 2012, doi: 10.1016/j.micron.2011.10.026.
- [76] R. Arenal *et al.*, “Spatially-resolved EELS analysis of antibody distribution on biofunctionalized magnetic nanoparticles,” *ACS Nano*, vol. 7, no. 5, pp. 4006–4013, May 2013, doi: 10.1021/nn306028t.
- [77] N. Kapp, D. Studer, P. Gehr, and M. Geiser, “Electron Energy-Loss Spectroscopy as a Tool for Elemental Analysis in Biological Specimens,” in *Methods in molecular biology (Clifton, N.J.)*, vol. 369, Methods Mol Biol, 2007, pp. 431–447.
- [78] F. Hofer, F. P. Schmidt, W. Grogger, and G. Kothleitner, “Fundamentals of electron energy-loss spectroscopy,” in *IOP Conference Series: Materials Science and Engineering*, Feb. 2016, vol. 109, no. 1, p. 012007, doi: 10.1088/1757-899X/109/1/012007.
- [79] K. M. Bataineh, “Developing of an environmental cell TEM holder for dynamic in situ observation,” *Rev. Sci. Instrum.*, vol. 87, no. 2, p. 023705, Feb. 2016, doi: 10.1063/1.4942245.
- [80] Y. Li *et al.*, “Atomic structure of sensitive battery materials and interfaces revealed by cryo-electron microscopy,” *Science (80-.)*, vol. 358, no. 6362, pp. 506–510, Oct. 2017, doi: 10.1126/science.aam6014.
- [81] J. K. SUNDE, S. WENNER, and R. HOLMESTAD, “*In situ* heating TEM observations of evolving nanoscale Al–Mg–Si–Cu precipitates,” *J. Microsc.*, vol. 279, no. 3, pp. 143–147, Sep. 2020, doi: 10.1111/jmi.12845.

- [82] M. Agati, F. Renaud, D. Benoit, and A. Claverie, "In-situ transmission electron microscopy studies of the crystallization of N-doped Ge-rich GeSbTe materials," *MRS Commun.*, vol. 8, no. 3, pp. 1145–1152, Sep. 2018, doi: 10.1557/mrc.2018.168.
- [83] S. Pu, C. Gong, and A. W. Robertson, "Liquid cell transmission electron microscopy and its applications," *Royal Society Open Science*, vol. 7, no. 1. Royal Society Publishing, Jan. 01, 2020, doi: 10.1098/rsos.191204.
- [84] K. Bücker *et al.*, "Ultrafast transmission electron microscopy reveals electron dynamics and trajectories in a thermionic gun setup," in *European Microscopy Congress 2016: Proceedings*, Wiley-VCH Verlag GmbH & Co. KGaA, 2016, pp. 445–446.
- [85] C. W. Barlow Myers, N. J. Pine, and W. A. Bryan, "Femtosecond transmission electron microscopy for nanoscale photonics: A numerical study," *Nanoscale*, vol. 10, no. 44, pp. 20628–20639, Nov. 2018, doi: 10.1039/c8nr06235h.
- [86] N. Jiang, "Beam damage by the induced electric field in transmission electron microscopy," *Micron*, vol. 83, pp. 79–92, Apr. 2016, doi: 10.1016/j.micron.2016.02.007.
- [87] N. Jiang, "Electron beam damage in oxides: A review," *Reports on Progress in Physics*, vol. 79, no. 1. Institute of Physics Publishing, p. 016501, Dec. 18, 2015, doi: 10.1088/0034-4885/79/1/016501.
- [88] S. Li, J. Zhong, Z. Cui, Q. Zhang, M. Sun, and Y. Wang, "Electron beam-induced morphology transformations of Fe₂TiO₅ nanoparticles," *J. Mater. Chem. C*, vol. 7, no. 44, pp. 13829–13838, Nov. 2019, doi: 10.1039/c9tc04561a.
- [89] I. G. Gonzalez-Martinez *et al.*, "Electron-beam induced synthesis of nanostructures: A review," *Nanoscale*, vol. 8, no. 22. Royal Society of Chemistry, pp. 11340–11362, Jun. 14, 2016, doi: 10.1039/c6nr01941b.
- [90] R. Sarkar, C. Rentenberger, and J. Rajagopalan, "Electron beam induced artifacts during in situ TEM deformation of nanostructured metals," *Sci. Rep.*, vol. 5, no. 1, pp. 1–11, Nov. 2015, doi: 10.1038/srep16345.
- [91] A. L. Koh, E. Gidcumb, O. Zhou, and R. Sinclair, "Oxidation of Carbon Nanotubes in an Ionizing Environment," *Nano Lett.*, vol. 16, no. 2, pp. 856–863, Feb. 2016, doi: 10.1021/acs.nanolett.5b03035.
- [92] H. Yoshida, H. Omote, and S. Takeda, "Oxidation and reduction processes of platinum nanoparticles observed at the atomic scale by environmental transmission electron

- microscopy,” *Nanoscale*, vol. 6, no. 21, pp. 13113–13118, Nov. 2014, doi: 10.1039/c4nr04352a.
- [93] M. Sun, X. Li, Z. Tang, X. Wei, and Q. Chen, “Constant-rate dissolution of InAs nanowires in radiolytic water observed by: In situ liquid cell TEM,” *Nanoscale*, vol. 10, no. 42, pp. 19733–19741, Nov. 2018, doi: 10.1039/c8nr04096f.
- [94] N. M. Schneider, M. M. Norton, B. J. Mendel, J. M. Grogan, F. M. Ross, and H. H. Bau, “Electron-Water interactions and implications for liquid cell electron microscopy,” *J. Phys. Chem. C*, vol. 118, no. 38, pp. 22373–22382, Sep. 2014, doi: 10.1021/jp507400n.
- [95] D. B. Williams, C. B. Carter, D. B. Williams, and C. B. Carter, “Inelastic Scattering and Beam Damage,” in *Transmission Electron Microscopy*, Springer US, 2009, pp. 53–71.
- [96] H. Guo *et al.*, “Vanadium dioxide nanowire-based microthermometer for quantitative evaluation of electron beam heating,” *Nat. Commun.*, vol. 5, no. 1, pp. 1–5, Oct. 2014, doi: 10.1038/ncomms5986.
- [97] S. Y. Lee, W. Y. Lee, J. T. L. Thong, G. S. Kim, and S. K. Lee, “Lateral heat flow distribution and defect-dependent thermal resistance in an individual silicon nanowire,” *Nanotechnology*, vol. 27, no. 11, p. 115402, Feb. 2016, doi: 10.1088/0957-4484/27/11/115402.
- [98] D. R. Queen and F. Hellman, “Thin film nanocalorimeter for heat capacity measurements of 30 nm films,” *Rev. Sci. Instrum.*, vol. 80, no. 6, p. 063901, Jun. 2009, doi: 10.1063/1.3142463.
- [99] A. J. Schmidt, R. Cheaito, and M. Chiesa, “A frequency-domain thermoreflectance method for the characterization of thermal properties,” *Rev. Sci. Instrum.*, vol. 80, no. 9, p. 094901, Sep. 2009, doi: 10.1063/1.3212673.
- [100] H. Malekpour and A. A. Balandin, “Raman-based technique for measuring thermal conductivity of graphene and related materials,” *J. Raman Spectrosc.*, vol. 49, no. 1, pp. 106–120, Jan. 2018, doi: 10.1002/jrs.5230.
- [101] E. Pop, “Energy dissipation and transport in nanoscale devices,” *Nano Research*, vol. 3, no. 3. Tsinghua University Press, pp. 147–169, Mar. 18, 2010, doi: 10.1007/s12274-010-1019-z.
- [102] J. A. Hachtel, A. R. Lupini, and J. C. Idrobo, “Exploring the capabilities of monochromated electron energy loss spectroscopy in the infrared regime,” *Sci. Rep.*, vol. 8, no. 1, pp. 1–

- 10, Dec. 2018, doi: 10.1038/s41598-018-23805-5.
- [103] “Electron Energy Loss Spectroscopy - an overview | ScienceDirect Topics.” <https://www.sciencedirect.com/topics/chemistry/electron-energy-loss-spectroscopy> (accessed Apr. 14, 2021).
- [104] Yougui Liao “Heat generation/temperature increase by electron irradiation.” <https://www.globalsino.com/EM/page4685.html> (accessed Apr. 19, 2021).
- [105] H. Zhang, “The Instrument Review: Lecture one.” Accessed: Apr. 14, 2021. [Online]. Available: <http://www.tcd.ie/Physics/People/HongZhou.Zhang/Teaching/PY5019/2011.php>.
- [106] C. W. Oatley, W. C. Nixon, and R. F. W. Pease, “Scanning Electron Microscopy,” *Adv. Electron. Electron Phys.*, vol. 21, no. C, pp. 181–247, Jan. 1966, doi: 10.1016/S0065-2539(08)61010-0.
- [107] Y. Chen, R. E. Palmer, and J. P. Wilcoxon, “Sintering of passivated gold nanoparticles under the electron beam,” *Langmuir*, vol. 22, no. 6, pp. 2851–2855, Mar. 2006, doi: 10.1021/la0533157.
- [108] R. F. Egerton, P. Li, and M. Malac, “Radiation damage in the TEM and SEM,” in *Micron*, Aug. 2004, vol. 35, no. 6, pp. 399–409, doi: 10.1016/j.micron.2004.02.003.
- [109] Z. J. W. A. Leijten, A. D. A. Keizer, G. De With, and H. Friedrich, “Quantitative Analysis of Electron Beam Damage in Organic Thin Films,” *J. Phys. Chem. C*, vol. 121, no. 19, pp. 10552–10561, May 2017, doi: 10.1021/acs.jpcc.7b01749.
- [110] S. T. Skowron, T. W. Chamberlain, J. Biskupek, U. Kaiser, E. Besley, and A. N. Khlobystov, “Chemical Reactions of Molecules Promoted and Simultaneously Imaged by the Electron Beam in Transmission Electron Microscopy,” *Acc. Chem. Res.*, vol. 50, no. 8, pp. 1797–1807, Aug. 2017, doi: 10.1021/acs.accounts.7b00078.
- [111] X. Zhang *et al.*, “Unexpected refacetting of palladium nanoparticles under atmospheric N₂ conditions,” *Chem. Commun.*, vol. 54, no. 62, pp. 8587–8590, Jul. 2018, doi: 10.1039/c8cc04574g.
- [112] C. W. Huang, S. S. Kuo, and C. L. Hsin, “Electron-beam-induced phase transition in the transmission electron microscope: The case of VO₂(B),” *CrystEngComm*, vol. 20, no. 43, pp. 6857–6860, Nov. 2018, doi: 10.1039/c8ce01536h.
- [113] R. Anufriev, R. Yanagisawa, and M. Nomura, “Aluminium nanopillars reduce thermal

- conductivity of silicon nanobeams,” *Nanoscale*, vol. 9, no. 39, pp. 15083–15088, Oct. 2017, doi: 10.1039/c7nr05114j.
- [114] A. Lipatov *et al.*, “Low-temperature thermal reduction of graphene oxide: In situ correlative structural, thermal desorption, and electrical transport measurements,” *Appl. Phys. Lett.*, vol. 112, no. 5, p. 053103, Jan. 2018, doi: 10.1063/1.4996337.
- [115] E. J. VandenBussche and D. J. Flannigan, “Sources of error in Debye–Waller-effect measurements relevant to studies of photoinduced structural dynamics,” *Ultramicroscopy*, vol. 196, pp. 111–120, Jan. 2019, doi: 10.1016/j.ultramic.2018.10.002.
- [116] P. Hervés, M. Pérez-Lorenzo, L. M. Liz-Marzán, J. Dzubiella, Y. Lu, and M. Ballauff, “Catalysis by metallic nanoparticles in aqueous solution: Model reactions,” *Chemical Society Reviews*, vol. 41, no. 17. The Royal Society of Chemistry, pp. 5577–5587, Sep. 07, 2012, doi: 10.1039/c2cs35029g.
- [117] D. Yohan and B. D. Chithrani, “Applications of nanoparticles in nanomedicine,” *Journal of Biomedical Nanotechnology*, vol. 10, no. 9. American Scientific Publishers, pp. 2371–2392, 2014, doi: 10.1166/jbn.2014.2015.
- [118] H. Yu, Y. Peng, Y. Yang, and Z. Y. Li, “Plasmon-enhanced light–matter interactions and applications,” *npj Computational Materials*, vol. 5, no. 1. Nature Publishing Group, pp. 1–14, Dec. 01, 2019, doi: 10.1038/s41524-019-0184-1.
- [119] J. A. Adekoya, K. O. Ogunniran, T. O. Siyanbola, E. O. Dare, and N. Revaprasadu, “Band Structure, Morphology, Functionality, and Size- Dependent Properties of Metal Nanoparticles,” in *Noble and Precious Metals - Properties, Nanoscale Effects and Applications*, InTech, 2018.
- [120] S. E. Skrabalak, L. Au, X. Li, and Y. Xia, “Facile synthesis of Ag nanocubes and Au nanocages,” *Nat. Protoc.*, vol. 2, no. 9, pp. 2182–2190, Sep. 2007, doi: 10.1038/nprot.2007.326.
- [121] X. Lu, H. Y. Tuan, J. Chen, Z. Y. Li, B. A. Korgel, and Y. Xia, “Mechanistic studies on the galvanic replacement reaction between multiply twinned particles of Ag and H₂AuCl₄ in an organic medium,” *J. Am. Chem. Soc.*, vol. 129, no. 6, pp. 1733–1742, Feb. 2007, doi: 10.1021/ja067800f.
- [122] X. Lu, J. Chen, S. E. Skrabalak, and Y. Xia, “Galvanic replacement reaction: A simple and powerful route to hollow and porous metal nanostructures,” *Proc. Inst. Mech. Eng. Part N*

- J. Nanoeng. Nanosyst.*, vol. 221, no. 1, pp. 1–16, Mar. 2007, doi: 10.1243/17403499JNN111.
- [123] J. Chen *et al.*, “Gold Nanocages: Engineering Their Structure for Biomedical Applications**,” doi: 10.1002/adma.200500833.
- [124] Y. Sun, B. Mayers, and Y. Xia, “Metal Nanostructures with Hollow Interiors,” *Adv. Mater.*, vol. 15, no. 78, pp. 641–646, Apr. 2003, doi: 10.1002/adma.200301639.
- [125] A. Genç *et al.*, “Tuning the Plasmonic Response up: Hollow Cuboid Metal Nanostructures,” *ACS Photonics*, vol. 3, no. 5, pp. 770–779, May 2016, doi: 10.1021/acsp Photonics.5b00667.
- [126] S. Joseph and B. Mathew, “Facile synthesis of silver nanoparticles and their application in dye degradation,” *Mater. Sci. Eng. B Solid-State Mater. Adv. Technol.*, vol. 195, pp. 90–97, May 2015, doi: 10.1016/j.mseb.2015.02.007.
- [127] A. Feng, J. Cao, J. Wei, F. Chang, Y. Yang, and Z. Xiao, “Facile synthesis of silver nanoparticles with high antibacterial activity,” *Materials (Basel)*, vol. 11, no. 12, Dec. 2018, doi: 10.3390/ma11122498.
- [128] B. Khodashenas and H. R. Ghorbani, “Synthesis of silver nanoparticles with different shapes,” *Arabian Journal of Chemistry*, vol. 12, no. 8. Elsevier B.V., pp. 1823–1838, Dec. 01, 2019, doi: 10.1016/j.arabjc.2014.12.014.
- [129] M. Sumithra, Y. Aparna, P. Raghavendra Rao, K. Srinivasa Reddy, and P. Ranjith Reddy, “Morphological change of silver nanoparticles by the effect of synthesis parameters,” in *Materials Today: Proceedings*, Jan. 2016, vol. 3, no. 6, pp. 2278–2283, doi: 10.1016/j.matpr.2016.04.137.
- [130] A. Pyatenko, M. Yamaguchi, and M. Suzuki, “Synthesis of spherical silver nanoparticles with controllable sizes in aqueous solutions,” *J. Phys. Chem. C*, vol. 111, no. 22, pp. 7910–7917, Jun. 2007, doi: 10.1021/jp071080x.
- [131] H. Xu *et al.*, “Synthesis of high-purity silver nanorods with tunable plasmonic properties and sensor behavior,” *Photonics Res.*, vol. 5, no. 1, p. 27, Feb. 2017, doi: 10.1364/prj.5.000027.
- [132] M. Torras and A. Roig, “From Silver Plates to Spherical Nanoparticles: Snapshots of Microwave-Assisted Polyol Synthesis,” *ACS Omega*, Mar. 2020, doi: 10.1021/acsomega.9b03748.
- [133] B. Wiley, T. Herricks, Y. Sun, and Y. Xia, “Polyol synthesis of silver nanoparticles: Use of

- chloride and oxygen to promote the formation of single-crystal, truncated cubes and tetrahedrons,” *Nano Lett.*, vol. 4, no. 9, pp. 1733–1739, Sep. 2004, doi: 10.1021/nl048912c.
- [134] T. Nagy-Simon *et al.*, “Antibody Conjugated, Raman Tagged Hollow Gold-Silver Nanospheres for Specific Targeting and Multimodal Dark-Field/SERS/Two Photon-FLIM Imaging of CD19(+) B Lymphoblasts,” *ACS Appl. Mater. Interfaces*, vol. 9, no. 25, pp. 21155–21168, Jun. 2017, doi: 10.1021/acsami.7b05145.
- [135] Y. Xie *et al.*, “Controlled growth and optical response of a semi-hollow plasmonic nanocavity and ultrathin sulfide nanosheets on Au/Ag platelets,” *Nanoscale*, vol. 10, no. 3, pp. 1279–1285, Jan. 2018, doi: 10.1039/c7nr07362c.
- [136] T. Tan *et al.*, “LSPR-dependent SERS performance of silver nanoplates with highly stable and broad tunable LSPRs prepared through an improved seed-mediated strategy,” *Phys. Chem. Chem. Phys.*, vol. 15, no. 48, pp. 21034–21042, Dec. 2013, doi: 10.1039/c3cp52236a.
- [137] F. Y. Kong, J. W. Zhang, R. F. Li, Z. X. Wang, W. J. Wang, and W. Wang, “Unique roles of gold nanoparticles in drug delivery, targeting and imaging applications,” *Molecules*, vol. 22, no. 9. MDPI AG, Sep. 01, 2017, doi: 10.3390/molecules22091445.
- [138] C. Zhang, T. Brinzer, C. Liu, S. Garrett-Roe, and N. L. Rosi, “Loading and triggered release of cargo from hollow spherical gold nanoparticle superstructures,” *RSC Adv.*, vol. 5, no. 93, pp. 76291–76295, Aug. 2015, doi: 10.1039/c5ra15492h.
- [139] S. V. Jenkins, T. D. Gohman, E. K. Miller, and J. Chen, “Synthesis of Hollow Gold-Silver Alloyed Nanoparticles: A ‘Galvanic Replacement’ Experiment for Chemistry and Engineering Students,” *J. Chem. Educ.*, vol. 92, no. 6, pp. 1056–1060, Jun. 2015, doi: 10.1021/acs.jchemed.5b00042.
- [140] J. R. Daniel, L. A. McCarthy, E. Ringe, and D. Boudreau, “Enhanced control of plasmonic properties of silver-gold hollow nanoparticles via a reduction-assisted galvanic replacement approach,” *RSC Adv.*, vol. 9, no. 1, pp. 389–396, Dec. 2019, doi: 10.1039/C8RA09364D.
- [141] Y. Sun and Y. Xia, “Triangular Nanoplates of Silver: Synthesis, Characterization, and Use as Sacrificial Templates For Generating Triangular Nanorings of Gold,” *Adv. Mater.*, vol. 15, no. 9, pp. 695–699, May 2003, doi: 10.1002/adma.200304652.
- [142] M. A. Mahmoud and M. A. El-Sayed, “Gold Nanoframes: Very High Surface Plasmon Fields and Excellent Near-Infrared Sensors,” *J. Am. Chem. Soc.*, vol. 132, no. 36, pp. 12704–

- 12710, Sep. 2010, doi: 10.1021/ja104532z.
- [143] X. Lu, J. Chen, S. E. Skrabalak, and Y. Xia, "Galvanic replacement reaction: A simple and powerful route to hollow and porous metal nanostructures," *Proc. Inst. Mech. Eng. Part N J. Nanoeng. Nanosyst.*, vol. 221, no. 1, pp. 1–16, Mar. 2007, doi: 10.1243/17403499JNN111.
- [144] S. E. Skrabalak, J. Chen, L. Au, X. Lu, X. Li, and Y. Xia, "Gold Nanocages for Biomedical Applications," *Adv. Mater.*, vol. 19, no. 20, pp. 3177–3184, Oct. 2007, doi: 10.1002/adma.200701972.
- [145] W. Shin, K. Kang, and H. Jang, "Recent Advances in Nanoparticle Shape and Composition Regulation Based on Galvanic Replacement for Cancer Treatment," no. July, Jul. 2018, doi: 10.20944/preprints201807.0226.v1.
- [146] M. S. Yavuz *et al.*, "Gold nanocages covered by smart polymers for controlled release with near-infrared light," *Nat. Mater.*, vol. 8, no. 12, pp. 935–939, Dec. 2009, doi: 10.1038/nmat2564.
- [147] P. Shi, K. Qu, J. Wang, M. Li, J. Ren, and X. Qu, "PH-responsive NIR enhanced drug release from gold nanocages possesses high potency against cancer cells," *Chem. Commun.*, vol. 48, no. 61, pp. 7640–7642, Aug. 2012, doi: 10.1039/c2cc33543c.
- [148] P. Sahandi Zangabad *et al.*, "Nanocaged platforms: Modification, drug delivery and nanotoxicity. Opening synthetic cages to release the tiger," *Nanoscale*, vol. 9, no. 4. Royal Society of Chemistry, pp. 1356–1392, Jan. 28, 2017, doi: 10.1039/c6nr07315h.
- [149] G. D. Moon *et al.*, "A new theranostic system based on gold nanocages and phase-change materials with unique features for photoacoustic imaging and controlled release," *J. Am. Chem. Soc.*, vol. 133, no. 13, pp. 4762–4765, Apr. 2011, doi: 10.1021/ja200894u.
- [150] L. Tian, N. Gandra, and S. Singamaneni, "Monitoring controlled release of payload from gold nanocages using surface enhanced raman scattering," *ACS Nano*, vol. 7, no. 5, pp. 4252–4260, May 2013, doi: 10.1021/nn400728t.
- [151] Z. Zhang *et al.*, "Photothermal gold nanocages filled with temperature sensitive tetradecanol and encapsulated with glutathione responsive polycurcumin for controlled DOX delivery to maximize anti-MDR tumor effects," *J. Mater. Chem. B*, vol. 5, no. 27, pp. 5464–5472, Jul. 2017, doi: 10.1039/c7tb01253e.
- [152] W. Xiong, R. Mazid, L. W. Yap, X. Li, and W. Cheng, "Plasmonic caged gold nanorods for

- near-infrared light controlled drug delivery,” *Nanoscale*, vol. 6, no. 23, pp. 14388–14393, Dec. 2014, doi: 10.1039/c4nr04400b.
- [153] H. Cheng *et al.*, “Combination cancer treatment through photothermally controlled release of selenous acid from gold nanocages,” *Biomaterials*, vol. 178, pp. 517–526, Sep. 2018, doi: 10.1016/j.biomaterials.2018.03.058.
- [154] Y. Yu *et al.*, “A new NIR-triggered doxorubicin and photosensitizer indocyanine green co-delivery system for enhanced multidrug resistant cancer treatment through simultaneous chemo/photothermal/photodynamic therapy,” *Acta Biomater.*, vol. 59, pp. 170–180, Sep. 2017, doi: 10.1016/j.actbio.2017.06.026.
- [155] S. Vanden-Hehir, W. J. Tipping, M. Lee, V. G. Brunton, A. Williams, and A. N. Hulme, “Raman imaging of nanocarriers for drug delivery,” *Nanomaterials*, vol. 9, no. 3. MDPI AG, Mar. 01, 2019, doi: 10.3390/nano9030341.
- [156] G. P. S. Smith, C. M. McGoverin, S. J. Fraser, and K. C. Gordon, “Raman imaging of drug delivery systems,” *Advanced Drug Delivery Reviews*, vol. 89. Elsevier, pp. 21–41, Jul. 15, 2015, doi: 10.1016/j.addr.2015.01.005.
- [157] G. Niu and X. Chen, “The Role of Molecular Imaging in Drug Delivery.,” *Drug Deliv. (London, England. 2007)*, vol. 3, pp. 109–113, 2009, Accessed: Oct. 04, 2020. [Online]. Available: <http://www.ncbi.nlm.nih.gov/pubmed/26435748>.
- [158] M. Hamoudeh, M. A. Kamleh, R. Diab, and H. Fessi, “Radionuclides delivery systems for nuclear imaging and radiotherapy of cancer,” *Advanced Drug Delivery Reviews*, vol. 60, no. 12. Adv Drug Deliv Rev, pp. 1329–1346, Sep. 15, 2008, doi: 10.1016/j.addr.2008.04.013.
- [159] T. Etrych, H. Lucas, O. Janoušková, P. Chytil, T. Mueller, and K. Mäder, “Fluorescence optical imaging in anticancer drug delivery,” *Journal of Controlled Release*, vol. 226. Elsevier B.V., pp. 168–181, Mar. 28, 2016, doi: 10.1016/j.jconrel.2016.02.022.
- [160] A. L. Shluger, A. L. Rohl, D. H. Gay, and R. T. Williams, “Atomistic theory of the interaction between AFM tips and ionic surfaces,” *J. Phys. Condens. Matter*, vol. 6, no. 10, pp. 1825–1846, Mar. 1994, doi: 10.1088/0953-8984/6/10/003.
- [161] D. A. Lamprou, V. Venkatpurwar, and M. N. V. R. Kumar, “Atomic Force Microscopy Images Label-Free, Drug Encapsulated Nanoparticles In Vivo and Detects Difference in Tissue Mechanical Properties of Treated and Untreated: A Tip for Nanotoxicology,” *PLoS*

- One*, vol. 8, no. 5, p. e64490, May 2013, doi: 10.1371/journal.pone.0064490.
- [162] Y. Gu *et al.*, “AFM characterization of dendrimer-stabilized platinum nanoparticles,” *Langmuir*, vol. 21, no. 7, pp. 3122–3131, Mar. 2005, doi: 10.1021/la047843e.
- [163] D. Ahmed, M. Raza, S. Ahmed, M. R. Shah, and S. Perveen, “Cephadrine Coated Silver Nanoparticle their Drug Release Mechanism, and Antimicrobial Potential against Gram-Positive and Gram-Negative Bacterial Strains through AFM Chemosensing View project Design, Synthesis and characterization of macromolecules in Supramolecular Chemistry View project Cephadrine Coated Silver Nanoparticle their Drug Release Mechanism, and Antimicrobial Potential against Gram-Positive and Gram-Negative Bacterial Strains through AFM,” 2018. Accessed: Oct. 04, 2020. [Online]. Available: <https://www.researchgate.net/publication/325194963>.
- [164] S. M. Rajput *et al.*, “Nano-Vehicles for Drug Delivery Using Low-Cost Cationic Surfactants: A Drug Induced Structural Transitions,” *ChemistrySelect*, vol. 3, no. 32, pp. 9454–9463, Aug. 2018, doi: 10.1002/slct.201801111.
- [165] Z. Li, A. L. B. de Barros, D. C. F. Soares, S. N. Moss, and L. Alisaraie, “Functionalized single-walled carbon nanotubes: cellular uptake, biodistribution and applications in drug delivery,” *International Journal of Pharmaceutics*, vol. 524, no. 1–2. Elsevier B.V., pp. 41–54, May 30, 2017, doi: 10.1016/j.ijpharm.2017.03.017.
- [166] Q. Guo, X. tao Shen, Y. yuan Li, and S. qing Xu, “Carbon nanotubes-based drug delivery to cancer and brain,” *J. Huazhong Univ. Sci. Technol. - Med. Sci.*, vol. 37, no. 5, pp. 635–641, Oct. 2017, doi: 10.1007/s11596-017-1783-z.
- [167] A. Baeza, R. R. Castillo, A. Torres-Pardo, J. M. González-Calbet, and M. Vallet-Regí, “Electron microscopy for inorganic-type drug delivery nanocarriers for antitumoral applications: what does it reveal?,” *Journal of Materials Chemistry B*, vol. 5, no. 15. Royal Society of Chemistry, pp. 2714–2725, Apr. 12, 2017, doi: 10.1039/c6tb03062a.
- [168] J. Kuntsche, J. C. Horst, and H. Bunjes, “Cryogenic transmission electron microscopy (cryo-TEM) for studying the morphology of colloidal drug delivery systems,” *International Journal of Pharmaceutics*, vol. 417, no. 1–2. Elsevier B.V., pp. 120–137, Sep. 30, 2011, doi: 10.1016/j.ijpharm.2011.02.001.
- [169] S. R. Falsafi, H. Rostamabadi, E. Assadpour, and S. M. Jafari, “Morphology and microstructural analysis of bioactive-loaded micro/nanocarriers via microscopy techniques;

- CLSM/SEM/TEM/AFM,” *Advances in Colloid and Interface Science*, vol. 280. Elsevier B.V., p. 102166, Jun. 01, 2020, doi: 10.1016/j.cis.2020.102166.
- [170] R. Nikkhah-Moshaie, A. Kaushik, R. D. Jayant, V. Bhardwaj, and M. Nair, “TEM Investigation of Nanocarriers Distribution in Mice Brain,” *Microsc. Microanal.*, vol. 22, no. S3, pp. 1172–1173, Jul. 2016, doi: 10.1017/s143192761600670x.
- [171] A. GOLDSTEIN, Y. SOROKA, M. FRUŠIĆ-ZLOTKIN, I. POPOV, and R. KOHEN, “High resolution SEM imaging of gold nanoparticles in cells and tissues,” *J. Microsc.*, vol. 256, no. 3, pp. 237–247, Dec. 2014, doi: 10.1111/jmi.12179.
- [172] G. Plascencia-Villa, C. R. Starr, L. S. Armstrong, A. Ponce, and M. José-Yacamán, “Imaging interactions of metal oxide nanoparticles with macrophage cells by ultra-high resolution scanning electron microscopy techniques,” *Integr. Biol.*, vol. 4, no. 11, p. 1358, Oct. 2012, doi: 10.1039/c2ib20172k.
- [173] A. M. Schrand, J. J. Schlager, L. Dai, and S. M. Hussain, “Preparation of cells for assessing ultrastructural localization of nanoparticles with transmission electron microscopy,” *Nat. Protoc.*, vol. 5, no. 4, pp. 744–757, Mar. 2010, doi: 10.1038/nprot.2010.2.
- [174] W. Albrecht *et al.*, “Impact of the electron beam on the thermal stability of gold nanorods studied by environmental transmission electron microscopy,” *Ultramicroscopy*, vol. 193, pp. 97–103, Oct. 2018, doi: 10.1016/j.ultramic.2018.05.006.
- [175] J. Goworek, A. Kierys, W. Gac, A. Borówka, and R. Kusak, “Thermal degradation of CTAB in as-synthesized MCM-41,” *J. Therm. Anal. Calorim.*, vol. 96, no. 2, pp. 375–382, May 2009, doi: 10.1007/s10973-008-9055-6.
- [176] D. Rioux, S. Vallières, S. Besner, P. Muñoz, E. Mazur, and M. Meunier, “An Analytic Model for the Dielectric Function of Au, Ag, and their Alloys,” *Adv. Opt. Mater.*, vol. 2, no. 2, pp. 176–182, Feb. 2014, doi: 10.1002/adom.201300457.
- [177] D. Wan, X. Xia, Y. Wang, and Y. Xia, “Robust Synthesis of Gold Cubic Nanoframes through a Combination of Galvanic Replacement, Gold Deposition, and Silver Dealloying,” *Small*, vol. 9, no. 18, pp. 3111–3117, Sep. 2013, doi: 10.1002/smll.201203233.
- [178] E. González, J. Arbiol, and V. F. Puntes, “Carving at the Nanoscale: Sequential Galvanic Exchange and Kirkendall Growth at Room Temperature,” *Science (80-.)*, vol. 334, no. 6061, pp. 1377 LP – 1380, Dec. 2011, doi: 10.1126/science.1212822.
- [179] H. J. Fan, U. Gösele, and M. Zacharias, “Formation of Nanotubes and Hollow

- Nanoparticles Based on Kirkendall and Diffusion Processes: A Review,” *Small*, vol. 3, no. 10, pp. 1660–1671, Oct. 2007, doi: 10.1002/smll.200700382.
- [180] “Kirkendall Effect and Inverse Kirkendall Effect,” in *Kinetics in Nanoscale Materials*, Hoboken, NJ, USA: John Wiley & Sons, Inc., 2014, pp. 67–98.
- [181] A. Ait-Oubba, C. Coupeau, J. Durinck, M. Talea, and J. Grilhé, “Effect of surface on the dissociation of perfect dislocations into Shockley partials describing the herringbone Au(1 1 1) surface reconstruction,” *Philos. Mag.*, vol. 98, no. 17, pp. 1594–1607, Jun. 2018, doi: 10.1080/14786435.2018.1447702.
- [182] D. Roy, “Consolidation of Mechanically Alloyed Products/Powders,” in *Handbook of Mechanical Nanostructuring*, Weinheim, Germany: Wiley-VCH Verlag GmbH & Co. KGaA, 2015, pp. 681–700.
- [183] S. Liu *et al.*, “Partial-surface-passivation strategy for transition-metal-based copper–gold nanocage,” *Chem. Commun.*, vol. 52, no. 39, pp. 6617–6620, May 2016, doi: 10.1039/C6CC01779G.
- [184] S. Raveendran, H.-T. Lim, T. Maekawa, M. V. Matham, and D. S. Kumar, “Gold nanocages entering into the realm of high-contrast photoacoustic ocular imaging,” *Nanoscale*, vol. 10, no. 29, pp. 13959–13968, Jul. 2018, doi: 10.1039/C8NR02866D.
- [185] H. Qian *et al.*, “Efficient light generation from enhanced inelastic electron tunnelling,” *Nat. Photonics*, vol. 12, no. 8, pp. 485–488, Aug. 2018, doi: 10.1038/s41566-018-0216-2.
- [186] L. Hung, S. Y. Lee, O. McGovern, O. Rabin, and I. Mayergoyz, “Calculation and measurement of radiation corrections for plasmon resonances in nanoparticles,” *Phys. Rev. B*, vol. 88, no. 7, p. 075424, Aug. 2013, doi: 10.1103/PhysRevB.88.075424.
- [187] N. Halas, “Playing with plasmons: Tuning the optical resonant properties of metallic nanoshells,” *MRS Bull.*, vol. 30, no. 5, pp. 362–367, 2005, doi: 10.1557/mrs2005.99.
- [188] E. Prodan, C. Radloff, N. J. Halas, and P. Nordlander, “A Hybridization Model for the Plasmon Response of Complex Nanostructures,” *Science (80-.)*, vol. 302, no. 5644, pp. 419 LP – 422, Oct. 2003, doi: 10.1126/science.1089171.
- [189] H. Wang *et al.*, “Symmetry breaking in individual plasmonic nanoparticles.,” *Proc. Natl. Acad. Sci. U. S. A.*, vol. 103, no. 29, pp. 10856–60, Jul. 2006, doi: 10.1073/pnas.0604003103.
- [190] M. Guettari, R. Gomati, and A. Gharbi, “Effect of temperature on cononsolvency of

- polyvinylpyrrolidone in water/methanol mixture,” *J. Macromol. Sci. Part B Phys.*, vol. 49, no. 3, pp. 552–562, 2010, doi: 10.1080/00222341003595378.
- [191] M. Guettari, A. Belaidi, S. Abel, and T. Tajouri, “Polyvinylpyrrolidone Behavior in Water/Ethanol Mixed Solvents: Comparison of Modeling Predictions with Experimental Results,” *J. Solution Chem.*, vol. 46, no. 7, pp. 1404–1417, Jul. 2017, doi: 10.1007/s10953-017-0649-0.
- [192] F. Niekieł, S. M. Kraschewski, J. Müller, B. Butz, and E. Spiecker, “Local temperature measurement in TEM by parallel beam electron diffraction,” *Ultramicroscopy*, vol. 176, pp. 161–169, May 2017, doi: 10.1016/j.ultramic.2016.11.028.
- [193] Z. Wang, L. Gui, D. Han, Z. Xu, L. Han, and S. Xu, “Measurement and Evaluation of Local Surface Temperature Induced by Irradiation of Nanoscaled or Microscaled Electron Beams,” *Nanoscale Res. Lett.*, vol. 14, no. 1, pp. 1–11, Jan. 2019, doi: 10.1186/s11671-018-2821-x.
- [194] T. Yamane, N. Nagai, S. I. Katayama, and M. Todoki, “Measurement of thermal conductivity of silicon dioxide thin films using a 3w method,” *J. Appl. Phys.*, vol. 91, no. 12, pp. 9772–9776, Jun. 2002, doi: 10.1063/1.1481958.
- [195] “Thermal Conductivity of Metals, Metallic Elements and Alloys.” https://www.engineeringtoolbox.com/thermal-conductivity-metals-d_858.html (accessed Apr. 15, 2021).
- [196] B. Mu and M. Li, “Fabrication and thermal properties of tetradecanol/graphene aerogel form-stable composite phase change materials,” *Sci. Rep.*, vol. 8, no. 1, p. 8878, Dec. 2018, doi: 10.1038/s41598-018-27038-4.
- [197] “NIST Standard Reference Database 71 | NIST.” <https://www.nist.gov/srd/nist-standard-reference-database-71> (accessed Apr. 15, 2021).
- [198] Y. Dubi and Y. Sivan, “‘Hot’ electrons in metallic nanostructures—non-thermal carriers or heating?,” *Light Sci. Appl.*, vol. 8, no. 1, pp. 2047–7538, Dec. 2019, doi: 10.1038/s41377-019-0199-x.

7 APPENDIX

7.1 Appendix I

I performed extensive SEM and HAADF-STEM characterization for all the 12 samples I synthesized. Figure A-I and Figure A-II show the SEM and ADF-STEM images of hollow-MNPs for every step of the galvanic replacement process. In these images, the evolution of the voids and pinholes is evident.

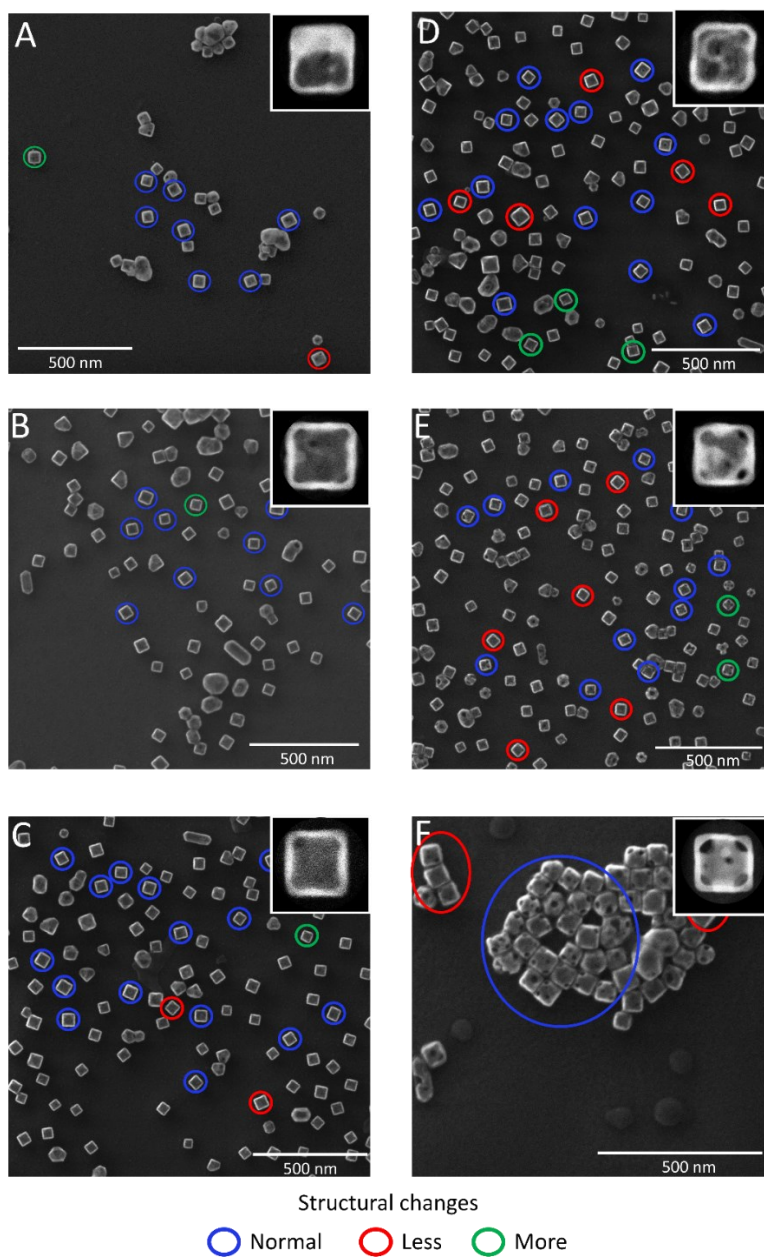


Figure A-I SEM images of hollow-MNPs for the small template. HAuCl₄ concentration increases from A to F. The inset shows the ADF-STEM image for a single nanoparticle showing the characteristic structural features of the ensemble.

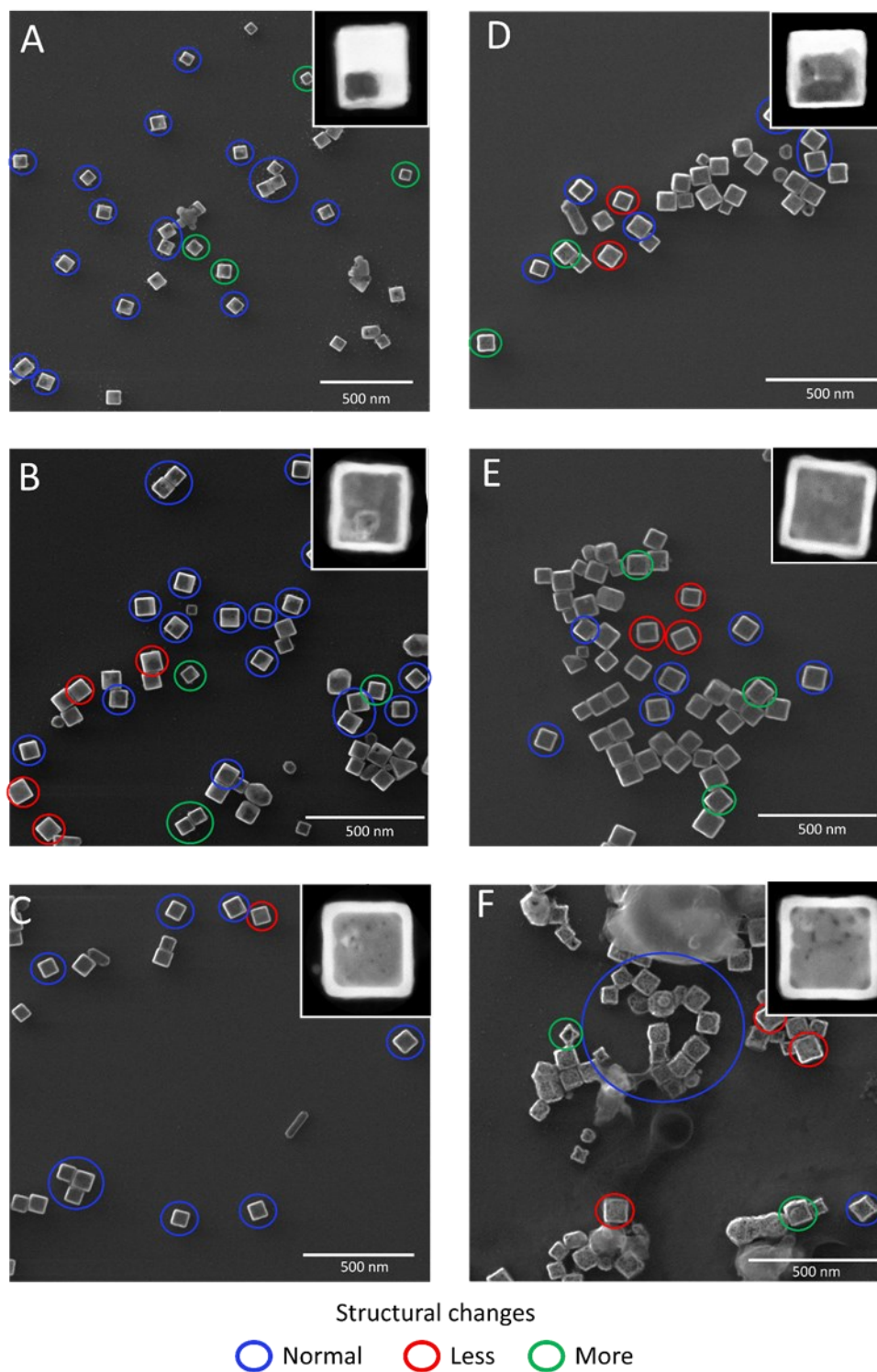


Figure A-II SEM images of hollow-MNPs for the small template. HAuCl_4 concentration increases from A to F. The inset shows the ADF-STEM image for a single nanoparticle showing the characteristic structural features of the ensemble.

